Chem Soc Rev

Recent Advances in Flexible Solid-State Supercapacitors: Substrates, Electrolytes, and Cell Designs

Journal:	*Chemical Society Reviews*
Manuscript ID	CS-SYN-07-2017-000505.R1
Article Type:	Synopsis
Date Submitted by the Author:	n/a

Complete List of Authors:	Dubal, deepak; Gwangju Institute of Science and Technology, School of Materials Science and Engineering; Catalan Institute of Nanoscience and Nanotechnology, CIN2, ICN2 (CSIC-ICN), Bellaterra (Barcelona), Spain, NEO Energy-Oriented Materials Group Chodankar, Nilesh; Chonnam National University, Department of Chemical Engineering Kim, Do-Heyoung; Chonnam National University, School of Chemical Engineering Gomez-Romero, Pedro; Nanoscience and Nanotechnology Research Center (CSIC-ICN),

Recent Advances in Flexible Solid-State Supercapacitors: Substrates, Electrolytes, and Cell Designs

*Deepak P. Dubal,[a, b]** Nilesh R. Chodankar,[c] Do-Heyoung Kim,[c]* Pedro Gomez-Romero,[b]**

[a] *School of Chemical Engineering, The University of Adelaide, Adelaide, South Australia 5005, Australia*

[b] Catalan Institute of Nanoscience and Nanotechnology (ICN2), CSIC and The Barcelona Institute of Science and Technology, Campus UAB, Bellaterra, 08193 Barcelona, Spain

[c] *School of Chemical Engineering, Chonnam National University, Gwangju 500-757, South Korea*

CORRESPONDING AUTHOR FOOTNOTE

Dr. Deepak Dubal and Prof. Pedro Gomez-Romero

Tel.: +6183131535 Fax: +61883134373

E-mail: dubaldeepak2@gmail.com (D. Dubal),

pedro.gomez@cin2.es (P. Gomez-Romero)

Abstract

Flexible solid-state supercapacitors (FSSCs) are frontrunners in energy storage device technology and have attracted much attention due to recent significant breakthroughs in modern wearable electronics. Herein, we review the state-of-the-art advancements in FSSCs to provide new insights on mechanisms, emerging electrode materials, flexible gel electrolytes, and novel cell designs. The review begins with a short introduction on the fundamental understanding of charge storage mechanisms based on the structural properties of electrode materials. The next sections briefly summarize the latest progress in flexible electrodes (free standing and substrate-supported, including textile, paper, metal foil/wire, and polymer-based substrates) and flexible gel electrolytes (aqueous, organic, ionic liquids, and redox-active gels). Subsequently, a comprehensive summary of FSSC cell designs introduces some emerging electrode materials, including MXenes, metal nitrides, metal-organic frameworks, polyoxometalates, and black phosphorus. Some potential practical applications, such as piezoelectric, photo-, and shape-memory supercapacitors are also discussed. The final section highlights current challenges and future perspectives on further research in this thriving field.

1. Introduction

Over the past decade, with the continuous emergence of applications in various sectors (mobility, biomedical, consumer electronics, sports, clean energy, and environmental), flexible and wearable microelectronic devices and systems have gained significant importance [1, 2]. Thus, the commercialization of flexible electronics is posing new challenges to well-established energy storage systems [3]. For instance, new energy storage devices need to maintain a high performance under continuous mechanical deformation, such as bending, folding, twisting, and stretching, for long cycles. Moreover, recent progress in implantable/wearable healthcare devices (spirometers, sphygmomanometers, wristbands, etc.) advocates a new self-sustainable energy storage device that can harvest/store body energy (breathing, arm pressing, chest compression, etc.) and power smart electronics [4, 5]. The key challenge is to design and assemble flexible electrode materials with high energy and power densities and excellent long-cycle stability with compatible electrolytes and separators in a flexible assembly. Safety and cost also need to be considered, especially for wearable and implantable devices. Thus, we believe that there will be a great demand for flexible energy storage systems for next generation implantable/wearable electronics.

Supercapacitors (SCs) are promising electrochemical energy storage devices that have attracted significant interest in both academia and industry during the past several decades because of their superior energy density (compared to conventional capacitors), good power density (compared to batteries), fast charge/discharge rates, and long cycle life [6, 7]. Currently, SCs are extensively used in many applications such as consumer electronics, transportation, military and aerospace, grid balancing, and power backup to protect, enhance, and/or replace batteries in these applications [8-10]. The history and origin of SCs has been extensively discussed in literature [9, 10]. In brief, the first SC patent was granted in 1957, when Becker from General Electric Corp. proposed a high-surface-area carbon-coated metallic current collector in H_2SO_4 solution. Sohio was the first to commercialize SCs in 1969 [7-10]. Between

1975 and 1981, Conway [10] proposed a new concept of energy storage in SCs using a RuO_2 film in aqueous H_2SO_4 electrolyte. The charge storage mechanism was referred to as a "pseudocapacitor," and was based on a non-faradaic process derived from surface redox reactions. In the 1990s, SCs became prominent when they began to be used, along with rechargeable batteries, to provide additional power in electrical vehicles (EVs) and hybrid electric vehicles (HEVs). These SCs captured and stored energy from regenerative braking and supplied vehicle acceleration power.

Traditional SCs exhibit clumsy bulk shapes (a separator sandwiched between two electrodes sealed in a liquid electrolyte) that present some major drawbacks for practical wearable application. For example, the liquid electrolyte requires high-standard safety encapsulation materials and technology to prevent leakage of toxic electrolytes. Moreover, because SC components can only be assembled in a few shapes/sizes, such as button and spiral wound cylinders, it is difficult to integrate them with other functional systems on the electronic motherboard. Thus, to transcend these limitations, flexible solid-state supercapacitors (FSSCs) have emerged as a new class of energy storage devices and have attracted considerable attention in recent years [11-12]. FSSC devices comprise flexible electrodes, a solid-state gel-electrolyte, a separator, and flexible packaging material similar to that of conventional SCs. The main advantage of FSSCs over conventional SCs is the use of a solid-state gel electrolyte and flexible electrodes that can be assembled in any shape/size with thin, light, and smart designs, thereby increasing their potential for application to flexible and wearable electronics.

Research on solid-state SCs began with the study of carbon and conducting polymer (CP)-based materials post 1990 [13]. The studies were continued in the beginning of the 20th century with some major contributions [14]. In these studies, the solid-state SCs were typically assembled by sandwiching a polymer gel electrolyte between two electrode pellets or films [active materials deposited on substrates e.g. stainless steel (SS)] and pressed together into

one device. This approach of first fabricating the electrodes and polymer electrolyte separately and subsequently assembling them together poses two major shortcomings: first, the reduction in thickness of the entire device is limited due to the use of thick solid-state gel electrolytes (the thinnest membrane prepared in a Petri dish was 0.15 mm) and metallic current collectors. Thus, the middle polymer gel electrolyte needs to be as thin as possible but thick enough to separate the two electrodes. Second, because the solid electrodes are in contact with the solid-state electrolyte under pressure, only the part of the electrode near the geometric electrode/electrolyte interface can be well utilized. However, the last few years have witnessed several innovative strategies to address previous challenges and new excellent breakthrough investigations have been reported [15-16]. The graphs shown in Figure 1 (a, b) depicts the number of articles published so far with corresponding number of citations (source: Scopus). The remarkable increasing trend in the number of articles published per year together with the outstanding number of citations suggests the prominence of next generation FSSC technology.

Currently, although many excellent reviews on FSSCs are available [1, 15-18], few give a complete picture that comprises the nature of the substrates, electrolytes, and cell design [16] and instead focus on these features, separately [18, 19]. In addition, the last few years have witnessed the emergence of many new materials for FSSC application, including two-dimensional (2D) materials and polyoxometalates (POMs), metal-organic frameworks (MOFs), which have yet to be summarized. Thus, a systematic summary of the latest innovations in FSSCs, which covers a fundamental understanding, new emerging materials, and novel cell designs is highly required. Accordingly, this review briefly describes the latest scientific progress in FSSCs and is divided into sections that discuss novel insights on charge storage mechanisms, flexible substrates, flexible electrolytes (gel electrolytes), and novel cell designs with new electrode materials together with their corresponding applications (Figure 2). Particularly, the first section highlights recently developed findings on ionic charge storage mechanisms and transport pathways. Next, we present a summary of recent progress in the

development of flexible substrates, including metallic foil/mesh/wire-, conventional and carbon paper-, carbon fabric-, yarn-, and polymer-based substrates. Section third focused on recent advancements in polymer gel electrolyte synthesis and the corresponding effect on electrochemical performances. Various gel electrolytes, such as aqueous, organic, ionic liquid, and redox-active gels, are briefly discussed. Section fourth is a review of the different cell designs including symmetric and asymmetric configurations. It also introduces novel materials such as MXenes, metal nitrides, POMs, black phosphorus (BP), and MOF-derived materials. A brief description on the various negative electrode materials used in all solid-state asymmetric SCs is also provided. The last section details state-of-the-art research in device innovation for next generation SCs including piezoelectric, photo-SCs, and shape-memory SCs. To facilitate further research and development, some future research trends and directions are also discussed. Overall, the goal of this review is to provide readers with a comprehensive summary of recent advancements in FSSCs in terms of new electrode materials, gel electrolytes, and novel cell designs.

2. Novel insights on Charge Storage Mechanisms

Several reviews provide brief descriptions about the charge storage mechanisms and basic electrochemistry of SCs [7, 20]. However, this is not the scope of this review and herein, we only discuss recently reported insights. According to previous studies, SCs are generally classified into two broad categories [20, 21], namely electrical double-layer capacitors (EDLCs) and pseudocapacitors. In EDLCs, the electrical charge is stored at the electrode/electrolyte interface. The separation of charges is a physical process without any faradaic reactions on the electrode surface. Thus, EDLC capacitance strongly depends on the surface properties, such as pore size distribution and specific surface area (SSA), of the electrodes [5, 20, 21]. It was recommended that the pore size in porous EDLCs should be approximately twice the ionic size of the electrolytes to allow full access into the pore walls. Moreover, the solvated ions do not

enter into the pores if the size exceeds the pore dimensions. However, other works have experimentally invalidated this assumption and reported record-breaking specific capacitance values by decreasing the pore width for pores smaller than double the size of the bare ions [22, 23]. Ultimately, there is no clear correlation between the SSA and the specific capacitance, implying that the capacitance cannot be increased by increasing the SSA and average pore size [24]. As presented in Figure 3 (a), the specific capacitance normalized by SSA, suggesting the effect of pore size, irrespective of surface area. Notably, the volumetric capacitance increased ~1.5-fold (from 55 to 80 F/cm^3) when microporous carbon with pores <1 nm were employed [22]. According to the Monte Carlo simulation, the anomalous increase in capacitance with decreasing pore width can be ascribed to the exponential screening of the electrostatic interactions of the ions inside the pore as well as the image-charge ionic attraction to the pore surface [25]. Thus, it was recently reported that the pore size and carbon nanostructure (rather than the SSA) played an important role in increasing the specific capacitance [26]. Due to recent developments in various advanced *in-situ* spectroscopic and simulation techniques, the understanding of the physical processes and origin of the charge storage mechanisms in carbon-based materials is of special interest.

Conway's work suggests that various faradaic reactions can result in capacitive electrochemical features as shown in Figure 3 (b) [10] such as (1) underpotential deposition, (2) redox pseudocapacitance (normally observed in $RuO_2.nH_2O$), and (3) intercalation pseudocapacitance (observed in V_2O_5, TiO_2, Nb_2O_5). A brief description on "pseudocapacitance in metal oxides" can be found in recent literature [27]. Underpotential deposition is defined as the adsorption of metal ions onto the surface of other metal ions well above their redox potential. For example, the adsorption of lead onto the surface of a gold electrode [21, 28]. In redox pseudocapacitance, the charge is stored through surface or near-surface charge transfer reactions. An intercalation pseudocapacitance mechanism has been recently proposed whereby

electrolyte ion intercalation in the tunnels or layers of a redox-active material is accompanied by a faradaic charge transfer without a change in the original crystal structure.

The charge kinetics of pseudocapacitive materials can be characterized by estimating the capacitive and diffusion-controlled charge contributions to the total charge stored by the electrode using cyclic voltammetric data at various scan rates. Generally, the charge storage mechanism can be determined from the dependence of the current (*i*) on the scan rate (*v*) [29]:

$$i = a\nu^{b} \qquad (1)$$

where a and b are adjustable parameters and b is determined from the slope of the plot of log(i) vs. log(ν). Typically, b = 0.5 and corresponds to the diffusion-controlled faradaic intercalation process, suggesting typical battery behavior where the current is proportional to the square root of the sweep rate ($\nu^{1/2}$) according to the equation:

$$i = nFAC^{*}D^{1/2}\nu^{1/2}(\alpha nF/RT)^{1/2}\pi^{1/2}\chi(bt) \qquad (2)$$

where C* is the surface concentration of the electrode material, α is the transfer coefficient, D is the chemical diffusion coefficient, n is the number of electrons involved in the electrode reaction, A is the surface area of the electrode material, F is the Faraday constant, R is the molar gas constant, T is the temperature, and the function (bt) represents the normalized current. On the other hand, for the capacitive process, the current response is directly proportional to the scan rate (*b* = 1). Generally, the total charge stored in the electrode is the sum of the currents resulting from capacitive ($k_1\nu$) and diffusion-controlled ($k_2\nu^{1/2}$) faradic processes. Thus, equation (1) can be modified to:

$$i = k_1\nu + k_2\nu^{1/2} \qquad (3)$$

The current at a fixed potential is therefore equal to the sum of the capacitive ($k_1\nu$) and diffusion-controlled ($k_2\nu^{1/2}$) contributions [6a]. Constants k_1 and k_2 can be determined by plotting

$i/v^{1/2}$ versus $v^{1/2}$ and measuring the slope and the y-axis intercept point of the straight line, respectively.

Notably, there are no standardized methods to evaluate the capacitive performance of SC electrode materials used in different techniques (three-electrode vs. two-electrode configurations, different electrode thickness, CC discharge vs. CV curves, discharge current intensity, and voltage scan rate) that yield widely varying results. There are many excellent reviews explaining these issues in great detail [30]. Moreover, the performance of macroscale SCs is usually evaluated by their gravimetric capacitance, energy, and power densities [31]. On the other hand, for microscale supercapacitors (MSCs), the mass of active materials is often very small and the limited space is a key constraint. Thus, volumetric/areal capacitance and energy and power densities based on volume/area are more meaningful evaluating parameters. Furthermore, for portable and wearable device applications, the performance stability of the FSSCs under different mechanical bending, twisting, compressing, stretching, and extreme environmental conditions (high or low temperature and moisture) is also an important performance metric. These conditions mainly depend on the substrates and polymer gel electrolytes. Thus, the third section briefly describes advancement in flexible substrates for FSCs.

3. Current advances and challenges in flexible electrodes

The most crucial factor in fabricating flexible SCs is the use of flexible electrodes (flexible substrate) with high electrical conductivity to ensure fast charge-discharge. Considering recent developments, the fabrication of flexible electrodes can be divided into two main categories: (i) flexible free-standing films of active materials and (ii) supporting/depositing active materials on flexible substrates. In this section, we highlight recent developments in flexible electrodes for all-solid-state SCs.

3.1 Free-standing flexible electrodes

An emerging approach for fabricating flexible electrodes is to develop free-standing or self-standing films of active materials. This approach avoids the use of current collectors, conductive additives, and binders, considerably reducing the weight of the final device. Thus, the complete volume is utilized, leading to excellent volumetric capacitance and energy density of the SC devices. From a volumetric perspective, manufacturing solid-state SC devices with free-standing electrodes has been demonstrated as an excellent strategy for the best utilization of the materials [32]. Recently, numerous solution-processing methods have been presented to fabricate free-standing SC electrodes based on carbon materials [33], especially carbon nanoparticles, graphene [34], and carbon nanotubes (CNTs) [35]. Compared to other carbon materials, CNTs are excellent electrode materials, especially for FSSCs, due to their high SSA (1240–2200 m^2/g), high electrical conductivity (10^4–10^5 S/cm), and controllable regular pore structure [36]. Moreover, CNTs possess a high aspect ratio, which provides long continuous conductive paths and ensures high flexibility. Vacuum filtration is one of the most widely used methods in CNT film preparation that can be easily achieved in a laboratory with simple equipment. However, the areas of CNT films prepared via this process are limited by the size of the filter. The resultant flexible CNT film, also known as buckypaper, presented desirable conductivity and specific areas and can be directly used as both the current collector and the active material for the FSSC [35]. Thus, Kang et al. [37] deposited CNTs onto a bacterial nanocellulose substrate through a vacuum filtering process to afford paper with high flexibility, a large SSA (460 m^2/g), and good chemical stability (Figure 4 (a, b)). The assembled FSSC exhibited a high specific capacitance of 46.9 F/g at a scan rate of 0.1 V/s and excellent stability with <0.5% loss of capacitance after 5000 charge-discharge cycles at a high current density of 10 A/g shown in Figure 4 (c).

With many similarities to CNTs, including a large SSA, good electronic and mechanical properties, and chemical stability [38], graphene has also been investigated for its potential as

an electrode in SCs [39]. Recently, Weng et al. [40] prepared graphene-cellulose paper (GCP) membranes by vacuum filtration of the graphene suspension, which exhibited great advantages for use as freestanding and binder-free electrodes for flexible SCs. These GCP-based SCs exhibited a high areal capacitance of 46 mF/cm^2 for the complete device under highly bent conditions. Freestanding, flexible, and transparent graphene paper was also prepared from a microwave plasma-enhanced CVD process for optoelectronic application, [41]. SCs based on flexible transparent graphene exhibited good electrochemical performance with high specific capacitance (3.3 mF/cm^2), volumetric energy (430 $\mu Wh/cm^3$), and power density (190 mW/cm^3). The remarkable electrochemical performance of the device was attributed to the ultrathin graphene flakes that provide large effective areas, good conductivity, and 3D transport paths for both ions and electrons. Despite these successful results, the individual graphene sheets begin to aggregate and restack during the fabrication process due to the interplanar π–π interactions and van der Waals forces between the graphene layers. This agglomeration reduces the surface area of the graphene films and the diffusion of the electrolyte ions, which results in a decrease in the electrochemical performance. Therefore, a number of strategies have been developed to prevent aggregation of the graphene sheets to increase the surface area and promote transport of electrolyte ions. These include the addition of spacers [42] and crumpling of the graphene sheets [43].

Wang et al. [44] reported the synthesis of reduced graphene oxide/carbon black (rGO/CB) hybrid self-standing films by a simple vacuum filtration method. The restacking of individual graphene sheets was considerably reduced by the CB spacers, resulting in a significant increase in electrochemical performance due to an open structure for charge storage and ion transport. The synthetic effects of the rGO sheets, CB, and the interlayer water led to a large accessible surface area for the electrolyte. Moreover, the uniformly distributed CB particles between the graphene layers prevented compact restacking of the rGO sheets and also provided electrical contact between the base planes of the rGO sheets. As-fabricated FSCs

with an rGO/CB hybrid film and polyvinyl alcohol (PVA)/H_2SO_4 gel on a Au-coated polyethylene terephthalate (PET) substrate presented a specific capacitance of 112 F/g at a scan rate of 5 mV/s and excellent rate performance with a specific capacitance of 79.6 F/g at a high scan rate of 1 V/s. Moreover, the FSSC exhibited good cycling stability with 94% capacitance retention after 3000 cycles in the normal state and 2000 cycles in the bent state. However, CB is only an additive and can only contribute a very small amount of capacitance to the whole device. Furthermore, compared to the intercalation method, solution-based strategies could be more effective in reducing the agglomeration of graphene sheets in terms of simplicity, effectiveness, processing, and cost of materials. In this context, Choi et al. [45] developed functionalized rGO films by functionalizing graphene with Nafion using a supramolecular assembly approach (see Figure 4 (d)). The tight integration of the amphiphilic Nafion species prevents restacking of the individual graphene nanosheets (GNSs) and improves the interfacial wettability between the electrodes and electrolyte. Subsequently, the interconnected functionalized rGO networks provide continuous transport pathways for fast-ion transport. FSSCs based on functionalized rGO thin films with solvent-cast Nafion electrolyte membranes were thus fabricated. The specific capacitance for the functionalized rGO species was determined as 118.5 F/g and remained almost constant (90% retention at 30 A/g) with changes in current density ranging from 1 to 30 A/g. Flexibility was demonstrated by bending the device at high tensile strain during the operation as shown in Figure 4 (e). In addition, the bending experiment also demonstrated that there was no significant reduction in the initial capacitance at a bending radius of 2.2 mm, indicating good mechanical stability of the rGO-based FSSC (Figure 4 (f)). Yu and Dai [46] reported the synthesis of poly(ethyleneimine)-modified graphene sheet/acid-oxidized CNT hybrid films with interpenetrating network carbon structures and well-defined nanopores. The resulting free-standing multilayered CNT/graphene hybrid film exhibited a near-rectangular CV, even at an exceedingly high scan rate of 1 V/s, with an average specific capacitance of 120 F/g (three-electrode).

Due to the dependence of the carbon materials on electrical double-layer charge storage, the electroactive surface area, pore size distribution, and transport resistance of the electrolyte ions restricts their reversible capacitance. Thus, the actual gravimetric specific capacitance of carbon materials is usually <300 F/g and leads to a lower energy density [47]. To further increase the energy density, pseudocapacitive materials, with much higher capacitances than those of carbon materials due to redox reactions, have attracted great interest as potential substitutes for carbonaceous materials [6]. The commonly explored pseudocapacitor materials include transition metal oxides and hydroxides [48] such as RuO_2 [49], MnO_2 [50], Fe_3O_4 [51], and Nb_2O_5 [52] as well as CPs such as polyaniline (PAni) [53], polypyrrole (PPy) [54], and polythiophene (PT) [55]. However, these materials exhibit a number of disadvantages including particle aggregation, poor electrical conductivity (metal oxides), structural degradation, and poor cycling stability. On the other hand, carbon-based materials exhibit high electrical conductivity and a large surface area and make suitable scaffolds to support these pseudocapacitive materials. Hence, a combination of these high capacitance materials with flexible carbon materials should provide better performance results.

In this context, freestanding metal oxides/nitrides, polymer/CNT, and graphene hybrid electrodes were fabricated by simple methods, utilizing the synergistic effects from the high electrochemical performance of pseudocapacitive materials and the high conductivity and mechanical consolidation of the CNTs and graphene. Thus, mesoporous vanadium nitrite nanowire (VNNW)/CNT hybrid electrodes were fabricated by a simple vacuum filtration method [56]. Notably, the device composed of VNNW/CNT hybrid electrodes and a PVA/H_3PO_4 gel electrolyte only weighed 15 mg (whole device) and exhibited a high volume capacitance of 7.9 F/cm^3 and energy and power densities of 0.54 mWh/cm^3 and 0.4 W/cm^3, respectively, at a current density of 0.025 A/cm^3. Likewise, 3D intertwined nitrogen-doped carbon encapsulated mesoporous vanadium nitrite (MVN@NC) NWs were prepared by hydrothermal formation of V_2O_5 NWs and subsequent DA polymerization, vacuum filtration, and annealing under NH_3 [57].

Thus, the paper-like free-standing MVN@NC NW electrode exhibited a thickness of 45 μm without any mechanical support or additives. FSSCs were fabricated by sandwiching two freestanding MVN@NC NW film electrodes with PVA, sodium polyacrylate (PAAS), and KOH gel electrolyte (PVA/PAAS/KOH). This delivered a remarkable volumetric capacitance of 10.9 F/cm^3 at a current density of 0.051 A/cm^3 and a high energy density of 0.97 mWh/cm^3 with a power density of 2.72 W/cm^3 based on the entire cell volume. These excellent electrochemical performances can be attributed to the MVN NWs that provide abundant active sites that are accessible for charge storage and the N-doped carbon shell that suppresses electrochemical dissolution of the inner MVN NWs in an alkaline electrolyte.

In addition to metal oxides/nitrites, many efforts have been made to fabricate self-standing films of CPs such as PAni, PPy, and poly(3,4-ethylenedioxythiophene) (PEDOT). Among these compounds, PAni, known for its ease of synthesis, low cost, environmental friendliness, and potentially large pseudocapacitance originating from its redox reactions, is one of the most promising electrode materials for SC application [58]. However, PAni exhibits severe mechanical degradation caused by swelling and shrinkage during the doping and dedoping processes, which greatly limits its application as an electrode material for SCs. Therefore, to harvest the high capacitance of PAni while maintaining good cyclic stability, it is usually combined with carbon-based materials such as graphene and CNTs. Chi et al. [59] developed a new type of nanohybrid based on a 3D graphene hydrogel-loaded PANi supported on freestanding graphene paper by an inkjet printing method. The electrochemical performance of the FSSCs based on these electrodes were surprisingly improved with a specific capacitance of 864 F/g at a current density of 1 A/g and an areal capacitance of 190.6 mF/cm^2 at a current density of 0.5 mA/cm^2. Owing to the synergistic effect of the different components in this nanohybrid paper, the FSC exhibited an excellent energy density of 24.02 Wh/kg (at a power density of 400.33 W/kg), remarkable flexibility, and 96% cycling performance of over 1000 cycles. Chen et al. [60] reported the electrodeposition of PPy on a freestanding vacuum-filtered

CNT film as another example of a CP/carbon composite. The CNT/PPy freestanding film exhibited good mechanical properties (ultimate tensile strength: 16 MPa). Thus, FSSCs based on robust CNT/PPy films exhibited good flexibility, a high volumetric capacitance (4.9 F/cm^3; considering total volume of the device), and 95% long cycling stability after 10,000 cycles. In addition, the FSSC device displayed an energy density of 0.26 mWh/cm^3 and a power density of 0.15 W/cm^3, both of which are acceptable values for practical application.

Poly(3,4-ethylenedioxythiophene)/poly(styrenesulfonate) (PEDOT/PSS) is also considered as a promising material for SCs, mainly due to its high conductivity, good chemical and electrochemical stabilities, and excellent dispersibility in various solvents [61]. Liu et al. [62] prepared flexible rGO-PEDOT/PSS films by a simple bar-coating method. Notably, the device based on an rGO-PEDOT/PSS electrode retained 100% electrochemical performance under complete bending (180°) and rolled up (1000-fold) conditions. Moreover, a high areal capacitance of 448 mF/cm^2 was achieved at a scan rate of 10 mV/s when using a composite electrode with high mass loading (8.49 mg/cm^2), indicating its potential in practical applications.

In addition to graphene and CNT-based free-standing films, Li et al. [63] have recently developed a novel method for the synthesis of thick PEDOT:PSS films with the highest conductivity (1400 S/cm) and a low sheet resistance of 0.59 ohm/sq. An FSSC based on the PEDOT:PSS film delivered a volumetric capacitance of 50.1 F/cm^3 at a current density of 0.1 A/cm^3. Interestingly, the device sustained a high volumetric capacitance of 32.9 F/cm^3, even at an extremely high current density of 100 A/cm^3, suggesting exceptional rate capabilities. Moreover, the device displayed an outstanding volumetric energy density of 6.80 mWh/cm^3 at a power density of 100 mW/cm^3. Surprisingly, the device maintained an energy density of 3.54 mWh/cm^3 at a high power density of 12815 mW/cm^3, 3.15 mWh/cm^3 at a power density of 16160 mW/cm^3, and 3.15 mWh/cm^3 at a very high power density of 16160 mW/cm^3. Thus, the outstanding electrochemical properties of the FSCs were attributed to the excellent conductivity of the free-standing PEDOT:PSS films.

3.2 Substrate-supported flexible electrodes

The thickness of the electrode materials used in FSSCs is lower (<50 μm); the freestanding active material films are relatively fragile and can flake off the electrode after prolonged bending. To overcome this problem, many efforts have been made to support the active materials on flexible substrates. In this section, we provide a brief description of recent advancements in support substrates. These include coating and growing of active materials on flexible, porous, and light-weight substrates such as flexible metal substrates (SS, nickel, and titanium), carbon-based electrodes, and porous materials (conventional paper, textiles, and cable-type electrodes and bendable plastics).

3.2.1 Flexible metal substrates

Metal substrates have been extensively used as electrode substrates for SCs because they exhibit high electrical conductivity and good mechanical properties [64-67]. Various metal substrates such as SS [64], copper (Cu) [65], nickel (Ni) [66], and titanium (Ti) [67] provide high strength, good conductivity, and ease of preparation. In addition, the electrode configuration of electroactive materials that are directly synthesized on the substrate surface leads to an increase in SC energy density and flexibility. On the other hand, conventional powder-formed materials require additional binders, resulting in low energy density and mechanical durability [68]. Chodankar et al. [69] prepared porous nanostructured MnO_2 directly on a flexible SS substrate by chemical bath deposition (CBD) (Figure 5 (a-b)). FSSCs based on these flexible MnO_2 electrodes were assembled with a carboxymethyl cellulose (CMC)-Na_2SO_4) gel electrolyte and afforded a specific capacitance of 145 F/g with a specific energy of 16 Wh/kg. Moreover, the device displayed almost negligible loss in capacitance under different bending conditions as well as long-term stability over 2500 cycles. More importantly, a series combination of two MnO_2-FSC devices easily glowed up two light-emitting diodes (LEDs) for 135 s, further confirming the significant potential for application in different portable electronic devices. Nanoporous 3D $Cu(OH)_2$ nanorods grown directly on copper foil provide a large amount of

active sites for redox reactions that can be easily accessed by electrolyte ions [70]. The flexible and foldable asymmetric SCs based on $Cu(OH)_2$ as positive and activated carbon (AC) as negative electrodes delivered a high energy density of 3.68 mWh/cm^3 and a high power density of 5314 mW/cm^3. Practical applicability was displayed by lightning 26 LEDs with the tandem device. Similarly, Sheng et al. [71] reported interpenetrating graphene electrodes fabricated by electrochemical deposition of vertical GO on gold foil. The double-layer capacitor comprising these graphene electrodes exhibited a specific capacitance of 283 mF/cm^2 and a short resistor-capacitor time constant of 1.35 ms.

Despite these advancements, the conducting substrates used in FSSC electrodes (SS, Cu, and Al foil) are usually much thicker and heavier than the coated active material. Therefore, even if the gravimetric specific capacitance based only on the active materials is increased, the low mass loading will only lead to a marginal increase in capacitance for the whole device. Furthermore, the charges in the thick electrode materials cannot be conveniently transferred to the surface of the conducting substrates, thereby greatly decreasing the rate capability and capacitance of SCs with thick electrodes. This problem can be solved by using a 3D conductive structure as substrate to increase the loading mass of the electrode. Many studies have proposed the use of porous metallic substrates such as mesh or foams [72]. Huang et al. [73] demonstrated an easy and cost-effective strategy to fabricate stretchable SCs with high performance and excellent cycling stability by electrochemical deposition of PPy on smartly tailored stretchable SS meshes (Figure 5 (c)). The fabricated FSSC exhibited a capacitance up to 170 F/g at a specific current of 0.5 A/g and could be effectively enhanced to 214 F/g with a 20% strain. Notably, the device can be operated at a very high scan rate up to 10 V/s in aqueous electrolytes. This value is significantly higher than that normally employed in PPy-based SCs. Furthermore, under stretching conditions (0% and 20% strains) the device still achieved significant capacitance retentions of 98% and 87%, respectively, at a very high specific current of 10 A/g after 10,000 cycles (Figure 5 (d)). The CV curves recorded at 10 mV/s

completely overlapped when the device was knotted, folded, and bent (Figure 5 (e); inset: corresponding digital photographs).This remarkable performance was attributed to the open porosity of the highly utilized PPy materials and the high electric conductivity of the mesh. Zhou et al. [74] prepared a core-shell heterostructure based on layered titanate NWs coated with nickel hydroxide nanosheets on a titanium mesh ($K_2Ti_4O_9$@$Ni(OH)_2$/Ti) by a simple nickel ion exchange reaction. The FSSCs were assembled with a $K_2Ti_4O_9$@$Ni(OH)_2$/Ti flexible electrode and KOH/PVA solid-state electrolyte. The device exhibited a specific capacitance of 5.8 mF/cm^2 at 5 mV/s with a retention rate of 92.5% after 2000 cycles and 92.7% after 10,000 cycles. Moreover, the $K_2Ti_4O_9$@$Ni(OH)_2$/Ti FSCs cell displayed an energy density of 4.8 mWh/cm^3 (0.72 mWh/cm^2) at a power density of 1.1 mW/cm^3 (0.16 mW/cm^2) and still retained 7.5 mWh/cm^3 (1.13 mWh/cm^2) at a power density of 0.32 mW/cm^3 (0.048 mW/cm^2). Notably, FSSCs displayed excellent mechanical integrity with no significant change in electrochemical performance after mechanical stress of more than 200 intentional bends to a radius of ~1.5 cm. Likewise, $NiCo_2O_4$ nanowire arrays (NWAs) on different flexible substrates, including nickel foam, carbon cloth, Ti-foil, and polytetrafluoroethylene tape, were prepared by Wang et al. [75]. The FSSC device assembled with the $NiCo_2O_4$ NWs on Ni-foam provided an areal capacitance of 161 mF/cm^2 at 1 mA/cm^2 with a capacity retention of 82% (137 mF/cm^2) after increasing the current density eightfold (8 mA/cm^2). In addition, the device exhibited good cycling stability under twisted and bent conditions over 3000 cycles. This high performance was attributed to the highly conductive 3D macroporous Ni foam, which enables efficient charge transport and accessible diffusion of the electrolyte. Recently, a hierarchical PPy@Co-Ni layered double hydroxide (CoNi-LDH) core–shell array was prepared by a two-step electrosynthetic method [76]. In this integrated configuration, the PPy core provided excellent conductivity, while the Co-Ni LDH shell acted as a protection layer to enhance the structural stability. The asymmetrical FSSC cell (PPy@LDH//RGO) presented an energy density of 46 Wh/kg at a power density of 2.4 kW/kg as well as the highest cycling stability (15.4% increase in capacitance after 20,000

cycles). The synergistic effect in this hierarchical core–shell nanostructure contributes towards the promising overall performance of the all-solid-state asymmetric SC device.

3.2.2 Paper-based substrates

Taking into consideration their conductivity and porosity, metallic porous substrates are considered good candidates for flexible SC application. However, the lower corrosive resistance of the metal limits this applicability. In addition, the heavy nature of the metallic current collector unusually increases the weight of the whole flexible SC device. On the other hand, carbon-based supporting substrates such as carbon paper, foam, and cloth exhibit higher electrical conductivity, lower corrosive resistance, and most importantly, better flexibility and lower weight. Thus, they are better candidates for the flexible SCs application. This section summarizes recent advancements in carbon-based flexible substrates for FSCs.

Carbon paper consists of regular arrangements of carbon microfibers (CMFs) into flat sheets with enormous nanoscale pores that provide a large surface area to host the electrode material. The single carbon fibers present in carbon paper are well connected to each other to form a conducting network that allows the formation of appropriate pore channels. These channels create an efficient electron transportation path as well as effective electrolyte access to the electrochemically active materials. Likewise, carbon nanofoams consist of a cluster-assembly of carbon strings in the form of a loose 3D web. Due to their porosity, mechanical integrity, and good conductivity, they have been widely used as substrates in fuel cells, SCs, and other applications. [77].

Various forms of paper are widely used in our daily life for hygiene and sanitation purposes, packaging, and decorating. In addition, paper applications have been expanded to flexible electronic devices such as photodiodes, transistors, circuits, and displays. Recently, several studies have demonstrated that paper can also be an excellent support for loading active materials to fabricate high performance SCs. Tao et al. [78] reported a solid-state SC with conventional Xerox paper by simple pencil drawing. The thin graphite sheets on paper provided

effective channels for electron transmission with a low resistance of 95 Ω/sq. The conductive organic material of PPy coated onto thin graphite sheets acted as the electrode material of the device. The as-fabricated SC exhibits a high specific capacitance of 52.9 F/cm^3 at a scan rate of 1 mV/s. In another investigation, high-purity single-walled carbon nanotube (SWCNT)/graphene flake ink was cast by a rod-rolling method on conventional paper and applied to the SCs [79]. Interestingly, at room temperature, the paper with the SWCNT/graphene ink provided lower sheet resistance (90.5 Ω/sq) than the paper with SWCNT (440.2 Ω/sq). Similarly, Zhang et al. [80] developed a new flexible SC in which the multi-walled carbon nanotubes (MWCNTs) were coated onto microfibrillated cellulose (MFC) doped with solid polyelectrolyte [polyethylene oxide (PEO) and lithium chloride]. In this design, the MWCNTs acted as the active material while the MFC coated with polyelectrolyte served the dual role of electrolyte and separator. Both the electrode and separator sheets afforded good conductivities (~8.2×10^{-4} S/cm and 6.8×10^{-4} S/cm) and hence, an acceptable specific capacitance of 154.5 mF/cm^2 at 20 mV/s. In addition, the paper-based device displayed excellent mechanical properties with a tensile strength of 1 MPa and a Young's modulus of 123 MPa, which are significantly better than those observed for conventional liquid or gel-based soft SCs.

The performance of these paper-based SCs is still limited but can be further enhanced by adding pseudocapacitive materials in carbon-based SCs. Yun et al. [81] reported an FSSC based on PAni/Au/paper structures that could be easily scaled-up to large-scale production. Interestingly, the device enhanced the energy density to 0.01 Wh/cm^3 (comparable to that of AC-based SCs with an aqueous electrolyte) and a power density of ~3 W/cm^3. Furthermore, the cell exhibited excellent long-term cycling stability over 10,000 charge/discharge cycles with 100% Coulombic efficiency. On the other hand, metal oxides are the best pseudocapacitive candidates to combine with carbon materials and hold great promise in increasing the overall

performance of the device. Recently, a paper-based asymmetric device was also developed with Ni/MnO_2 filter paper as the positive electrode and Ni/AC filter paper as the negative electrode, separated by a PVA-Na_2SO_4 electrolyte [82]. Impressively, the asymmetric device exhibited a volumetric energy density of 0.78 mWh/cm^3 as well as superior flexibility under different bending conditions with practical demonstration (see Figure 5 (f)). A paper-based all-solid-state flexible planar SC using a PEDOT:PSS-CNT/Ag electrode was accomplished using the inkjet printing technique [83]. The device delivered the best rate capability up to 10,000 mV/s and a fast frequency response (relaxation time constant τ_0: 8.5 ms). A high volumetric specific capacitance of 23.6 F/cm^{-3} with long cycle stability of ~92% capacitance retention after 10,000 cycles was also displayed.

3.2.3 Textile substrates

Textile-based electronics such as e-textiles, smart textiles, and wearable electronics can be potentially utilized in the future for high-tech sportswear, workwear, portable energy systems, health monitoring systems, and military camouflage [84]. These integrated devices for wearable electronics need an energy source and thus, textile-based SCs hold great promise for application in these systems (Figure 6 (a)). Common textiles such as cotton, polyester, and acrylonitrile are reusable, cheap, flexible, and hydrophilic [85]. When considering flexibility and stretchability, textile-based substrates have many advantages over paper based-substrates [85]. For example, the porous structure of these textiles provides abundant support for the loading of active materials and facilitates the rapid absorption of electroactive materials due to their hydrophilic nature. This results in a much higher areal mass loading of active materials and therefore a higher areal power and energy density [86]. Low cost and highly efficient textile-based SCs are already being integrated into prototype wearable electronics. For instance, CNTs have been directly grown on carbon cloth to fabricate conducting electrodes with 3D porous network architecture [87]. The assembled FSSCs exhibited extraordinary electrochemical performances including a capacitance of 106 F/g (areal capacitance: 38.75 mF/cm^2), an

ultralong cycle life (100,000-fold; 99% capacitance retention), a high energy density (2.4 $\mu Wh/cm^2$), and a high power density (19 mW/cm^2). In addition, the device sustained its excellent performance even under very harsh conditions such as shape deformation (bending, folding, etc.), high mechanical pressure (63 kPa), and a wide temperature window (up to 100 °C). Nitrogen-doped single crystalline silicon carbide nanowires (SiCNWs), directly grown on flexible carbon fabric by chemical vapor deposition (CVD) method as shown in Figure 6 (b) [88]. The FSSC cell fabricated with this unique material displayed an areal capacitance of 4.7 mF/cm^2, which translates into an excellent power density of 72.3 mW/cm^2 (considerably higher than that observed in electrolytic capacitors) and an energy density of 0.12 $\mu Wh/cm^2$ together with superior rate ability and cyclability (~100% after 10,000 cycles; Figure 6 (c-e)). Notably, the SiCNW-based textile FSSC can be operated at an ultrahigh rate (up to 30 V/s), which is two orders of magnitude higher than that of conventional SCs. Further attempts were made to improve the electrochemical performances of textile-based SCs by fabricating hybrid composite materials such as carbon-metal oxides and/or CPs. Jin et al. [89] introduced a novel approach for the functionalization of carbon fabric by a simple acid-oxidation and heat-treatment method. This approach created oxygen-functional groups on the carbon fabric that in turn added extra capacitance through a pseudocapacitive mechanism and provided additional potential window. Thus, the symmetric cells fabricated with these functionalized electrodes could be cycled in a voltage window up to 1.6 V and provided a capacitance of 134.8 F/cm^2 (or 2.41 F/cm^3) with an energy density of 0.83 mWh/cm^3 and a power density of 1.58 W/cm^3. These values are higher than those observed for most previously reported CF-based SCs. MnO_2 is the most successful and promising pseudocapacitive material in terms of cost-effectiveness, high performance, and environmental friendliness. A lightweight MnO_2/CNT-based textile SC was developed by Ko et al. [90]. A very simple fabrication process was implemented, comprising the deposition of MWCNTs onto commercial textiles using the “dip and dry” method and subsequent

electrodeposition of MnO_2 nanosheets onto the MWCNTs. Due to the strong van der Waals forces and carboxyl groups, MWCNTs strongly adhered to the surface of the textile fibers through hydrogen bonds and washing and other mechanical processes did not damage these textiles. Interestingly, the FSSC cell displayed a specific capacitance of 324 F/g at 0.5 A/g and an energy density of 7.2 Wh/kg with excellent cycling stability of ~100% capacity retention over 5000 cycles. Recently, Javed et al. [91] developed a zinc sulfide-based textile SC using a hydrothermal method. The ZnS-textile-based symmetric SC exhibited excellent electrochemical performance with a high specific capacitance of 540 F/g (areal capacitance: 56.25 F/cm^2) at a scan rate of 5 mV/s with good rate capability and excellent cycling stability (94.6% retention of the initial capacitance after 5000 cycles) at a constant current density of 0.8 mA/cm^2. A high energy density of 51 Wh/kg at a power density of 205 W kg was also achieved, indicating excellent ion accessibility and charge storage ability. Wang et al. [92] reported the growth of vertically aligned graphene nanosheets (VAGNs) decorated with Co_3O_4 nanoparticles directly on the carbon fabric for extraordinary SSCs as presented in Figure 6 (f). The Co_3O_4@VAGNs hybrid exhibited an excellent specific capacitance of 3480 F/g (close to the theoretical value of 3560 F/g). This value was attributed to the VAGN supported onto the carbon fabric, which served as an excellent backbone. A solid-state symmetric cell based on a Co_3O_4/VAGN/carbon fabric cell delivered a capacitance of 580 F/g under normal and bending conditions with good cycling ability (86.2% capacitance retention after 20,000 cycles; Figure 6 (g-i)). Moreover, the cells exhibited an excellent energy density of 80 Wh/kg that was maintained at 27 Wh/kg at a high power density of 20 kW/kg.

3.2.4 Yarn-like (fiber) substrates

Fiber SCs are small lightweight 1D wires with diameters ranging from micrometers to millimeters. Fiber SCs have several advantages over conventional planar SCs, including great design versatility (allows fabrication into various desired shapes that can be located at different places), high flexibility (allows them to be woven or knitted into smart textiles with excellent

wearability), and good compatibility with other energy harvesting devices and sensors to form integrated multifunctional systems [93, 94]. Generally, planar SCs are fabricated as a bulk powder or thin film. On the other hand, yarn-electrode assembly is usually constrained by the geometrical configuration and mechanical flexibility of the substrates. Normally, highly conductive fibers such as metal wires and carbon-based fibers are used as a current collector to grow different nanomaterials that can be directly used as electrodes in SCs. Interestingly, they also present a large specific volume power density that cannot be attained by planar SCs. For fiber SCs, the structures are numerous and much effort has been made in designing novel device constructions. One simple design consists of two fiber electrodes coated with gel electrolyte in parallel, with a space on the flexible substrate. Graphene-based materials are more suitable for wire- or yarn-based SCs due to their excellent electrical conductivity and mechanical flexibility. Recently, Huang et al. [95] developed a graphene fiber-based SC from wet-spun graphene fibers. The graphene fibers, which were several meters in length, were wet-spun in a coagulation bath of $CaCl_2$ aqueous ethanol solution and subsequently reduced with hydrazine. Two different-sized fibers (diameters: 35 μm and 100 μm), prepared from hydrogen iodide (HI) and dihydrogen dihydride (N_2H_4) reducing agents, displayed electrical conductivities of 10,000 S/m and 700 S/m, respectively (Figure 7 (a, b)). The planar cell design was used to fabricate fiber-based SCs (Figure 7 (c)) with a capacitance of 2.5 mF/cm^2 and 3.3 mF/cm^2 at 0.1 mA/cm^2 for the 100-μm and 35-μm fibers, respectively, demonstrating the adverse effect of large-sized fibers. The capacitance of the graphene fiber electrode can be further improved by combining it with a conjugated polymer. To this end, the graphene fibers were uniformly coated with PAni. Surprisingly, the resultant fiber SC displayed a capacitance of 66.6 mF/cm^2, representing a 22-fold improvement. Likewise, Kou et al. [96] developed a yarn SC using a coaxial wet-spinning strategy to prepare polyelectrolyte-wrapped (CMC) carbon nanomaterial (graphene, CNTs, and their mixture) core-sheath fibers that could be directly applied as contactable and interweaving yarn SC electrodes as illustrated in Figure 7 (d-e). The

polarized optical image reveals the presence of homogeneous CMC on the GO core-sheaths. The CMC is ionically conductive, while the presence of the electrically insulating polyelectrolyte avoids any risk of short-circuits. First, GO@CMC core-shell fibers were prepared by mixing aqueous solutions of graphene oxide (GO) and CMC into a mixture of ethanol/water solution with $CaCl_2$. The GO was further reduced by acid to afford the rGO@CMC fibers. These presented a conductivity of 7000 S/m, while being completely insulated when measured from the CMC side. The solid-state flexible two-ply yarn SC displayed a capacitance and energy density of 177 mF/cm^2 (158 F/cm^3) and 3.84 $\mu Wh/cm^2$ (3.5 mWh/cm^3), respectively, which are superior to values afforded by commercial capacitors (Figure 7 (f)).

In addition to self-assembled CNT and graphene fibers and their composite fiber electrodes, wire electrodes can also be fabricated by directly growing active materials on the fiber conductive current collectors. Carbon, nickel, and titanium fibers are commonly employed as conductive substrates, while the metal oxides include $ZnCo_2O_4$, $NiCo_2O_4$, Co_3O_4, and $Ni(OH)_2$ [97].

Although the above-discussed SCs exhibit many advantages, they are not real fiber-SCs due to the use of planar substrates as support. True yarn or fiber SCs should be of single wire form or cable-type architecture. Recently, Wang et al. [97] developed a fiber SC by assembling two nickel wires anchored with a $NiCo_2O_4$ nanosheet, whereby one wire was wound around the other and a PVA–KOH gel electrolyte filled the middle space. No obvious change was recorded in the electrochemical performance of the device under harsh bent conditions due to the unique spring-like structure of the material. However, there is possibility of electrolyte damage during bending due to the stress between the metal current collectors. Similarly, titania nanotubes were grown on titanium NWs by the anodization method [98]. In this configuration, pseudocapacitive titania nanotubes provided a high surface area and also acted as a separator between the Ti-fiber and the outmost CNT yarn or sheet. These electrodes, processed in FSSCs with a CNT

sheet electrode, displayed a capacitance of 1.84 mF/cm^2, which is approximately triple that afforded with a single CNT yarn electrode. Remarkably, this wire-shaped SC can be successfully woven into various textiles and connected in series or parallel to meet a large variety of specific energy demands.

The mechanical stability of a fiber SC can be further improved by fabricating cable-type SCs using plastic and carbon fibers instead of metal fibers as the substrate for active materials. A cable-type fiber SC based on PPy-MnO_2/SWCNT-coated carbon fibers as the electrode was assembled with excellent mechanical stability [99]. In this composite, the conducting SWCNT backbone provided excellent conductivity, while the active mesoporous flower-like MnO_2 nanoplates and PPy conductive wrapping layer improved the electrical conductivity and added extra pseudocapacitance. However, this kind of SC design exhibits low capacitance due to reduced utilization of the active materials. Therefore, it is very important to choose a proper cell design that maximizes the use of the active materials. To this end, a novel fiber SC with a coaxial structure that possesses the highest contact area between the active materials has attracted significant interest. Yu et al. designed a coaxial SC using CuO@AuPd@MnO_2 core-shell nanowhiskers grown on copper wire and foil as inner and outer electrodes, respectively [100]. The as-fabricated coaxial SCs take full advantage of both the inner and outer active materials, thus providing many more electrochemically active sites for the reversible redox reactions. Notably, high flexibility was also exhibited and electrochemical performance could be well retained when tested under different bending angles.

Preparing an industrially weavable and knittable conductive yarn with high capacitance is still a challenge. To this end, soft conductive yarns were produced by a scalable method with the use of a twist-bundle-drawing technique. These yarns are sufficiently mechanically robust to be knitted into a cloth by a commercial cloth knitting machine as illustrated in Figure 8 (a, c) [101]. Furthermore, these conductive yarns were coated with rGO and subsequently, MnO_2 nanosheets and PPy were deposited on it. The cable-type SCs fabricated with these composite

yarns exhibited capacitances of 31 mF/cm (length capacitance) and 411 mF/cm^2 in an all solid-state two-electrode cell, which are considerably higher than previously reported values (Figure 8 (b)). Moreover, the symmetric solid-state SC displayed energy densities of 9.2 μWh/cm^2 and 1.1 mWh/cm^3 (both normalized to the whole device) with a long cycle life over 5000 cycles. Finally, a large-sized (15 cm x 10 cm) yarn-type FSSC was assembled on a loom and a woolen wrist band was knitted to form a pattern as demonstrated in Figure 8 (d). Moreover, many yarn-FSSCs were fabricated to elucidate the effect of the number of yarns. Recently, Le et al. [102] developed a coaxial-fiber FSSC, comprising MWCNTs coated onto CMF bundles as the core electrode, with carbon nanofiber (CNF) paper as an outer electrode and polymer gel as the electrolyte (Figure 8 (e)). The devices exhibited a length capacitance of 6.3 mF/cm with a 230-μm sized core electrode and an energy density of 0.7 μWh/cm (9.8 μWh/cm^2) at a power density of 13.7 μW/cm (189.4 μW/cm^2), as depicted in Figure 8 (f). Moreover, negligible changes in the CV characteristics (Figure 8 (g)) were observed after severe bending (180°), revealing that the components of the devices (CMFs, MWCNTs, and CNFs) soaked with polymer gel electrolyte are highly flexible.

Thus, many fiber/yarn/cable-type SCs have been successfully explored. The discussed results suggest that textile-based energy storage systems with high energy density and mechanical robustness can be achieved using a binder free approach with nanostructured metal oxides as active materials and CNT graphene fibers as substrates. Moreover, there is a great need for the development of new nanostructured active materials with high electron conductivity, abundant electrochemical sites, and novel fiber current collectors with strong mechanical stability and ultra-high flexibility to develop fiber-shaped flexible energy storage devices and wire-based integrated energy systems with excellent performances.

3.2.5 Polymer based non-conducting substrates

Low-cost, excellent bendability and comparatively light plastic substrates such as PET [103], polydimethylsiloxane (PDMS) [104], and ethylene/vinyl acetate copolymer (EVA) films [105] are considered as a promising support for active materials. PET is widely used due to its easy availability, excellent water and moisture repellent properties, and transparent nature. Several works on PET-based flexible SCs have been reported [106]. A transparent FSSC based on graphene was also attempted [107]. A cell with an optical transmittance of ~67% at a wavelength range of 500–800 nm was realized, suggesting great potential for application in transparent flexible electronics. In addition, the cell exhibited good flexibility with a retention of 92.4% of its initial capacitance under a bending angle of 80°. The decrease in capacitance under bending was ascribed to the buckling of the graphene electrode during compression. On the other hand, a two-fold increase in the graphene-based FSSC was reported by Choi et al. [108] where functionalized reduced graphene oxide (f-rGO) thin films were used as the electrode and solvent-cast Nafion electrolyte membranes as the electrolyte and separator. Moreover, the f-rGO cell exhibited a relaxation time that was four-fold faster than that of the rGO-based cell as well as higher capacitive behavior at the low-frequency region. These results were attributed to facilitated ionic transport at the electrical double layer due to the interfacial engineering of rGO via Nafion. However, the capacitance of graphene is still limited, thereby hindering the use of these thin films in a wide-range of applications. Fei et al. [109] explored a new strategy of mixing CB with graphene and using cross-linked PVA-H_2SO_4 porous gel electrolytes. In this composite, CB nanoparticles were uniformly distributed in the GNSs, thereby greatly improving the active surface area and ion transportation in pristine graphene. In addition, the porous PVA-H_2SO_4 membrane improved the equilibrium swelling ratio of the electrolyte and provided interconnected ion transport channels. The symmetric cell was designed by casting a graphene/CB composite on PET foil and afforded a specific capacitance of 144.5 F/g at 0.5 A/g with good capacitance retention (67.9% from 0.2 to 4 A/g). More importantly, when the effect of

temperature was investigated, a capacitance retention of 78.3% after 1000 cycles was displayed at 70 °C. A new on-chip MSC based on MnO_x/Au multilayers on a PET substrate was introduced by Si et al. [110]. The digital photograph of the assembled device is presented in Figure 9 (a). These MSCs exhibited an energy density of 1.75 mWh/cm^3 and a maximum power density of 3.44 W/cm^3 (Figure 9b). Moreover, at a high scan rate of 1 V/s, the device displayed a volumetric capacitance of 32.8 F/cm^3, which is almost two-fold higher than that of the bare MnO_x electrode (19.23 F/cm^3). These excellent electrochemical responses correspond to the improved electrical conductivity of MnOx due to the incorporation of gold. The MnOx/Au multilayered MSC also exhibited good long-term cycling stability with a capacitance retention rate of 74.1% over 15,000 cycles (Figure 9 (c)). Notably, the cell provides good flexibility with negligible change in the CV shapes under different bending conditions (Figure 9 (d)), suggesting great potential for application in integrated micro-devices. On the other hand, Xiao et al. [111] developed a core-shell structure by depositing MnO_2 on carbon fiber and a planar self-powered SC device was assembled on a PET substrate. The device exhibited excellent electrochemical performances including a high rate capability with a scan rate up to 20 V/s, high volume capacitance of 2.5 F/cm^3, and an energy density of 0.22 mWh/cm^3. Figure 9 (e and f) display the digital photographs of a MnO_2@carbon fiber single cell under different bending conditions and its corresponding CV curves, respectively. Interestingly, in these CV curves, no significant change can be observed under different bending conditions. To meet the energy and power requirements, cells packaged either in series, parallel, or a combination of both may be a viable solution. Figure 9 (g) presents a module fabricated from 3 cells connected in series integrated with a triboelectric generator through which the SC can be charged. Interestingly, a practical demonstration was provided where the movement of a human hand (Figure 9 (h)) charged the SC and powered a LED. These results suggested great potential for application in self-powered micro/nanosystems.

Kurra et al. [112] proposed an FSSC fabrication procedure based on PEDOT on a plastic polyethylene naphthalate (PEN) substrate using conventional photolithography and electrochemical deposition techniques. Surfactant-assisted electropolymerization allows the synthesis of porous conducting PEDOT electrodes. The electrodes were first tested in aqueous H_2SO_4 electrolytes and displayed excellent electrochemical performances (tunable frequency response and energy density). Specifically, an ultrahigh scan rate capability up to 500 V/s was achieved with a crossover frequency of 400 Hz at a phase angle of ~45°, values comparable to those afforded by carbonaceous-based materials. When PEDOT SCs were tested with a polymer gel electrolyte, they presented an areal cell capacitance of 5 mF/cm^2 with a volumetric stack capacitance of 33 F/cm^3 (retention: ≤80% over 10,000 cycles with 100% Coulombic efficiency). Moreover, the device exhibited an energy density of 7.7 mWh/cm^3, a value that is comparable to that afforded by lithium-based thin film batteries and superior to the current state-of-the-art carbon and metal oxide-based FSCs. Polyimide (PI) is another polymeric substrate that has recently gained much attention for its potential as a flexible substrate in FSCs [113]. Recently, In et al. [114] developed a flexible MSC based on laser carbonization of PI sheets. Localized pulsed laser irradiation rapidly converts the pristine PI surface into an electrically conductive porous carbon structure under ambient conditions. Thus, the PI sheet acts as a flexible substrate as well as a precursor for carbonization. The electrical properties and morphology of the carbon nanostructure were optimized by various laser parameters. The FSC was fabricated by drawing interdigitated electrode patterns directly on the PI sheets and using a PVA-phosphoric acid mixture as the gel electrolyte. The device exhibited a specific capacitance of 800 $\mu F/cm^2$ at a voltage scan rate of 10 mV/s with good capacitance retention under mechanical bending. Interestingly, this laser-based patterning technique avoids the use of tedious photolithographic patterning of porous carbon and metal current collectors. Similarly, Peng et al. [115] prepared two FSCs based on porous vertically aligned in-plane graphene on a PI substrate using a laser induction technique. The device displayed a capacitance of 9.11

mF/cm^2 at a current density of 0.01 mA/cm^2 with excellent cycle stability (98% retention over 8000 cycles). Moreover, the areal capacitance was well-maintained after 7000 bending cycles at a radius of 14 mm, suggesting negligible effect from repeated bending.

Several other flexible polymer substrates were tested as substrates for SSCs such as polycarbonates (PCs) [116], polyethersulfone (PES) [117], and parylene [118]. To date, the afforded results reinforce the assertion that polymersubstrate-based FSCs are promising candidates as energy storage devices in flexible, portable, and wearable electronics. However, despite their high flexibility and good ion accessibility, the electrical conductivity of these electrodes has been limited by the insulating properties of the substrates used, which affect the charge-discharge rate of the SCs. In addition, the total SC device weight increased due to the use of insulating substrates, leading to a decrease in capacitance per unit weight. Table 1 lists various flexible substrates used for the fabrication of solid-state devices and their respective electrochemical performances [70, 72, 75, 76, 91, 109, 110, 119-172].

4. Recent trends in the development of gel electrolytes

Solid-state electrolytes are key components in SCs and considerably affect electrochemical properties such as energy density, rate capability, and cycling stability [14, 15, 20, 26]. The advantages of SCs based on solid-state electrolytes over those based on conventional liquid electrolytes include easy and inexpensive packaging, simple fabrication steps, and no leakage of toxic electrolytes. In addition, solid-state electrolytes provide good mechanical stability that allows different flexible and bendable SCs to be successfully assembled in various applications. They also play a dual role in SC devices such as ionic conducting media and electrode separators. The key to develop high performance FSSCs is a suitable solid-state electrolyte that exhibits high ionic conductivity; high chemical, electrochemical, and thermal stabilities; good mechanical strength; and dimensional stability. Three main types of solid-state electrolytes are used in SCs, namely ceramic electrolytes (CEs)

[173], gel-polymer electrolytes (GEs) [174], and polyelectrolytes (PE). Among these, GEs are extensively employed in SCs due to their relatively high ionic conductivity (10^{-4} to 10^{-3} S/cm under ambient conditions) [174].

Normally, GEs are composed of a polymeric host (PVA), a solvent as the plasticizer, and a conducting electrolytic salt where the polymer serves as a medium that swells in the solvent and the ions travel through the solvent. Some studies have termed these GEs as quasi-solid-state electrolytes due to the presence of a liquid phase [175]. Polymer matrices are also commonly used to prepare GEs for FSCs. These include PVA [176], poly(methyl methacrylate) (PMMA) [177], poly(polyacrylate) (PAA) [178], poly(amine-ester) (PAE) [179], PEO [180], polyacrylonitrile (PAN), poly-(ethylene glycol) blending poly(acrylonitrile) (PAN-b-PEG-b-PAN) [181], poly(vinylidene fluoride) (PVdF), and poly(vinylidene fluoride-co-hexafluoropropylene) (PVdFco-HFP) [182]. On the other hand, based on the electrolyte salts, the GEs are classified as Li-ion GEs (e.g. LiCl), proton conducting GEs (e.g. H_2SO_4, H_3PO_4), and alkaline GEs (e.g. KOH). These exhibit a low dissociation energy and provide free/mobile ions. In this section, we discuss current advancements in GEs to develop different-shaped and high performance FSCs. The section is divided into four sub-sections: (1) Aqueous gel polymer electrolytes (AGEs), (2) Organic gel polymer electrolytes (OGEs), (3) Ionic liquid gel polymer electrolytes (IL-GEs), and (4) Redox-active gel polymer electrolytes (RGEs).

4.1 Aqueous gel polymer electrolytes (AGE)

As specified before, AGEs have been extensively studied for their potential in FSSC application due to their high ionic conductivity, low-cost, and non-toxicity. AGEs comprise a host polymer matrix (PVA, PMMS, PAA, and PEO), water as a plasticizer, and an electrolytic salt that can be a strong acid (H_2SO_4 and H_3PO_3), strong alkaline (KOH), or neutral (LiCl, Na_2SO_4). AGEs are also known as hydrogel polymer electrolytes where 3D polymeric networks trap water molecules through the surface tension. The degree of plasticization depends on the compositional polymer/plasticizer ratio that affects the glass-transition temperature of the AGEs.

Generally, high performance FSSCs require good interfacial contact between the electrode and gel-electrolyte, thus, the interfacial features of the AGE and electrode materials are key components. PVA has been widely investigated as a polymer matrix for AGEs due to its ease of preparation, high hydrophilicity, good film forming properties, non-toxic characteristics, and low cost [183]. On the other hand, the selection of the electrolyte salt generally depends on the electrode materials. Several neutral AGEs, such as PVA/LiCl [184], PVA/Na_2SO_4 [185], and PVA/$NaNO_3$ [186], have been investigated as promising electrolytes for FSSCs for different electrode materials. For instance, Li et al. [187] developed a neutral AGE with PVA as the polymer host, LiCl as the electrolyte, and water as the plasticizer for CNF-based films. The resultant symmetric device could be reversibly cycled in a wide voltage window of 1.8 V with a specific capacitance of 137.5 F/g at a scan rate of 5 mV/s. Moreover, ~93.1% capacitance retention was observed with almost constant Coulombic efficiency over 5000 cycles at 1 A/g, demonstrating an ideal movement of charge carriers and excellent electrochemical capacitive behavior. Subsequently, a practical demonstration was provided by fabricating internal series-connected SCs that afforded an extended voltage range up to 3.6 V. The Nyquist plot suggested that the equivalent series resistance (Rs) of the device was 3.35 Ω, illustrating the excellent effective interfacial area of the active materials for the electrolyte and the low internal resistance of the series-connected device. Thus, this neutral LiCl/PVA AGE effectively suppressed the chemical dissolution and irreversible electrochemical oxidation reaction of the electrode and mechanically stabilized the electrode during cycling. Similarly, PVA/LiCl AGE was recently used in a polypyrrole/carbon quantum dot (PPy/CQD) composite material synthesized on carbon cloth [188]. The device exhibited good capacitance (315 mF/cm^2) and good cycling stability (85.7% after 2000 cycles at 2 mA/cm^2). Other PVA-based neutral electrolytes such as PVA/$LiNO_3$ and PVA/LiOH have also been developed to enhance the intercalation/deintercalation performance of metal oxide and polymer electrodes [184, 189]. Notably, for some electrode materials such as vanadium oxide and vanadium nitride (VN), the

AGEs provided greatly enhanced cycling stability over aqueous electrolytes, suggesting the importance of interfacial contacts between the electrode and AGE electrolyte. In addition to PVA-based Li-ion AGEs. Lian et al. [190] have recently developed a polyacrylamide-LiCl (PAM/LiCl) AGE for CNT-coated graphite electrodes. The as-prepared PAM/LiCl AGE exhibited an amorphous structure with excellent ionic conductivity <10 mS/cm. Moreover, this neutral electrolyte system exhibited a high overpotential for both hydrogen and oxygen evolution reactions, providing a wide voltage window of 1.5 V for the CNT-graphite-based symmetric cell. The device also displayed excellent cycling stability with 90% capacitance retention over 10,000 cycles and excellent rate capability up to 5 V/s.

The relatively higher mobility of protons compared to that of Li^+ ions holds great promise to transport charges at ultrafast rates during charge/discharge processes in SCs. The proton conducting AGEs are prepared by mixing a polymer matrix with water (plasticizer) and proton-donor salts such as H_3PO_4 and H_2SO_4. To date, many proton-conducting AGEs, including PVA/H_3PO_4 [191] and PVA/H_2SO_4 [192], have been investigated. These AGEs exhibit ionic conductivities ranging from 10^{-4} to 10^{-2} S/cm at ambient temperature. Normally, proton conducting AGEs are applied to carbon-based materials such as graphene [193], CNTs [87], graphene ribbons [194], AC cloths [195], and graphene/porous carbon aerogels [196]. These advanced carbon nanostructures facilitate proton transport into the porous electrodes, suggesting enhancement in electrochemical performance and high utilization of the active materials. Recently, Chen et al. [197] tested different electrolytes (H_2SO_4, H_3PO_4, KOH, NaOH, KCl, and NaCl) with a PVA-based AGE for application to graphene-based FSCs. Electrochemical analyses suggested that the PVA/H_3PO_4 AGE exhibited a relatively higher capacitive performance. Lian et al. have developed a novel proton-conducting heteropoly acid AGE for high rate SCs [198, 199]. For example, the SiWA/PVA/H_3PO_4 AGE developed for a graphite-based device exhibited excellent performance and shelf life [198]. Compared to Nafion, the SiWA/PVA/H_3PO_4 gel electrolyte displayed significantly higher conductivity, achieving a

value of 8 mS/cm at room temperature. Moreover, the as-assembled device was successfully charged/discharged at a very high rate (20 V/s) with a time constant of 10 ms. To further improve the environmental stability of the SiWA/PVA/H_3PO_4 gel-electrolyte, nano-SiO_2 was incorporated into the AGE [200]. In gel electrolytes, SiO_2 can function as a plasticizer, cross-linker, and water-retaining agent [201]. The addition of SiO_2 in SiWA/PVA/H_3PO_4 significantly enhanced water retention and displayed consistent proton conductivity (16 mS/cm) over the parent gel electrolyte. It also exhibited a cross-linking effect on the PVA polymer. The symmetric cell was assembled from SS foils as electrodes and a nano-SiO_2-incorporated SiWA/PVA/H_3PO_4 AGE and demonstrated a high rate capability of 5,000 V/s in CV curves with good environmental stability and excellent cycle life (up to 100,000 cycles). Likewise, Lian et al. further developed another heterpoly acid AGE based on PVA and phosphotungstic acid ($H_3PW_{12}O_{40}$, PWA) and applied it to an asymmetric cell based on graphite and RuO_2 [202]. The PVA/PWA electrolyte provided a wide voltage window of 1.5 V and also contributed extra capacitance through the pseudocapacitance of the electrochemical reactions. Thus, the PVA-HPA electrolyte shows great promise for application in both symmetric and asymmetric FSCs due to its good ionic conductivity and stability. Recently, $H_5BW_{12}O_{40}$ (BWA)/PVA was developed as an effective electrolyte for FSSCs based on CNT-graphite electrodes and its electrochemical properties were compared to those of the SiWA/PVA electrolyte [203]. The structures of BWA and SiWA (Figure 10 (a)) suggest that except for the central atoms, the overall structures are the same. The electrolytes exhibited an ionic conductivity trend of BWA (78 mS/cm) >SiWA (60 mS/cm) >H_2SO_4 (30 mS/cm) as illustrated in Figure 10 (b). Due to the high ionic movements and number of dissociated ions, the device with the BWA/PVA electrolyte exhibited high capacitance. Moreover, this device was successfully cycled in a wide voltage window of 1.6 V (higher than that of the SiWA/PVA electrolyte, 1.4 V) while maintaining its high proton conductivity. It also displayed a very stable performance with no significant decay in capacitance after 5000 cycles (Figure 10 (c)). Several other polymer matrices have also been

investigated. Kim et al. [204] tested the electrochemical performance of RuO_2-based FSSCs using different acrylic hydrogel electrolytes such as poly(acrylic acid) (PAA), potassium polyacrylate (PAAK), and poly(2-acrylamido-2-methyl-1-propanesulfonic acid) (PAMPS). They discovered that the capacitance of RuO_2 decreased in the following trend: PAMPS/H_2O >PAA/H_2SO_4 >PAAK/H_2SO_4 >PAMPS/H_2SO_4. Moreover, due to the favorable proton hosting in the PAMPS side chain, RuO_2-based SCs with PAMPS exhibited a relatively high specific capacitance.

PVA-based electrolytes exhibit fluidity and thermal aging problems at high temperatures. Recently, Chen et al. [205] investigated the effect of temperature (between -5 °C and 55 °C) on the electrochemical performances of CNT-based FSCs with a PVA/H_2SO_4 gel-electrolyte. They observed that the conductivity of the gel electrolyte increased (from 5.52 mS/cm to 46 mS/cm) with an increase in temperature (Figure 10 (d)). Consequently, the capacitance was also enhanced with an increase in temperature due to the reduction in internal resistance via the acceleration of electrolyte ion transport/adsorption and surface modification of the electrode. About 24.3% and 32.6% enhancement was observed when the temperature changed from -5 °C to 25 °C and 25 °C to 55 °C, respectively, at 0.2 mA/cm^2. It was further concluded that the PVA-based gel electrolyte exhibited excellent cycling stability at low temperatures but was not suitable at temperatures >40 °C due to aging of the electrolyte (Figure 10 (e)). The digital photograph of the device at 55 °C displayed a color change in the PVA-H_2SO_4 gel electrolyte from transparent to brown, suggesting aging of the electrolyte as seen from Figure 10 (f). To limit the fluidity of the PVA-based gel electrolytes at high temperatures, Fei et al. [109] developed a cross linked PVA/H_2SO_4 hydrogel (SEM image in Figure 10 (g)). The PVA/H_2SO_4 membrane was modified by poly(vinyl pyrrolidone) (PVP) as a pore-forming agent to enhance their swelling ratio in the H_2SO_4 electrolyte; glutaraldehyde (GA) was employed as crosslinking agent. The ionic conductivity of the cross-linked PVA/H_2SO_4 electrolyte was determined as 24.9 mS/cm at 20 °C and further increased with an increase in temperature. The as-fabricated cell

with a graphene/CB nanocomposite electrode and cross-linked PVA/H_2SO_4 gel electrolyte exhibited good cycling stability with 78.3% capacitance retention after 1000 cycles at a high temperature of 70 °C (Figure 10 (h)). The photographs did not display any significant change in the color of cross-liked PVA/H_2SO_4 gel, while the bare PVA-H_2SO_4 turned brown suggesting aging at high temperatures (Figure 10 (i)).

With recent advancements in alkaline rechargeable batteries and SCs the development of alkaline gel polymer electrolytes is of great importance [206]. Among the different electrolyte salts, KOH is by far the most widely investigated salt for OH^- ion-conducting AGE application, due to its low-cost and environmentally friendly nature [207]. Several noteworthy investigations on KOH-based gel electrolytes for FSSCs have been reported [208]. For instance, Yang et al. have prepared a PVA/KOH gel electrolyte for SCs as well as Ni–MH and Zn–air batteries [209]. These alkaline PVA/KOH electrolytes exhibited a high ionic conductivity of 10^{-2} S/cm. Likewise, Zhang et al. [210] developed self-standing α-Fe_2O_3/rGO hybrid films by a vacuum filtration method and assembled symmetric FSSCs with a PVA/KOH gel-electrolyte. The device exhibited a high volumetric capacitance of 16.45 F/cm^3, leading to an energy density of 1.46 mWh/cm^3 and a power density of 199.8 mW/cm^3. In addition, the device with the AGE displayed excellent flexibility with almost no change in capacitance, even when the cell was bent to 180°. Similarly, Lewandowski et al. [211] developed a PEO/KOH gel electrolyte and reported good ionic conductivity ranging from 10^{-4} to 10^{-3} S/cm by controlling the PEO/KOH/ water ratio. To further improve the ionic conductivity of the PVA/KOH gel-electrolyte, additives or fillers such as SiO_2 [212] and GO [213] were incorporated. Thus, to improve ionic conduction, Huang et al. incorporated electrically insulating GO in a boron cross-linked PVA/KOH gel electrolyte for AC-based SCs. They discovered that at low levels of GO doping, the ionic conductivity of the cross-linked PVA/KOH gel increased (from 100 to 200 mS/cm), while high GO doping afforded a decreasing trend. This decrease in ionic conductivity with an increase in GO doping was attributed to ion channel blocking due to aggregation of the GO nanosheets. Interestingly, the

device with GO-doped boron cross-linked PVA/KOH exhibited 29% higher specific capacitance than that with the parent KOH aqueous electrolyte. Various reports with KOH as salt and different polymer matrices as host, such as poly(epichlorohydrin-co-ethylene oxide) P(ECH-co-EO)/KOH [214], PEO/KOH [215], and PAAK/KOH [216], have been investigated.

Despite significant advancements in KOH-based alkaline gel electrolytes, these compounds still exhibit KOH crystallization under ambient conditions, suggesting environmental instability. The performance of SCs with PVA/KOH gel electrolytes considerably degrades over time due to the hydration of the KOH/PVA electrolyte [217]. To tackle the issue of environmental instability, Li and Lian [218] replaced KOH with tetraethylammonium hydroxide. Moreover, OH^- ion transportation in the polymer matrix depends on the crystallinity, hydrophilicity, and functional group electronegativity of the polymer hosts. Thus, different polymer host matrices such as PVA, PEO, and PAA were tested to check their compatibility with TEAOH and achieve a gel electrolyte with high ionic conductivity TEAOH-PVA- and TEAOH-PAA-based SCs achieved an ionic conductivity of 5 mS/cm and an ultra-high rate of 5000 V/s that was attributed to the amorphous nature of TEAOH-PVA and TEAOH-PAA polymers with high water contents (12% and 46%, respectively). Moreover, no significant change in ionic conductivity was observed after 6 weeks of shelf-storage, suggesting excellent environmental stability.

4.2 Organic gel electrolytes (OGEs): GEs are promising candidates for FSSCs, however, their narrow operating voltage window limits their wide application. The focus has therefore shifted to OGEs. The synthetic strategy for OGEs plays an important role in determining the mechanical properties and ionic conductivity of the systems. Generally, an OGE comprises a physical blend of a high molecular weight polymer (PMMA, PVDF-HFP) gelated with a conducting salt dissolved in a non-aqueous solvent. Such OGEs overcome low interface formation and improve ionic conductivity. Organic solvents such as propylene carbonate (PC) [177], ethylene carbonate (EC), dimethyl formamide (DMF) [219], and their mixtures (PC-EC [220] and PC-EC-DMC [221]) have been used as common plasticizers to improve the working voltage range.

Thus, the cell voltage was increased to 2.5–3 V [222] a value that is significantly higher than that observed for AGE-based cells. This increase in cell voltage consequently improves the energy density of the device [223]. For example, Huang et al. [224] developed an OGE using a PEO-PAN blend (PAN-b-PEG-b-PAN) as host, DMF as plasticizer, and $LiClO_4$ as an electrolytic salt for an AC-based SC. The PAN-b-PEG-b-PAN/DMF/$LiClO_4$ OGE exhibited an ionic conductivity of 6.9 mS/cm and excellent compatibility with carbon electrodes. The fabricated cell exhibited a capacitance of 101 F/g at 0.125 A/g and delivered an energy level of 11.5 Wh/kg at a high power of 10 kW/kg over a voltage window of 2.1 V. Moreover, the cell displayed good stability with very small decay in capacitance over 30,000 cycles. The ionic conductivity is strongly influenced by the electrolyte salt and salt/host polymer ratio [225]. Thus, several different salts such as $LiClO_4$ [226], $LiPF_6$ [227], and $TBAPF_6$ [228] have been investigated in OGEs. For instance, Ramasamy et al. [229] investigated two different OGEs, namely PEO/PC-sodium bis(trifluoromethanesulfonyl)imide (NaTFSI) and PEO/PC-EC-DMC-NaTFSI, for use in AC-based SCs. Both gel electrolytes exhibited good ionic conductivity (0.54 mS/cm and 0.76 mS/cm, respectively), while the mixed gel electrolyte displayed higher ionic conductivity and thus, better electrochemical performances. Moreover, the cells operated in a wide voltage window of 2.5 V with high specific capacitance and good efficiency at a low charge rate (specific capacitance: 24 F/g, power: 0.52 kW/kg, and energy density: 18.7 Wh/kg). Other alkali metal ions such as Mg have been investigated in OGEs [230]. To improve the ionic conductivity, Jain et al. [231] incorporated SiO_2 particles into a PVDF-HFP/$Mg(ClO_4)_2$-PC electrolyte for carbon-based SCs. The resulting OGE exhibited an ionic conductivity of 5.4 mS/cm at room temperature as well as good mechanical and dimensional stability. Although these OGEs performed better than dry polymer electrolytes in terms of ionic conductivity, their mechanical stability was generally compromised. Therefore, considerable effort has been made to improve the mechanical stability of OGEs with particular interest in mimicking the liquid-like electrode-electrolyte interface [232]. An interesting new strategy to prepare high ionic conducting and

mechanically stable OGEs has recently been proposed in which a liquid electrolyte ($LiClO_4$/PC) is entrapped in a poly(2-hydroxy-3-phenoxypropyl acrylate) matrix via an in situ polymerization method [233]. Thus, this new OGE integrates the qualities of liquid, dry polymer, and quasi-solid electrolytes in a single system. Moreover, they entrapped ~80% (v/v) of the liquid electrolyte (3 M $LiClO_4$/PC) and presented an ionic conductivity of 4.7 mS/cm, comparable to those of non-aqueous liquid electrolytes. Large-scale FSSC cells (area 16 cm^2) with high AC and OGE mass-loading (4 mg/cm^2) were designed and demonstrated a capacitance of 111 F/g at a current density of 1 mA/cm^2 in a potential window of 2.5 V, indicating the industrial potential of the system.

4.3 Ionic-liquid based gel polymer electrolytes (ILGE): ionic liquid-based gel electrolytes exhibit some additional advantages over aqueous and organic electrolytes, including high ionic conductivities, non-volatility, non-flammability, and wide potential windows (up to 3.5 V); therefore, they are considered suitable for use in flexible and stretchable energy storage devices. Several ILGEs have been investigated for use in FSSCs [234], with the ILGE properties (conductivity and working voltage window) relying on the nature of the IL and polymer host matrix. Similar to AGE and OGE, various polymer hosts were investigated for ILGE, including PVDF-HFP [235], PVA [236], and PEO [237]. Recently, Tamilarasan et al. [238] prepared an ILGE using 1-butyl-3-methylimidazolium bis(trifluoromethylsulfonyl)imide as supporting electrolyte and PAN as polymer host (PAN/[BMIM][TFSI]). This electrolyte exhibited an ionic conductivity of 2.42 mS/cm at ambient temperature along with good mechanical strength and thermal stability. The graphene-based FSSC comprising the PAN/[BMIM][TFSI] ILGE displayed a maximum energy density of 32.3 Wh/kg and power density 82 kW/kg with good cycling stability. Zhang et al. [239] developed a flexible ILGE using 1-butyl-3-methylimidazolium chloride (BMIMCl) as ionic liquid, Li_2SO_4 as additive, and PVA as polymer host. The afforded ILGE presented a high ionic conductivity of 37 mS/cm and high fracture strain at 100% elongation. Moreover, the fabricated FSSC with AC as electrode and a PVA-

Li_2SO_4:BMIMCl gel electrode displayed a maximum energy density of 10.6 Wh/kg and a power density of 3400 W/kg. Notably, the ionic conductivity remained stable even after bending at an angle of 180°. To improve the conductivity of the gel-electrolyte, Yang et al. [240] made two major contributions by preparing GO-doped ILGEs such as P(VDF-HFP)) as the polymer matrix, the ionic liquid 1-ethyl-3-methylimidazolium tetrafluoroborate ($EMIMBF_4$) as the supporting electrolyte, and GO as the ionic conducting promoter. The ionic conductivity for 1 wt% GO-doped P(VDF-HFP)-$EMIMBF_4$ ILGE was determined as ~25 mS/cm, which was attributed to the 3D distribution of the GO network throughout the gel that acts as an ion ‘‘highway’’ to facilitate ionic transportation. Interestingly, the device based on the AC electrode and P(VDF-HFP)-$EMIMBF_4$ ILGE displayed an energy density of 32.4 Wh/kg at a power density of 6.6 kW/kg, suggesting excellent performance. For patterned MSCs, it is important to select a polymer that can be easily patterned on any substrate. Poly(ethylene glycol) diacrylate (PEGDA) is a nondegradable hydrophilic polymer that in an ILGE can be patterned on any substrate using a photolithographic process [241]. Kim et al. [242] developed an ILGE using 1-ethyl-3-methylimidazolium bis(trifluoromethylsulfonyl)imide ([EMIM][TFSI]) as IL electrolyte and PEGDA as polymer host. The afforded ILGE presented an ionic conductivity of 9.4 mS/cm at room temperature and demonstrated excellent electrochemical performances when used in CNT-based FSCs. The flexible MSC exhibited a stack capacitance of 5.3 F/cm^3 at a scan rate of 10 mV/s and an energy density of 2.9 mWh/cm^3 at a power density of 50 mW/cm^3 and a high potential window of 2 V. Moreover, the flexible MSC exhibited excellent cyclability with ~80% capacitance retention over 30,000 cycles. However, the preparation of an IL-gel-electrolyte with high ionic conductivity and good mechanical properties is still challenging. Zhong et al. [243] prepared a cross-linked [EMIM][TFSI] ionic liquid with PEO and benzophenone (Bp) followed by ultraviolet (UV) irradiation. The resultant [EMIM][TFSI]-based ILGE exhibited an ionic conductivity of 6.7 mS/cm with a high capacitance of 70.84 F/g, a wide and stable electrochemical window of 3.5 V, and an energy density of 30.13 Wh/kg.

An ideal IL-gel electrolyte should exhibit good compressive stress, good tensile strength, and puncture resistance. Liu et al. [244] developed an IL-mask hybrid gel electrolyte using $BMIMBF_4$ as ionic liquid, N,N-dimethylacrylamide (DMAA) and methylene-bis-acrylamide (MBAA) as polymer host, and TiO_2 nanoparticles. These nanoparticles initiated in-situ polymerization through UV irradiation to form a hybrid ILGE that comprised the high mechanical strength of the masked substance and the good thermal characteristics of the ILGE. The fabricated FSC exhibited a stable capacitive performance, even under a high pressure of 3236 kPa. Moreover, due to the good thermal stability of the composite gel electrolyte, the FSSC comprising an AC electrode could be operated at high temperatures ranging from 25 °C to 200 °C.

Many pseudocapacitive materials require proton CP gel electrolytes such as RuO_2, PANi, and PPy [245]. Recently, Lian et al. [246] developed protic ionic liquids (PILs) and binary systems of PILs with different cations and PIL eutectic compositions. Three PILs, namely 1-ethyl-3-methylimidazolium hydrogen sulfate ($EMIHSO_4$), 1-methylimidazolium hydrogen sulfate ($MIHSO_4$), and imidazolium hydrogen sulfate ($ImHSO_4$), were prepared. The ILGEs comprising $EMIHSO_4$-$MIHSO_4$ and $EMIHSO_4$-$ImHSO_4$ binary mixtures with a PEO polymer host exhibited ionic conductivities of 1.7 mS/cm and 2.5 mS/cm, respectively. Moreover, the eutectic binary PIL mixtures exhibited a liquidus range from −70 °C to +150 °C. The specific capacitances of the RuO_2-based cell using $MIHSO_4$-$ImHSO_4$, $EMIHSO_4$-$ImHSO_4$, and $EMIHSO_4$ were determined as 67 mF/cm^2, 44 mF/cm^2, and 26 mF/cm^2, respectively, suggesting a higher proton contribution of the MI and Im cations (over that of EMI) to the electrochemical oxidation and reduction of RuO_2. Similarly, Gao et al. [247], prepared a 1-ethyl-3-methylimidazolium bis(trifluoromethylsulfonyl)imide–poly(vinylidene fluoride)-hexafluoropropylene {[EMIM][NTf2]–PVdF(HFP)} ILGE and applied it to MnO_2/CNT/carbon nano-onions. The FSSCs exhibited an energy density of 16.4 Wh/kg at a power density of 33.3 kW/kg when the [EMIM][NTf2]–PVdF(HFP) gel electrolyte was employed. Moreover, these SCs exhibited high electrochemical

performances under large mechanical stress, making the devices suitable for application to flexible electronics.

4.4 Redox-active solid electrolytes: An emerging strategy to improve the electrochemical performance of a device is to modify/add redox-active species to the electrolyte to maximize the capacitance and consequently, the energy density of the device. Redox additives can add extra pseudocapacitance through reversible faradaic reactions and fast electron transfer at the electrode-electrolyte interface, resulting in significant enhancement of the specific capacitance. [248]. A typical charge storage mechanism in a redox-active electrolyte is presented in Figure 11 (a) using potassium iodide (KI) as an example. Notably, the iodide can produce redox pairs (I^-/I_3^- and I_2/IO_3^-) during the electrochemical process. The ionic sizes of I^-, I_3^- (I_3^- solvated by four water molecules), and IO_3^- (IO_3^- solvated by three water molecules) are 0.39 nm, 0.63 (1.8) nm, and 0.57 (1.4) nm, respectively [249]. Thus, due to their small ionic sizes, these ions can easily access the micropores and small mesopores of the porous electrode. A number of redox couples such as iodides (KI) [250, 183], $K_3Fe(CN)_6$ [251], and Na_2MoO_4 [252]; organic redox mediators such as hydroquinone [253], P-phenylenediamine (PPD) [254], and p-benzenediol [250]; and methylene blue (MB) [255], anthraquinone-2,7-disulfonate (AQDS) [256], and indigo carmine (IC) [257] have been investigated in solid-state gel electrolytes (Figure 11 (b-e)). This approach of adding redox-species in gel electrolytes effectively improves the performance of the device. Feng et al. [258] prepared a bromamine acid sodium (BAAS)-doped PVA-H_2SO_4 gel electrolyte that presented good ionic conductivity (21.4 mS/cm). The FSSC device assembled with AC electrodes displayed a good energy density (30 Wh/kg) for PVA-H_2SO_4-BAAM that was almost twofold higher than that without BAAM doping. The same group also investigated the redox additive 1-anthraquinone sulfonic acid sodium (AQQS) incorporated with a PVA-H_2SO_4 gel electrolyte [259]. The resultant redox-gel electrolyte exhibited excellent mechanical strength and a high ionic conductivity of 28.5 mS/cm. Notably, the device exhibited a remarkably stable capacitive performance with the gel electrolyte, even under a large tensile strain (100%), a high

pressure of 2000 kPa, and fold states. In our previous investigation, we demonstrated a double hybrid strategy using hybrid electrodes (rGO-POMs such as PMo_{12} and PW_{12}) and a hybrid electrolyte (HQ-doped PVA-H_2SO_4 gel electrolyte) [260]. The symmetric cells based on rGO-PMo_{12} and rGO-PW_{12} could be reversibly cycled in a wide voltage window of 1.6 V and exhibited energy densities of 1.7 mWh/cm^3 and 2.38 mWh/cm^3, respectively; these values are double those afforded in the absence of the HQ electrolyte. Yarn and fiber SCs have gained considerable attention for application in wearable applications. Pan et al. [261] assembled a CNT-mesoporous carbon (CNT-MC) fiber SC using a 2-mercaptopyridine (PySH)-doped PVA-H_2SO_4 gel-electrolyte. The resulting FSC, based on two aligned CNT-MC hybrid electrodes with a redox-gel electrolyte, exhibited excellent capacitances (length, areal, and volumetric capacitances of 17.51 mF/cm, 507.02 mF/cm^2, and 184.37 mF/cm^3, respectively) that were nine times higher than those afforded in the absence of PySH.

Kim et al. [262] utilized a p-nitroaniline-doped PVA-KOH (PVA-KOH-PNA) gel electrolyte in an asymmetric cell with SiC/Fe_3O_4 negative and SiC positive electrodes. Notably, the unique integration of hybrid electrode materials with a redox active gel electrolyte into a single device manifested several excellent features such as good specific capacitance (97.6 F/g at a scan rate of 5 mV/s) and good rate capability (72.58% retention after increasing the scan rate from 5 to 500 mV/s). Moreover, the cell could deliver an enhanced energy of 48.94 Wh/kg at a power density of 463.64 W/kg and excellent mechanical flexibility. Similarly, the specific capacitance of a fiber SC based on RGO exhibited a threefold improvement when sodium molybdate (Na_2MoO_4) was employed as a redox-active electrolyte [263]. The molybdate species (MoO_4^{2-}) form polymeric ions (H_2MoO_4) in an acidic medium (PVA/H_3PO_4 gel electrolyte) with a +VI oxidation state. H_2MoO_4 can react with H^+ ions via Mo(VI)/Mo(V) and Mo(VI)/Mo(IV) as possible redox couples.

To increase the operation cell voltage, Zhang et al. [264] investigated two redox mediators, namely ferrocene (fc) and 4-oxo-2,2,6,6-tetramethylpiperidinooxy (4-oxo-TEMPO)

with a tetraethylammonium tetrafluoroborate/PMMA-PC gel electrolyte for PEDOT-based SCs. The resultant gel exhibited ionic conductivities of 1.89 and 1.73 mS/cm, respectively, suggesting that the introduction of a redox mediator also improves the ionic conductivity of the gel-electrolyte. The maximum energies and power densities for fc- and 4-oxo TEMPO-based organic gel electrolytes were determined as 27.4 Wh/kg and 17.3 kW/kg and 20.8 Wh/kg and 14.8 kW/kg, respectively. Zhou et al. [265] developed a PEO/$LiClO_4$-acetonitrile organic gel with two different redox mediators, NaI/I_2 and $K_3Fe(CN)_6/K_4Fe(CN)_6$. The cells with NaI/I_2 and $K_3Fe(CN)_6/K_4Fe(CN)_6$ could deliver specific energy densities of 49.1 Wh/kg and 33.6 Wh/kg, respectively. Recently, Kim et al. fabricated flexible MSCs using an OGE with a redox-active species (HQ) based on PMMA-PC-$LiClO_4$ and MWCNTs on a PET substrate [266]. The incorporation of HQ significantly enhanced the specific capacitance and the energy density of the MSCs, with the latter being ~35-fold higher than that of MSCs without the HQ additive.

As described in the previous section, ILGEs are of special interest in the FSSC field due to their wide voltage window, inflammability, and good flexibility. Jang et al. [267] prepared a redox-active $EMIMBF_4$-IL-incorporated PVA-H_3PO_4 gel-electrolyte and investigated the ionic conductivity of the PVA/H_3PO_4/IL gel polymer electrolyte at various $EMIMBF_4$ weight percentages. They discovered that the ionic conductivity of the GE increased with an increase in $EMIMBF_4$ inclusion from 27.3 mS/cm (PVA/H_3PO_4) to a maximum of 39.3 mS/cm for 100 wt% $EMIMBF_4$ addition. The improved ionic conductivity was attributed to the plasticizing effect of the ionic liquid. The incorporation of $EMIMBF_4$ in the PVA/H_3PO_4 electrolyte effectively increased the specific capacitance of the AC-based FSC to 271 F/g at 0.5 A/g, a much higher value than that of the bare PVA/H_3PO_4 cell (103 F/g). Moreover, the FSC with the PVA/H_3PO_4/$EMIMBF_4$ (50%) electrolyte exhibited high energy and power density values of 54.3 Wh/kg and 23.88 kW/kg, respectively.

This section described the pros and cons of different GEs, namely aqueous, organic, ionic liquid, and redox-active species-based gel electrolytes. Different parameters such as ionic

conductivity, nature of electrolyte, and mechanical stability affected the overall electrochemical performance of the devices. Thus, to assemble high performance flexible SCs, suitable gel electrolytes with good ionic conductivity and mechanical stability must be used. Different combinations of polymer host matrices and electrolytic salts together with their corresponding ionic conductivities are summarized in Table 2 [176, 226, 230, 268-274]. This list can act as a guide for the selection of suitable gel electrolytes in FSCs.

5. Progress towards cell designs and an introduction to novel materials

Previous sections provide the comprehensive summary of the flexible substrates and flexible polymer gel electrolytes used in FSCs. The performance of FSCs devices is strongly depends on electrode materials and electrolytes. On the other hand, the device configuration is one of the factors defines the performance of FSCs devices. Thus, according to the arrangement of electrodes, FSCs can be classified into two categories such as solid-state symmetric SCs (SSCs) and solid-state asymmetric SCs (ASCs). Several materials such as nano-carbons (CNTs, graphene etc.), transition metal oxide/hydroxides/sulfides, conducting polymers have been widely investigated as a promising electrode materials for FSCs. Additionally, several new electrode materials such as MXenes, MOFs, POMs and black phosphorous (BP) are recently introduced as frontrunners in FSCs as shown in Figure 12. Following section provides the brief summary of the recent progress in these two configurations and strategies involved to improve the overall device performance with new designs and emerging new materials.

5.1. Advances in solid-state symmetric *(SSCs)* devices

5.1.1 Carbon-based SSCs

A symmetric device is fabricated from electrodes of the same material with the same mass. Carbon materials exhibit excellent properties including electrical conductivity, flexibility, low-cost, and light weight, which make them ideal candidates for SSC application. Several

works on SSCs based on carbon materials such as CNTs [37, 275] and graphene [40, 41, 44, 45] have been reported to date. Miao et al. [276] developed a flexible SSC based on freestanding nitrogen-doped porous CNFs derived from electrospun PAN/polyaniline core-shell composite nanofibers. The device achieved a specific capacitance of 260 F/g at a current density of 0.5 A/g (areal capacitance: 0.35 F/cm^2; volume capacitance: 4.3 F/cm^3) as well as a high rate capability with 54% capacitance retention of the initial capacitance at 8 A/g. Moreover, the device delivered an energy density of 9.2 Wh/kg (0.61 mWh/cm^3) at 0.25 kW/kg (17 mW/cm^3) and exhibited good cycling stability with 86% capacitance retention after 10,000 cycles. The flexibility test did not reveal any significant changes in the performance of device after repeated deformation (bindings). SWCNTs are considered the best candidates for SSCs due to their good electrical and mechanical properties as well as their good corrosion resistance. Yuksel et al. [228] cast SWCNT onto PDMS substrates to assemble transparent and flexible SSCs as illustrated in Figure 13 (a, b). Interestingly, the flexible SSCs exhibited an optical transmittance of 82% for 0.02 mg SWCNTs, while the high conductance of the SWCNT thin films eliminated the use of extra charge collectors. The specific capacitance, maximum power, and energy density were determined as 34.2 F/g, 21.1 kW/kg, and 18 Wh/kg, respectively, for 0.08-mg SWCNT devices (see Figure 13 (b)). Moreover, high bendability without any significant deterioration in device properties was attained (<6% loss in the initial capacitance over 500 charge/discharge cycles). Similarly, an interdigitated pattern of vertically aligned CNTs was coated on a thin PC substrate via a maskless laser-assisted dry transfer method [277]. The flexible SSC was fabricated with an ionogel, an ionic liquid in a semi-solid matrix gel electrolyte. The assembled SC device reached a maximum specific capacitance of 430 μF/cm at a scan rate of 0.1 V/s. Moreover, the flexibility test suggested a capacitance retention >90% over the full 1000 bending cycles, implying great potential for application in foldable energy storage devices. Paper-based substrates show greater promise as supports

than other polymer substrates such as PPET and PDMS due to their porous nature that readily integrates with carbon materials.

Graphene is another promising carbon isotope that has attracted much attention in the field of flexible SSCs due to its relatively higher mechanical and electrical properties and exceptionally larger surface areas when compared to other carbon materials. Recently, El-Kady et al. [278] developed a new strategy to fabricate graphene-based flexible SCs whereby the restacking of graphene was effectively avoided. The GO was directly reduced by using a standard LightScribe DVD optical drive. The afforded graphene films exhibited a high electrical conductivity (1738 S/m) and SSA (1520 m^2/g), allowing their direct use as SCs electrodes. The flexible SSC was assembled with PVA-H_3PO_4 as a gel electrolyte and displayed an ultrahigh energy density value while maintaining the high power density and excellent cycle stability of the SCs (>97% over 10,000 cycles). Moreover, the as-fabricated device exhibited an excellent calendar life since no significant decay in capacitance was observed after 4 months. In addition, the device exhibited only 5% loss in the initial capacitance when tested in the bent state for more than 1000 cycles. This was attributed to the high mechanical flexibility of the electrodes along with the interpenetrating network structure between the graphene electrodes and the gelled electrolyte. Likewise, an interconnected 3D graphene hydrogel with exceptional electrical conductivity (192 S/m) and mechanical robustness was developed by Xu et al. [279]. Initially, silver paste was coated on the PI substrate, onto which 3D graphene and a gel electrolyte were sequentially casted. The steps involved in the preparation of the electrodes and FSC are presented in Figure 13 (c). Exceptional electrochemical properties, including a high gravimetric specific capacitance of 186 F/g for a 120-μm thick electrode (up to 196 F/g for a 42-μm thick electrode) and an unprecedented areal specific capacitance of 372 mF/cm^2 (≤402 mF/cm^2 for a 185-μm thick electrode), were afforded. Moreover, no considerable change in the CV curves was observed, even under harsh bending conditions (Figure 13 (d)), suggesting excellent flexibility. Notably, only 8.4% decay in specific capacitance was observed after 10,000

charge/discharge cycles with a coulombic efficiency of 98.8–100% throughout testing under the bent state (150°) (Figure 13 (e)). Gao et al. [280] fabricated a flexible SSC based on a CNF-rGO hybrid aerogel with a PVA-H_2SO_4 gel electrolyte. The assembled SSC device displayed a specific capacitance of 203 F/g at a current density of 0.7 mA/cm^2 that was maintained at 134 F/g after an increase in current density to 11.2 mA/cm^2, suggesting excellent rate capability (66%). These characteristics were attributed to the highly open continuous pore structure that facilitates ionic diffusion. Moreover, the device exhibited excellent performance with an areal capacitance, maximum areal power, and areal energy density of 158 mF/cm^2, 15.5 mW/cm^2, and 20 mWh/cm^2, respectively.

5.1.2 Metal oxide/Nitride/Sulfide-based SSCs

Normally, carbon-based materials exhibit a lower capacitance than pseudocapacitive/faradaic materials due to their electrostatic (non-faradaic) charge storage mechanism. On the other hand, pseudocapacitive/faradaic materials store charge through fast and reversible surface redox reactions and hence, exhibit considerably large capacitance values (300–2000 F/g) [281]. This category normally comprises transition metal oxides/hydroxides/sulfides/nitrites [282] and CPs such as PANi, PPy, and PEDOT [283]. Among the different transition metal oxides, RuO_2 is the first and most studied material due to its wide potential window of 1.2 V, highly reversible redox reactions spanning three distinct oxidation states, high proton conductivity, remarkably high specific capacitance, and a long cycle life [49]. Ferris et al. [284] prepared a porous gold/RuO_2 electrode through a two-step procedure where the gold current collectors were sculptured using the hydrogen bubble dynamic template synthesis followed by electrodeposition of the hydrous ruthenium oxide. Figure 14 (a, b) illustrates the top side and cross-sectional SEM images of the electrodeposited RuO_2, suggesting a cracked mud-like morphology. Subsequently, a flexible SSC was assembled using gold/RuO_2 electrodes with a PVA-H_3PO_4 gel electrolyte comprising silicotungstic acid. A remarkable cell capacitance of 1220 mF/cm^2 with a very low IR-drop voltage (38 mV) was

afforded at 1.5 mA/cm^2. Moreover, the cell delivered an excellent specific energy density of 0.126 mWh/cm^2 (7.9 mWh/cm^3) and a maximum power density of 7.9 mW/cm^2 (493.8 mW/cm^3) (Figure 14 (c)) with a significant capacitance retention of ~95% after 2000 cycles. These encouraging electrochemical properties were attributed to the porous current collectors that provide a mechanical and conductive framework to afford durable 3D hydrous RuO_2. Similarly, the same group also fabricated vertically aligned carbon nanowalls decorated with porous ruthenium oxide for SSCs [285]. The RuO_2-decorated carbon nanowalls electrode, consisting of thin carbon sheets assembled from graphene domains, delivered a specific energy density of 49 μWh/cm^2, comparable to that of state-of-the-art lithium ion micro-batteries but with much higher power (10–20 mW/cm^2) and lifetime (up to 2000 cycles at 1.5 mA/cm^2) values (Figure 14 (d-f)). However, the high cost, toxic nature, use of acidic electrolytes, and lower natural abundance of RuO_2 hampers its potential for practical application. Thus, significant efforts have been directed towards finding suitable low-cost metal oxides as alternatives. Manganese-based oxides are widely recognized as highly promising alternative electrode materials for RuO_2 due to their low-cost and high theoretical specific capacitance (~1400 F/g). Due to the significant potential of MnO_2, several SSCs have been developed in recent years [105, 86]. Chodankar et al. [69] fabricated an SSC with MnO_2 nanoflakes grown on an SS substrate and a PVP-$LiClO_4$ gel electrolyte. Interestingly, the cell could be cycled in a wide voltage window of 1.6 V and hence, exhibited an energy density of 23 Wh/kg at a power density of 1.9 kW/kg. Recently, flexible SSCs were fabricated by electrodeposition of ultrathin MnO_2 nanosheets on commercial carbon fiber yarns [286]. Two hybrid MnO_2-coated carbon fiber electrodes were assembled together in parallel with a PVP-Na_2SO_4 gel electrolyte. The assembled flexible device exhibited a high volumetric energy density of 3.8 mWh/cm^3 at a power density of 89 mW/cm^3 with good flexibility, (no significant change in CV curves over 2000 cycles in the bending state). In addition, the device displayed superior long cycle stability with a capacity retention of 85.8% over 10000 cycles. A practical demonstration was also provided by lightning a commercial LED using the

integrated SCs, suggesting strong potential for application as flexible energy storage devices. However, the relatively low electrical conductivity of MnO_2 (10^{-5} to 10^{-6} S/cm) and its cycling stability limit its electrochemical performances. An effective approach to improve the electrical conductivity and stability of MnO_2 electrodes is to combine them with other highly conductive materials such as carbon-based materials and/or CPs. Shi et al. [287] decorated an amorphous MnO_2 nanoparticle on MWCNT fiber and applied it to SSC devices. This unique amorphous MnO_2@MWCNT fiber provided good mechanical reliability, high electrical conductivity, and fast-ion diffusion. Impressively, the volumetric capacitance for the amorphous MnO_2@MWCNT fiber-based device was determined as 10.9 F/cm^3 (specific length capacitance: 28.9 μF/cm; gravimetric capacitance: 10.3 F/g) at a current density of 0.1 A/cm^3. Notably, the device retained ~63% of its initial capacitance when the current density was increased from 0.1 A/cm^3 to 5 A/cm^3, suggesting excellent rate capability. In addition, the device could deliver an energy density of 1.5 mWh/cm^3 at a power density of 50 mW/cm^3. The flexibility test did not display any significant changes in the CV curves for the MnO_2@MWCNT fiber-based cell in a highly curved shape (180° folded). Moreover, very little decay (<10%) in the initial capacitance was observed over 15,000 charge-discharge cycles. Graphene can also be combined with MnO_2 to improve the overall electrochemical performance of the SSC cell. Ma et al. [288] developed hierarchical MnO_2 NW/graphene hybrid fibers with a mesoporous structure and large SSA (139.9 m^2/g) using the wet-spinning method. Synergic charge storage from both the pseudocapacitive MnO_2 and EDLC graphene improved the final device performance. The SSC cell fabricated by twisting two MnO_2/graphene fibers with a PVA-H_3PO_4 gel electrolyte exhibited a volumetric capacitance of 66.1 F/cm^3 (normalized by the total volume of the two fiber electrodes) and excellent cycling stability with 96% capacitance retention over 10,000 cycles. In addition, high energy (5.8 mWh/cm^3) and power (510 mW/cm^3) densities were also achieved, suggesting great potential for application in wearable electronics. Many other MnO_2-based hybrid devices were investigated for SSCs [289].

Due to their high specific capacitance, vanadium-based oxides are also considered as promising alternative materials to RuO_2 in flexible SSCs [290]. Kim et al. [291] fabricated an on-chip SSC on a PET substrate with hybrid electrodes of MWNT/V_2O_5 NW composites. The patterned SSC based on MWNT/V_2O_5 electrodes exhibited an excellent volumetric capacitance of 80 F/cm^3 with an energy density of 6.8 mWh/cm^3 in a PVA-LiCl electrolyte. The cell maintained 82% of the capacitance over 10,000 cycles at a current density of 11.6 A/cm^3. In addition, bending analysis suggested a small capacitance loss of only 6% over 1000 bending cycles at a bending radius of 7 mm. Finally, a practical demonstration was provided by operating a SnO_2 NW UV sensor.

Nickel- and cobalt-based binary and ternary materials have gained much attention as electrode materials for SSCs due to their high capacitance through faradaic reactions. Recently, Qian et al. prepared NiO nanosheets on flexible carbon fibers using pre-deposited ZnO nanoparticle films as a seed-layer that was subsequently removed [292]. The device displayed a specific capacitance of 20 mF/cm^2 at 0.1 mA/cm^2 that was maintained over 10000 cycles (100% retention), suggesting excellent cycling stability. The CV curves tested under different curvature conditions (bending angles: 60°, 90°, 120°, 180°, and twist) afforded very small changes to the CV curves, confirming outstanding mechanical flexibility. Ni-Co-based oxides ($NiCo_2O_4$) are low-cost ternary metal oxides with superior conductivity (from 0.05 to 10^{-6} S/cm) over that of single component nickel (2×10^{-2} S/cm) or cobalt oxides (333 S/cm), which makes them suitable for SCs. Recently, Wang et al. [75] designed flexible SSCs using two $NiCo_2O_4$ NWAs supported on Ni foam as the electrodes and PVA/KOH as electrolyte. The as-fabricated SSCs displayed a high cell areal capacitance of 161 mF/cm^2 at 1 mA/cm^2. In addition, good cycling stability (100% capacity retention) over 3000 cycles was achieved, even after the device was subjected to harsh mechanical conditions including both twisted and bent states. Likewise, Zheng et al. [293] assembled SSCs with a CNT/$NiCo_2O_4$ hybrid paper electrode and PVA/KOH gel electrolyte. A sandwich-like CNT/$NiCo_2O_4$ hybrid paper was prepared from a layer of conductive CNT

buckypaper coated with honeycomb-like $NiCo_2O_4$ nanosheets on both sides. This CNT/$NiCo_2O_4$ SSC device delivered a high areal capacitance of 337.3 mF/cm^2 (specific capacitance: 268.4 F/g) at a discharge current density of 0.1 mA/cm^2. An excellent volumetric energy of 1.17 mWh/cm^3 and a power density of 2430 mW/cm^3 were also demonstrated. On the other hand, a porous vanadium doped-zinc-nickel-cobalt ternary oxide (VZnNiCo) was grown on nickel foil for flexible SSCs [294]. Interestingly, the SSC based on VZnNiCo-based electrodes exhibited a capacitance of 590 mF/g, which is fourfold higher than that of $NiCo_2O_4$/$NiCo_2O_4$- and twofold higher than that of ZnNiCo//ZnNiCo-based SSCs. This significant increase in capacitive response was attributed to the synergistic redox reactions of all the ions and the direct growth of the unique porous nanostructure on the flexible current collector that provides excellent ion diffusion efficiency with a high electrochemically active surface area. Moreover, the device delivered a volumetric capacitance of 0.463 mF/cm^2 with an energy density of 0.93 mWh/cm^2 and a power density of 75 mW/cm^2. The SSC also revealed excellent cycling stability with 94% capacitance retention after 5000 cycles. The constant area under the CV curves at different bending angles suggests that mechanical deformation has no impact on the electrochemical activity of the flexible SC, thereby providing a stable capacitive response. Several other materials including $ZnCo_2O_4$ [97, 295], $MnFe_2O_4$/graphene [296], and CoMn-layered double hydroxide [138] have been investigated as promising electrode materials for SSCs.

Metal nitrides such as titanium nitride (TiN) and VN are an emerging class of electrode materials for high-performance SCs due to their excellent electrical conductivity (4000–55500 S/cm) [297]. Xiao et al. [298] prepared flexible freestanding mesoporous VNNWs on CNTs to realize MVNN/CNT hybrid electrodes. A synergic combination of the high electrochemical performance of MVNNs and the high conductivity and mechanical consolidation of the CNTs was achieved. The SSC cell was constructed based on freestanding MVNN/CNT hybrid electrodes with an H_3PO_4-PVA electrolyte and exhibited a high volume capacitance of 7.9 F/cm^3 and energy and power density values of 0.54 mWh/cm^3 and 0.4 W/cm^3, respectively, at a

current density of 0.025 A/cm^3. In addition, the device displayed 82% capacity retention over 10,000 cycles and demonstrated excellent flexibility with almost no change in the CV shapes under different bending conditions. Recently, Ma et al. [299] developed a freestanding multilayered film electrode with alternately stacked mesoporous Mo_2N nanobelts and rGO nanosheets (MMNNB/rGO). The SSC was then fabricated by sandwiching two thin and flexible freestanding MMNNB/rGO hybrid electrodes with PVA-H_3PO_4-silicotungstic acid (SiWA) gel electrolyte. The cell exhibited a high volumetric capacitance of 15.4 F/cm^3 as well as energy and power densities of 1.05 mWh/cm^3 and 0.035 W/cm^3, respectively, based on the volume of the entire cell. In addition, the flexible SC retained 85.7% of the initial capacitance after 4000 cycles, suggesting good cycling stability. However, most of these metal nitrites exhibited poor cycling stabilities due to the irreversible electrochemical oxidation of metal nitrites during the charging/discharging cycles. Lu et al. [300] demonstrated the electrochemical cycling stabilization of TiN NWs by using a PVA/KOH gel electrolyte. The polymer electrolyte suppressed the oxidation reaction on the electrode surface. As a result, the TiN NW-based SSCs displayed extraordinary stability up to 15000 cycles (82% capacity retention) and a high volumetric energy density of 0.05 mWh/cm^3. These results open up new opportunities in the development of high-performance metal nitrite-based SSCs. Similarly, many other metal sulfides [301] and metal phosphates [302] have been explored for their excellent potential as electrode materials for SSCs.

5.1.3 Conducting polymer-based SSCs

CPs such as PANi, PPy, and PEDOT are another class of pseudocapacitive materials with great potential to provide excellent specific capacitance [303]. Xiao et al. [304] designed a new rGO/PANi/rGO sandwich-structured nanohybrid paper and explored its potential as an electrode for SSCs. Initially, the free-standing graphene paper was prepared by a printing technique and bubbling delamination method and displayed high electrical conductivity (340 S/cm^2), light weight (1 mg/cm^2), and excellent mechanical properties. Subsequently, PANi was

electropolymerized on graphene paper with successive deposition of a thin graphene layer by dip coating to form a sandwich-structured graphene/PAni/graphene paper. Interestingly, this unique approach improved the energy storage capacity and enhanced the rate performance and cycling stability of the electrode. Thus, the as-obtained SSC exhibited an excellent capacitance of 120 mF/cm^2, which was maintained at 62% after an increase in current density from 0.1 to 10 mA/cm^2, and an energy density of 5.4 mWh/cm^3 (10.79 Wh/kg). PPy is another CP extensively used as an electrode material in SCs. This compound has good environmental stability, a low-cost synthetic procedure, good conductivity, unusual doping/dedoping chemistry, and high redox pseudocapacitive charge storage [54]. A simple “soak and polymerization” method was employed to prepare highly conductive paper through PPy coating on common printing paper [305]. The as-fabricated porous flexible paper exhibited an electrical conductivity of 15 S/cm and a low sheet resistance of 4.5 Ω/sq. The flexible SSC cell assembled from the PPy/paper composite exhibited an areal capacitance of 0.42 F/cm^2 with an energy density of 1 mWh/cm^3 at a power density of 0.27 W/cm^3 (normalized to the volume of the whole cell). The electrode for the SSC was prepared by decorating PPy NWs on rGO sheets [306]. The maximum capacitance for the PPy NW/graphene composite-based SSC was determined as 434.7 F/g at a current density of 1 A/g; this is almost quadruple that observed for the rGO-based SSC (117.2 F/g). Notably, a specific capacitance of 361.1 F/g (83%) was retained after an increase in current density to 20 A/g, suggesting excellent rate capability attributed to the high dispersibility, large effective surface area, and high electric conductivity (457.6 S/m) of the composite. In addition, the as-fabricated SSC exhibited an energy density of 60.37 Wh/kg at a power density of 0.5 kW/kg and excellent cycling stability with 88.1% capacitance retention over 5000 cycles, suggesting exceptional mechanical flexibility. Recently, Liu et al. [307] proposed a chemical polymerization and filtering method to coat flexible bacterial cellulose (BC) paper with PANi and graphene. BC paper with a 3D fibrous network exhibited an appreciable areal capacitance (4.16 F/cm^2), excellent tensile strength (65.4 MPa), and high flexibility. Moreover, the SSC cell

exhibited stable behavior in the bent state and provided an energy density of 0.12 mWh/cm^2 at a power density of 0.1 W/cm^2.

5.1.4 MXene-based SSCs

The revolutionary discovery of graphene realized the unusual electronic, mechanical, and optical properties of 2D materials, triggering extensive research in the past few years [308]. MXenes, the term collectively used for transition metal carbides, carbonitrides, and nitrides (Nb_2C, Ti_3C_2, Ti_3CN, Ti_4N_3, etc.) are the latest addition to the family of 2D materials and have received much attention since their discovery in 2011 [309]. These compounds have a general formula of $M_{n+1}X_nT_x$ (n = 1–3), where M represents an early transition metal (Ti, V, Nb, Cr, and Mo), X is carbon and/or nitrogen, and Tx corresponds to the surface terminations (hydroxyl, oxygen, and fluorine) [309, 310]. Their various unique properties, such as high conductivity, good mechanical properties, and hydrophilicity make them promising candidates for energy storage applications. For example, depending on its synthetic route, $Ti_3C_2T_x$ displays an electronic conductivity ranging from <1,000 S/cm to 6,500 S/cm [311].

MXenes are commonly prepared by selective etching of element “A” (mostly Al) from their layered precursors (MAX phases) using wet chemistry routes such as etching in HF [309, 312] or acidic solutions of fluoride salts (LiF in HCl) [313]. Among the many MXenes, $Ti_3C_2T_x$ is one of the most widely studied materials for FSSC application [314, 315]. Recently, transparent thin films of $Ti_3C_2T_x$ nanosheets with transmittance values of 93% (~4 nm) and 29% (~88 nm) and respective conductivities of ~5736 and ~9880 S/cm were fabricated [314]. Subsequently, a transparent solid-state asymmetric cell (72% transmittance) was assembled using $Ti_3C_2T_x$ and SWCNT films as positive and negative electrodes, respectively (Figure 15 a, b). Notably, the cell displayed a capacitance of 1.6 mF/cm^2 with a long cycle life (no capacitance decay over 20,000 cycles) (Figure 15 (c)). Moreover, almost fivefold improvement in the energy density was recorded when compared to the symmetric cell based on $Ti_3C_2T_x$. The exclusive layered structure of MXenes is thought to effectively prevent dense stacking in graphene and CPs,

resulting in relatively porous structures that are favorable for ion transport. In this context, an ultra-thin SSC (size of the whole device: 149 μm based on a PPy intercalated Ti_3C_2 film was assembled (Figure 15 d)). Notably, the intercalated Ti_3C_2 effectively prevented dense stacking in PPy and the electrochemical performances (Figure 15 e) including the capacitance (35 mF/cm^2), cycling stability, and deformation tolerance, were significantly advanced (Figure 15 f). [315]. Moreover, the strong interconnections between the PPy backbones and Ti_3C_2 layers offer highways for charge-carrier transport, greatly facilitating the pseudocapacitive process. Similarly, a freestanding film comprising hybrid inks based on $Ti_3C_2T_x$ nanosheets and graphene was developed and applied to the SSCs [316]. The assembled SSCs with the MXene/graphene hybrid film delivered a volumetric capacitance of 216 F/cm^3 at a current density of 0.1 A/cm^3. Moreover, the device exhibited a volumetric energy density of 3.4 mWh/cm^3 at a power density of 200 mW/cm^3, maintained at 1.4 mWh/cm^3 at a high power density of 1600 mW/cm^3. In this unique hybrid electrode, the small-sized MXene between the graphene layers acted as an active material and ideal “buffer” for enhanced electrolyte shuttling as well as a conducting spacer that prevented the irreversible π–π stacking between the graphene sheets.

5.1.5 Polyoxometalates (POM)-based SSCs

A new class of faradaic electrode materials known as POMs, is emerging as a molecular frontrunner in the field of energy storage systems [317]. POMs are nanometric oxide clusters with reversible redox activities that can be used as building blocks for energy storage applications. These materials comprise a 3D framework of redox-active molecular clusters that combine oxygen and early transition metals (Mo, V, Nb, Ta, and W) at their highest oxidation states. POMs are molecular oxides that contain tens to hundreds of metal atoms that reach nuclearities as high as 368 metal atoms in one single cluster molecule. Moreover, they are well-suited to achieve a high capacity for energy storage applications due to their fast and reversible multi-electron redox reactions [318]. Nonetheless, the best known, most stable, and widely

investigated species are solid acids (or anions in their deprotonated form) with the general formula $H_n[AM_{12}O_{40}]$ (A: Si or P and M: V, Mo, or W). Notably, POM clusters (simple Keggin type), phosphomolybdate (PMo_{12}), and phosphotungstate (PW_{12}) represent the ultimate degree of dispersion for an oxide nanocluster as all 12 MO_6 moieties (M: Mo or W) are at the surface of the cluster; this makes them ideal active materials for SCs [319]. Indeed, the development of hybrid materials made of CPs and POMs for SSCs has been tackled by our group [317, 320] and others [319, 321]. The anchoring of anionic POMs within the network of CPs and/or on the surface of nanocarbons (graphene and CNTs) has led to the synthesis of hybrid materials in which the inorganic clusters maintain their integrity and activity while benefiting from the conducting properties of the hybrid composite structure. A ternary nanocomposite based on polypyrrole- Phosphomolybdic acid/reduced graphene oxide (PPy-PMo_{12}/rGO) was developed for the realization of a high-performance SSC [322]. The flexible cell assembled on an Au-coated PET and a PVA/H_2SO_4 electrolyte (Figure 15 (g)) displayed a specific capacitance of 2.61 mF/cm^2 at a current density of 150 mA/m^2. An ion soft landing (SL) deposition technique has been recently developed to prepare high-density CNTs decorated with monodisperse POM (PMo_{12}) anions and the agglomeration of the active species (POMs) has been proven to strongly affect the performance and stability of SSCs [323]. The direct evidence of the uniform distribution of the individual redox-active species (PMo_{12}) on complex commercially relevant electrodes (CNT) was provided using atomically resolved STEM imaging. The FSC device was fabricated from CNT/PMo_{12}-coated carbon paper as electrode and $EMIMBF_4$/PVDF-HFP as gel-electrolyte. Uniform deposition of small amounts of intact active species (PMo_{12}) on CNT electrodes was found to substantially improve the device performance.

5.1.6 *MOF-derived material-based SSCs*

MOFs, a new class of functional materials with high porosity and chemical tunability, comprise nanosized cavities and open channels that make them promising candidates as sacrificial templates or precursors of nanostructured materials [324]. MOFs were first introduced

by Yaghi [325] in 1995, as extremely light materials with very high SSAs (up to 46000 m^2/g), large pore volumes, and well-defined pore sizes. MOFs consist of metal ions or cluster units coordinated by electron donating organic ligands, which are commonly prepared using solvothermal, hydrothermal, microwave-assisted, and surfactant mediated synthetic methods [324]. The mass production of MOFs was recently realized by some companies (BASF and MOF Technologies) [326]. MOFs hold great promise as electrode materials in SCs due to their controlled pore sizes (0.6–2 nm) as well as their ability to incorporate redox-metal centers.

As-synthesized MOFs are usually non-conducting, thereby limiting their practical application in SCs. Hence, high temperature carbonization methods are implemented to convert them into nanoporous carbon materials. The first practical realization of MOFs as an electrode in SCs was demonstrated in 2011, using some Co-based MOFs in liquid electrolytes [327]. Recently, they have been employed as promising electrode materials in FSSCs [328-331]. The FSSC with MOF-5-derived nanoporous carbon delivered a high energy density of 17.37 Wh/kg and high power density of 13 kW/kg with 94.8% capacity retention over 10,000 cycles using Na_2SO_4/PVA electrolyte [329]. Another effective strategy to improve the conductivity in MOFs is to prepare nanocomposites with other conducting materials such as carbon-based species (CNT, RGO) and CPs (PANi, PPy) [330]. For example, Co-based MOF crystals (ZIF-67) were interwoven with electrochemically deposited PANi chains on carbon cloth to realize a flexible conductive porous electrode without altering the underlying structure of the MOF (Figure 15 h, i) [331]. The SSC with the PAni-ZIF-67-CC electrode yielded a remarkable areal capacitance of 35 mF/cm^2 (stack capacitance: 116 mF/cm^3) and a power density of 0.833 W/cm^3 at a current density of 0.05 mA/cm^2 and retained more than 80% of its initial capacitance after 2000 cycles. As previously mentioned, MOFs are ideal templates for the construction of carbons, metal nanoparticles, metal oxide nanoparticles, and their composites under thermolysis conditions. The tribasic composite MoO_2@Cu@C was prepared using the POM (PMo_{12})@MOF (Cu-based MOF) as template by a thermolysis method and subsequently applied to SSCs [332]. The

device displayed a charge capacity of 7.49 mAh/g at 0.25 A/g and 91% capacity retention over 5000 cycles. Moreover, the cell delivered an energy density of 2.58 Wh/kg at a power density of 86.8 W/kg. Recently, rGO/Fe_2O_3 and rGO/NiO/Ni composite aerogels were also prepared using GO/MOF composites (Fe-MOF and Ni-MOF, respectively) as precursors. [156]. The flexible SSC device assembled with the rGO/Fe_2O_3 composite aerogel exhibited a volumetric capacitance of 250 mF/cm^3 at 6.4 mA/cm^3 and a capacity retention of 96.3% after 5000 cycles at 50.4 mA/cm^3. It also displayed excellent mechanical flexibility.

In addition to producing nanocomposites, several efforts have been made to design and prepare conducting MOFs [333]. In 2016, Dinca et al. [334] applied the conductive MOF Ni_3(2,3,6,7,10,11-hexaiminotriphenylene)$_2$ (Ni_3(HITP)$_2$) as free-standing electrode material in an EDLC without conductive additives or other binders. This was the first of its kind. Moreover, the team claimed a bulk electrical conductivity >5,000 S/m, exceeding that of ACs and holey graphite (1,000 S/m). Inspired by this pioneering work, Li et al. have recently developed conductive MOF NWAs (Cu-CAT) on carbon fiber paper and demonstrated their potential as electrodes in SSCs. Typically, Cu-CAT is constructed by coordinating Cu ions with 2,3,6,7,10,11-hexahydroxytriphenylene (HHTP) ligands in the *ab* plane to create a 2D hexagonal lattice [335]. This structure further packs along the *c*-axis with a slipped-parallel AB stacking model to form a honeycomb-like porous structure as illustrated in Figure 12. Moreover, Cu-CAT exhibited 1D channels along the *c*-axis with an open-window size of ≈1.8 nm and good charge transportation due to the effective orbital overlap between the Cu ions and organic ligands. The Cu-CAT NW-based SSC displayed an EDL capacitance of 120 F/g at a current density of 0.5 A/g and good cycling stability, retaining 85% of its initial capacitance after 5000 cycles. Notably, the device delivered a surface area normalized capacitance of ≈22 μF/cm^2 (BET surface area: 540 m^2/g), which is twofold higher than values observed for AC- and SWCNT-based cells (10 μF/cm^2) and comparable to those observed for graphene-based SSCs (18.9 –25 μF/cm^2).

5.1.7 Black Phosphorous-based *SSCs*

BP is a new member of the large family of 2D materials and is the most stable allotrope of phosphorous. It comprises a layered structure with corrugated planes of P atom puckered layers weakly bonded via van der Waals interactions [336]. Similar to other layered materials, single- and few-layered BP nanoflakes can be readily formed by mechanical exfoliation (high-energy ball-milling of red phosphorus and liquid exfoliation [337]. Few-layered BP (phosphorene) is a p-type direct-bandgap semiconducting layered material. Moreover, BP has a large spacing of 5.3 Å between adjacent puckered layers that is larger than the 3.6-Å spacing observed in graphite and comparable to the 6.15-Å spacing in the 1T MoS_2 phase. This makes it a promising candidate for energy-storage applications [338]. The utilization of BP in SCs is still in its infancy. Recently, a liquid-exfoliated BP nanoflake-based SSC on a PET substrate was accomplished using PVA/H_3PO_4 as gel electrolyte [338]. The cell displayed a volumetric capacitance of 17.78 F/cm^3 (59.3 F/g) at a scan rate of 5 mV/s with energy densities ranging from 0.123 to 2.47 mWh/cm^3 and a maximum power density of 8.83 W/cm^3. The cycling stability study revealed ~71.8% capacitive retention after 30,000 cycles.

5.1.8 Other emerging materials

In addition to traditional electrode materials, a few works on FSSCs with selenium (Se)- and tellurium (Te)-based transition metal dichalcogenides have been recently reported [339-340]. These materials are considered as promising electrode materials for FSSCs due to their large effective surface area, remarkable electrochemical performance, and good flexibility, guaranteeing maximum functionality. Very recently, atomically thin WTe_2 nanosheets were applied to SSCs for the first time [341]. WTe_2 was initially prepared using the CVD method followed by liquid-phase exfoliation to afford single crystals 2-7 layers WTe_2 nanosheets. The resulting SSCs delivered energy and power densities of 0.01 Wh/cm^3 and 83.6 W/cm^3, respectively, values superior to those observed for the commercial 4 V/500 μAh Li thin-film battery and 3 V/300 μAh electrolytic capacitor. These positive results were attributed to good

mechanical flexibility and superior cycling stability (capacitance retention of ≈91% after 5500 cycles). Table 3 lists recent advancements in symmetric SCs based on different materials with their corresponding electrochemical performances [191, 342-376].

5.2. Advances in solid-state asymmetric SCs

SSCs usually exhibit low voltage (~1 V), leading to low energy density. Thus, to expand the practical applications of SCs, the energy density and operating voltage of FSSCs need to be improved without sacrificing their device power density and cycling stability. An emerging approach to attain these results is to assemble ASCs [377]. Contrary to SSCs, ASCs comprise two electrodes of different charge storage mechanisms such as a faradaic/pseudocapacitive positive electrode and a non-faradaic capacitor-type negative electrode [378]. Thus, in ASCs, both electrodes work in different potential windows, resulting in an extended voltage range up to 2.0 V for the cell, even in aqueous electrolytes. This range is much larger than that of SSCs and hence, significantly improves the energy density. Several innovative cell designs are developed in these years as shown in Figure 16, in order to use in wearable/bendable electronics

5.2.1 Carbon-based negative electrodes

Generally, carbon-based nanomaterials are used as negative electrodes in ASCs due to their excellent electrical conductivity and high surface area and power density [379]. On the other hand, faradaic/pseudocapacitve materials such as transition metal oxides and CPs are used as positive electrodes due to their high capacitance and energy density [380]. AC has been widely studied as a negative electrode material in ASC due to its high SSA (2000 to 3000 m^2/g) and controlled porosity. Recently, Pang et al. [381] fabricated ASCs with a Co_3O_4-nanocube/$Co(OH)_2$-nanosheet hybrid as a positive electrode and AC as a negative electrode with PVA/KOH as gel electrolyte. The $Co_3O_4/Co(OH)_2$//AC device delivered a specific capacitance of 210 mF/cm at a current density of 0.3 mA/cm^2, which is almost twice as high as that of Co_3O_4-nanocube//AC (111 mF/cm^2), fivefold higher than that of $Co(OH)_2$ microplate//AC

(43 mF/cm^2), and twice as high as that of Co_3O_4+$Co(OH)_2$ hybrid//AC (133 mF/cm^2) cells. Interestingly, the Co_3O_4/$Co(OH)_2$ hybrid//AC cell maintained a capacitance of 159 mF/cm^2 at a current density of 10 mA/cm^2, suggesting excellent rate capability (75% capacitance retention). Notably, the as-assembled ASC cell exhibited a maximum energy density of 9.4 mWh/cm^3 with very little capacitance decay over 5000 cycles (97.4% retention). Graphene is another carbon-based negative electrode material widely investigated for application in ASCs due to its high electrical conductivity and mechanical strength [382]. Pan et al. [383] developed ASCs by pairing MnOx (as a positive electrode) with chemically converted graphene as a negative electrode. A nanoporous Ni architecture was first constructed on the surface of a flexible carbon cloth (Ni@CC) to prepare a 3D porous current collector. This unique 3D architecture effectively enhanced the energy density per surface area due to its ability of high mass loading of active materials and efficient electron and ion transport. Subsequently, ultrathin MnO_x nanosheets were electrodeposited onto the 3D Ni@CC nanoporous current collectors, which exhibited an areal specific capacitance of 906.6 mF/cm^2 at 1 mA/cm^2 in an aqueous electrolyte. When 3D MnO_x@Ni@CC was employed as the positive electrode and chemically converted graphene (CCG) as the negative electrode in an ASC, with Na_2SO_4/PVA as gel electrolyte, a superior energy density of 1.16 mWh/cm^3 was achieved. In addition, the device exhibited excellent cyclic stability with 81.5% capacity retention after 10,000 charge/discharge cycles. More importantly, the ASC cell maintained over 85.7% of its original capacitance, even after 200 bending cycles, suggesting potential application in flexible high performance wearable electronics and energy storage devices. A novel 1D $Co_{2.18}Ni_{0.82}Si_2O_5(OH)_4$ ultrathin nanoflake architecture was paired with GNSs to realize an ASC [384]. Interestingly, the as-assembled $Co_{2.18}Ni_{0.82}Si_2O_5(OH)_4$//graphene ASC cell displayed a specific capacitance of 194.3 mF/cm^2 at a current density of 0.50 mA/cm^2, while retaining a value of 141.6 mF/cm^2 at a current density of 6.0 mA/cm^2 (~73% capacitance retention). In addition, the cell could deliver a maximum energy density of 0.496 mWh/cm^3 and excellent cycle stability with 96.3% retention over 10,000 cycles.

Hierarchical core/shell nanostructures are of great interest due to their large surface area, short diffusion paths, fast-ion/electron transport pathway, and component synergistic effects that are feasible for high performance SCs. Zhu et al. [385] prepared well-aligned hierarchical $Cu(OH)_2$@$Ni_2(OH)_2CO_3$ core/shell NWAs on copper foam as a positive electrode combined with rGO as negative electrode to assemble ASCs. Impressively, the device could be cycled up to 1.6 V and exhibited a specific capacitance of 785 mF/cm^2 (based on the area of the device) at a current density of 10 mA/cm^2. Moreover, an energy density of 1.01 Wh/cm^2 at a power density of 57 W/cm^2 was attained. A practical demonstration was provided by powering a "five-point star" pattern on a shoulder bag using two of the fabricated asymmetric SC devices with an area of 1 x 3 cm^2 in series for more than 45 s, indicating great potential for application as a portable and wearable energy storage device.

The common electrochemical performance-limiting factor for metal oxides is their low electrical conductivity, hence, it is essential to combine them with conducting carbon or polymer-based materials. Recently, a $ZnCo_2O_4$/ZnO@multiwall carbon nanotube hybrid was prepared as a positive electrode for ASCs [386]. Initially, $ZnCo_2O_4$/ZnO was deposited onto Ni foam by the hydrothermal method, with subsequent MWCNT deposition by a dip and dry process. The ASC cell was then fabricated by pairing a $ZnCo_2O_4$/ZnO@MWCNT positive electrode and AC negative electrode with PVA/KOH as electrolyte. The ASC device displayed a high specific capacitance of 111.8 F/g (at 1 A/g), a high energy density of 48.1 Wh/kg (at 900 W/kg), and good cycling stability with a capacitance retention of 92.9% after 3000 cycles. Moreover, two serial connected $ZnCo_2O_4$/ZnO@MWCNT//AC ASCs were utilized to light four parallel connected LEDs, which remained bright for 23 min. Similarly, Shao et al. [387] produced a solid-state ASC device based on a graphene/MnO_2 nanorod as the positive electrode and a graphene/Ag combination as the negative electrode. The device exhibited a maximum energy density of 50.8 Wh/kg and a high power density of 90.3 kW/kg, even at an energy density of 7.53 Wh/kg. The bent hybrid nanostructured asymmetric SC was connected to spin a fan, which

also proved the high power density of the fabricated asymmetric SC. Notably, the unique graphene sheet-MnO_2 nanorod structure and 3D network architecture of the graphene/Ag species provided a higher specific surface and richer porous structure than those of traditional constructions, enabling high rates of charge propagation and short electron transport paths that improved the electrochemical performances of the electrodes. Yang et al. [388] also developed ASCs based on a 3D Al@Ni@MnOx nanospike (NSP) as the positive electrode, chemically converted graphene (CCG) as the negative electrode, and Na_2SO_4/PVA as the polymer gel electrolyte. Due to the different working potential windows of the Al@Ni@MnOx NSP and CCG electrodes, the ASC cell exhibited ideal capacitive behavior with a cell voltage up to 1.8 V, capable of lighting up a red LED indicator (nominal voltage: 1.8 V). Moreover, the device delivered an energy density of 23.02 Wh/kg (1.29 mWh/cm^3) at a power density of 947.5 W/kg (53.02 mW/cm^3); the device maintained an energy density of 6.57 Wh/kg even at a maximum power density of 59 kW/kg. Interestingly, the device preserved 96.3% of its initial capacitance over 10,000 charging/discharging cycles at a current density of 2 A/g. Several other ASCs with carbon-based negative electrodes have also been explored [389].

CPs are also promising candidates to combine with metal oxides to increase conductivity and add extra pseudocapacitance. Recently, a positive electrode for ASCs was fabricated by coating $NiCo_2O_4$ NWAs on carbon textiles with a PPy nanosphere shell layer [390]. The $NiCo_2O_4$@PPy electrode exhibited a high specific capacitance of 2244 F/g in an aqueous electrolyte. This was attributed to the synergistic effect between the conductive PPy and short ion transport channels in the ordered $NiCo_2O_4$ mesoporous NW. Moreover, a lightweight and flexible ASC device assembled with $NiCo_2O_4$@PPy (positive) and AC (negative) electrodes achieved a high energy density of 58.8 Wh/kg at 365 W/kg, outstanding power density of 10.2 kW/kg at 28.4 Wh/kg, and good cycling stability (□89.2% retention after 5000 cycles) as well as high flexibility. Similarly, ASC was fabricated from PPy-wrapped MnO_2 nanoflowers on carbon cloth and AC on carbon cloth as positive and negative electrodes, respectively [391]. The ASC

displayed an areal capacitance of 1.41 F/cm^2 and an energy density of 0.63 mWh/cm^2 at a power density of 0.9 mW/cm^2. An energy storage unit fabricated using multiple ASCs could drive an LED segment display, a mini motor, and even a toy car after full charging. PEDOT is another promising CP that can be used as a pseudocapacitive material in combination with a metal oxide. Yang et al. [392], developed a fiber-shaped ASC with NiO/Ni(OH)$_2$ nanoflowers encapsulated in 3D interconnected PEDOT on contra wires as the positive electrode and ordered mesoporous carbon (CMK3) as the negative electrode. The as-formed flexible ASC device exhibited an areal capacitance of 31.6 mF/cm^2 (3.16 F/cm^3) at a current density of 0.4 mA/cm^2 with an energy density of 0.011 mWh/cm^2 at a power density of 0.33 mW/cm^2 in an operating voltage window of 1.45 V. The as-fabricated ASC only displayed a slight fluctuation during charge/discharge cycling over 1400 cycles, demonstrating the outstanding stability of the device.

As described in the previous section, MOF-based materials can be used as templates or precursors for the synthesis of nanoporous carbon and nanostructured metal oxides with tunable surface properties. A new “one for two” strategy has been proposed to prepare positive (Co_3O_4) and negative (N-doped carbon) electrodes on carbon cloth for flexible ASCs using a single 2D MOF precursor [393]. The device exhibited fast kinetics by retaining almost 66% capacitance when the current density was increased eightfold and also demonstrated robust mechanical flexibility. Moreover, an energy density of 41.5 Wh/kg at a power density of 6.2 kW/kg was delivered with 85.5% capacitance retention after 20,000 cycles under different bending and twisting conditions.

5.2.2 Metal oxide-based negative electrodes

Recently, metal oxides have also been widely explored as negative electrodes in asymmetric supercapacitors due to their high capacitance and high energy density over those of carbon-based materials [394]. The working potential window of metal oxides for asymmetric SCs can be defined as:

$$E = E_0 + \Delta E_1 + \Delta E_2 = \frac{1}{F(\omega^{\beta} - \omega^{\alpha})N_A} + \Delta E_1 + \Delta E_2 \qquad (1)$$

where ω^{α} and ω^{β} are the work functions of the positive and negative electrodes, respectively; N_A is Avogadro's constant; and ΔE_1 and ΔE_2 are the surface dipole potential of the positive and negative electrodes, respectively [395]. For SSCs, both electrodes have the same charge storage mechanisms so that $\Delta E_1 = -\Delta E_2$ and $\omega^{\beta} = \omega^{\alpha}$. Hence, the additional potential window is zero. The operation voltage of symmetric SCs is therefore defined by the dissociation energy of the electrolyte. Conversely, for asymmetric SCs, the work function difference of the two metal oxides (positive and negative electrodes) defines the operating potential. Therefore, to assemble large voltage asymmetric SCs, it is essential to choose the two different metal oxide electrodes with the largest work function difference. This results in an extended operating voltage window, even larger than the dissociation energy of the electrolyte, which improves the energy density over that of symmetric SCs. Water dissociation is kinetically limited by hydrogen and oxygen evolution reactions on the surface of the metal oxides in the aqueous electrolytes.

Figure 17 presents the work functions and working potential windows for different metal oxides [396, 397] and can be used as a guide when choosing suitable positive and negative electrodes for high performance ASCs. In metal oxides with a higher work function, oxygen vacancy defects are more prone to decrease the work function of the oxide because they act as n-type dopants, shifting the Fermi level closer to the conduction band edge. Furthermore, the chemisorption of proton and hydroxide ions on the surface of the metal oxides will further extend the potential window by modifying the work function of the electrode. Several metal oxides, such as MoO_3 [397] and iron oxide [398], have been widely studied as negative electrodes for ASCs due to advantages including high theoretical capacitance, a suitable potential window, low cost, abundance, and nontoxicity. Yang et al. [399] developed a low-cost high-performance ASC with α-MnO_2 NWs and amorphous Fe_2O_3 nanotubes on flexible carbon fabric with PVA-LiCl as the gel electrolyte. Taking advantage of the different operating potential ranges of MnO_2 NWs and

Fe_2O_3 nanotubes, the ASC cell can be cycled up to 1.6 V. The MnO_2//Fe_2O_3 ASC cell exhibited high specific and volumetric capacitances of 91.3 F/g and 1.5 F/cm^3, respectively, at a current density of 2 mA/cm^2 that was maintained at 0.88 F/cm^3 when the current density was increased to 10 mA/cm^2, suggesting good rate performance (58.6% retention). Moreover, the MnO_2//Fe_2O_3 cell displayed a high energy density of 0.55 mWh/cm^3, and a high power density of 139.1 mW/cm^3 with moderate stability (80%) over 6000 cycles. A simple application to light a commercial blue LED was demonstrated by connecting two MnO_2//Fe_2O_3 devices in series. These encouraging results were attributed to the unique nanostructure of the carbon fabric with a large surface area and high electrical conductivity. Recently, Ma et al. [400] designed $ZnCo_2O_4$@MnO_2 core-shell nanotube arrays on Ni foam as a positive electrode for an ASC and paired it with 3D porous α-Fe_2O_3 on Fe foil as the negative electrode. The as-designed ASC device exhibited an extended operating voltage window of 1.3 V with a specific capacitance of 161 F/g at 2.5 mA/cm^2, a maximum energy density of 37.8 Wh/kg, and excellent stability with 91% capacitance retention after 5000 cycles. Likewise, a novel core-shell nanoarchitecture based on Co_3O_4@RuO_2 nanosheet arrays was developed on woven carbon fabrics to use as negative electrodes in ASCs [401]. The positive electrode Co_9S_8 nanorod array was prepared by hydrothermal sulfuration treatment of acicular Co_3O_4 nanorod arrays. Thus, the Co_3O_4@RuO_2//Co_9S_8 ASC cell was fabricated with a PVA-KOH gel electrolyte that can be reversibly cycled in a voltage window up to 1.6 V. The as-fabricated cell exhibited an energy density of 1.21 mWh/cm^3 at a power density of 13.29 W/cm^3 in aqueous electrolyte and an energy density of 1.44 mWh/cm^3 at a power density of 0.89 W/cm^3 in a solid-state electrolyte. However, the intrinsic semiconducting nature of metal oxides presents poor electrical conductivity, eventually leading to low power density in ASCs [402]. To tackle this issue, Yu et al. [403] recently developed a novel coil-type ACS based on Fe_2O_3@C nanorods on carbon cloth as the negative electrode and MnO_2 NWs on copper wire as the positive electrode with PVA-LiCl as the gel-electrolyte. The thin carbon coating on the Fe_2O_3 nanorods improved the

electrical conductivity. For the MnO_2 NW positive electrode, the copper wire was first annealed to prepare insulating CuO NWs on the Cu-wire and subsequently, a MnO_2 layer was electrodeposited onto it. The coil-type ASC was assembled by simply winding the Fe_2O_3@C negative electrode onto the MnO_2@CuO NW positive electrode separated by a PVA-LiCl electrolyte. The as-assembled device exhibited an excellent volumetric capacitance of 2.46 F/cm^3 with extraordinary rate capability (95.4%), high energy density (0.85 mWh/cm^3) (Figure 18 (a)), and remarkable flexibility and bendability with superior bending cycle stability (≈93.0% after 4000 cycles at different bending states). The digital photographs of the different bending states of the device and the corresponding capacity retention against the number of cycles are illustrated in Figure 18 (b, c), respectively. Another approach to improve the conductivity of metal oxide electrodes is to combine them with carbon materials such as CNTs and graphene. Thus, ASCs with wrinkled MnO_2/CNT as the positive electrode and a wrinkled Fe_2O_3/CNT composite as the negative electrode were assembled [404]. The optimized ASC could be reversibly cycled in a voltage window up to 2 V and displayed an energy density of 45.8 Wh/kg at a power density of 0.41 kW/kg. Additionally, the ASC exhibited exceptional cycling stability and durability, with 98.9% specific capacitance retention after 10000 cycles at multiple strains. These excellent electrochemical performances were attributed to the synergistic effects of the two electrodes with an optimized potential window. Recently, Lu et al. explored a novel approach to improve the conductivity of MnO_2 by fabricating a hydrogenated TiO_2@MnO_2 core-shell nanostructure as presented in Figure 18 (d) [405]. Interestingly, TiO_2 is an inexpensive and electrochemically stable semiconductor with higher electrical conductivity (10^{-5}–10^{-6} S/cm) [406] than that of MnO_2 (10^{-5}-10^{-2} S/cm) [407]. More importantly, the carrier density of pristine TiO_2 can be increased by three orders of magnitude upon hydrogenation. Thus, hydrogen-treated TiO_2 (H-TiO_2) NWs were employed as the core (conducting scaffold) to support electrochemically active MnO_2 and carbon shells (H-TiO_2@C) (Figure 18 (b, c)) and an ASC device based on H-TiO_2@MnO_2 (positive electrode)//H-TiO_2@C (negative electrode) core-shell

NW electrodes was fabricated. This could be reversibly cycled in a potential window up to 1.8 V and exhibited maximum volumetric and specific capacitance values of 0.71 F/cm^3 and 141.8 F/g, respectively, at 10 mV/s. Moreover, the device displayed a good capacitance rate, with 56% volumetric capacitance retention when the scan rate increased from 10 to 400 mV/s. The device further delivered a volumetric energy density of 0.30 mWh/cm^3 (59 Wh/kg) and a volumetric power density of 0.23 W/cm^3 (45 kW/kg). Additionally, the device exhibited excellent cycling performance with 8.8% capacitance loss over 5000 cycles and good flexibility as illustrated by the CV curves measured under different bending conditions (Figure 18 (e)).

Due to their diverse crystal structures, Mn-based oxides can be used as both positive and negative electrodes. For example, a novel ASC cell based on amorphous porous Mn_3O_4 on conducting paper (nickel/graphite/Paper, NPG; Mn_3O_4/NGP) as a negative electrode and an $Ni(OH)_2$ on NGP ($Ni(OH)_2$/NGP) positive electrode were assembled [408]. In the ASC negative electrode, Mn_3O_4 exhibits +2 and +3 Mn valences and provides rich redox reactions for pseudocapacitance generation. In addition, Mn_3O_4 has a suitable working window at negative potential and is also low in cost, highly abundant, and nontoxic. Interestingly, the devices could be reversibly cycled in a wide voltage window (1.3 V) and displayed a high energy density of 0.35 mWh/cm^3, high power density of 32.5 mW/cm^3, and a superior cycling performance (<17% capacitance loss after 12,000 cycles at a high scan rate of 100 mV/s). On the other hand, Gao et al. [409] prepared a free standing Mn_3O_4-graphene (Mn_3O_4-G) paper electrode and applied it as a positive electrode in an ASC cell with free-standing carbon nanotube-graphene (CNT-G) as negative electrode and a PAAK/KCl electrolyte. Figure 18 (f) is a schematic illustration of the systematic fabrication process of the ACS. Compared to pristine graphene paper, the composite paper electrodes with carbon nanotubes or Mn_3O_4 nanoparticles uniformly intercalated between the GNSs exhibited excellent mechanical stability, greatly improved active surface areas, and enhanced ion transportation. As expected, the CNT-G//Mn_3O_4-G cell could be cycled reversibly with a cell voltage window up to 1.8 V (Figure 18 (g)) and achieved a specific capacitance of

72.6 F/g at a current density of 0.5 A/g while still retaining 50.8 F/g at a higher current density of 10 A/g. Moreover, the cell presented an energy density of 32.7 Wh/kg, which is almost threefold higher than that of the CNT-G//CNT-G (10.5 Wh/kg) and Mn_3O_4-G// Mn_3O_4-G (7.1 Wh/kg) supercapacitors. More importantly, when the power density increased to 9.0 kW/kg, the energy density of CNT-G//Mn_3O_4-G was still as high as 22.9 Wh/kg, suggesting that the ASC cell can concurrently provide high energy and power densities. Finally, the cell displayed remarkable cycling stability and retained 86% of its initial capacitance after 10,000 cycles as illustrated in Figure 18 (h).

5.2.3 Metal nitrite-based negative electrodes

The limited electrical conductivity of the metal oxide-based negative electrode hampers the resulting energy storage capacity of ASCs. Therefore, to further improve the efficiency of ASCs, a new class of redox active metal nitrides with superb electrical conductivity (4000–55500 S/cm) has been recently explored [410]. Lu et al. [411] developed vanadium nitrites (VN) as a new class of negative electrodes for ASCs. Vanadium nitride (VN) shows great potential as a negative electrode for ASCs due to its large specific capacitance (1340 F/g), high electrical conductivity (σ_{bulk} = 1.67 x 10^6 /Ωm), and wide operation windows at negative potentials. The ASC cell was fabricated with porous VN NW as the negative electrode and VOx NW as the positive electrode with LiCl/PVA as electrolyte. Initially, porous VN NWs were fabricated through a two-step approach comprising growth of VOx NWs on a carbon cloth substrate by the hydrothermal method followed by post-annealing in ammonia at 600 °C. Notably, the VOx//VN-ASC device exhibited a stable electrochemical window of 1.8 V and achieved a volumetric capacitance of 1.35 F/cm^3 (based on the volume of the entire device; 60.1 F/g, based on the total mass of active materials) at a current density of 0.5 mA/cm^2. More importantly, the ASC cell demonstrated remarkable rate capability with 74.7% retention of the initial capacitance (1.01 F/cm^3) as the current density increased to 5 mA/cm^2. Indeed, a high energy density of 0.61 mWh/cm^3 and a high power density of 0.85 W/cm^3 were achieved with excellent cycling stability

(12.5% reduction in capacitance over 10,000 cycles). The mechanical flexibility test indicated that the electrochemical performance of the device was not affected by folding and twisting, which confirms its potential for application as a flexible energy storage device. However, metal nitrites usually oxidize in aqueous solutions, therefore, to circumvent this problem, these materials have been combined with more stable materials by different processes including CNT encapsulation [412] and graphene wrapping [413]. Among these, vertically aligned graphene nanosheets (GNS) are more effective as substrates due to their large surface area, high conductivity, and light weight. Zhu et al. [414] fabricated an all metal nitrides ASC using titanium nitride (TiN) as positive and iron nitride (Fe_2N) as negative electrode grown on GNS substrate. The schematic illustration of the steps involved in the fabrication process for both electrodes is presented in Figure 19 (a). Initially, thin layers (20 nm) of TiO_2 and ZnO were coated on the GNS substrate by atomic layer deposition. Next, the Fe_2N@GNS negative electrode was produced by converting ZnO into FeOOH via an ion-exchange reaction and subsequent thermal treatment in NH_3. On the other hand, the TiN@GNS positive electrode was prepared by annealing TiO_2@GNS under NH_3 atmosphere. The TiN@GNS//Fe_2N@GNS ASC assembled with PVA/LiCl gel electrolyte could be reversibly cycled up to 1.6 V. The device delivered a stable capacitance of 60 F/g at 10 mV/s with <2% capacity drop after an increase in scan rate to 100 mV/s, suggesting extraordinary rate capability. Moreover, the cycling stability of the device was tested under bending conditions from the 5000^{th} to the 15000^{th} cycle and subsequently under natural state in the last 5000 cycles, suggesting that bending had negligible effect on the capacitance of the device. Interestingly, the device maintained 100% Coulombic efficiency within 20000 cycles (Figure 19 (b)). This result was ascribed to the structure stability of the electrode material in the gel electrolyte. In addition, the device achieved both a high volumetric energy density of 0.55 mWh/cm^3 and a high power density of 220 mW/cm^3 (Figure 19 (c)).

5.2.4 Conducting polymer-based negative electrodes

CPs make up a big family of pseudocapacitive materials that can provide a stable and impressive energy-storage performance in both positive and negative working potentials due to their good conductivities, reversible redox reactions, and environmental friendliness. However, during charging/discharging processes, the CPs may swell and shrink, resulting in mechanical degradation of the electrodes. Thus, poor cycling stability is always observed, especially when they are used as negative electrodes. Therefore, different strategies have been developed to enhance the pseudocapacitance of CPs, such as optimizing the nanostructures, doping with surfactant ions, and fabricating composites with other species. Lu et al. [415] synthesized highly ordered 3D α-Fe_2O_3@PANi core-shell NWAs as negative electrodes for ASCs. The α-Fe_2O_3 NWAs were electrodeposited on carbon cloth with subsequent annealing in air. A thin layer of PANi was then electrodeposited on the α-Fe_2O_3 NWs to produce the 3D α- Fe_2O_3@PANi core-shell NW. This unique α-Fe_2O_3@PANi core-shell nanoarchitecture provided a large reaction surface area, fast ion and electron transfers, and good structure stability, all of which improved the electrochemical performance. The ASC cell was then assembled with α-Fe_2O_3@PANi as negative and PANi on carbon cloth as positive electrodes. The ASC cell displayed a high volumetric capacitance of 2.02 mF/cm^3 (based on the volume of device), a high energy density of 0.35 mWh/cm^3 at a power density of 120.51 mW/cm^3, and very good cycling stability with a capacitance retention of 96% after 10,000 cycles. Likewise, Jin et al. [416] assembled an ASC using CNT/PANi and CNT/MnO_2/graphene paper as negative and positive electrodes, respectively, with a PVP-Na_2SO_4 gel electrolyte as presented in Figure 19 (d). The assembled ASC operated in a higher voltage range up to 1.6 V and achieved an energy density of 24.8 Wh/kg and a high power density of 2230 W/kg (Figure 19 (e, f)). PEDOT is another promising candidate for application as a negative electrode in ASC due to its higher reduction potential ascribed to the electron donating nature of its oxygen groups. In addition, the high stability of PEDOT in its oxidized state enables it to exhibit electrochemical activity in a wide potential

window. For example, an ASC device was fabricated on Au-coated PEN plastic substrates using PEDOT and PANi as negative and positive electrodes, respectively [417]. This ASC device could be cycled in a wide voltage window of 1.6 V and exhibited a volumetric stack capacitance of 34 F/cm^3 at a current density of 0.5 mA/cm^2. Moreover, the PANi//PEDOT ASC device displayed the highest energy density (12 mWh/cm^3), which was six-fold higher than that for the symmetric PEDOT cell (E = 2 mWh/cm^3) and twofold higher than the PANi-based cell (E = 5 mWh/cm^3). Finally, the cycling stability of the ASC was determined as 80% over 10,000 cycles at a current density of 2 mA/cm^2.

5.2.5 Some other negative electrodes

In addition to the above discussed materials, some new promising materials have been recently employed as negative electrodes in ASCs. Specifically, metal phosphides, having both metalloid characteristics and good electric conductivity, are considered as advanced electrode materials for ASCs. A 3D cobalt phosphide (CoP) NW on carbon cloth was presented as the negative electrode with a MnO_2 NW as the positive electrode and LiCl/PVA as the gel electrolyte [418]. Interestingly, the resultant ASC cell could be successfully cycled in a voltage window up to 1.6 V and delivered good supercapacitive characteristics including a volumetric capacitance of 1.94 F/cm^3, and energy and power densities of 0.69 mWh/cm^3 and 114.20 mW/cm^3, respectively. Iron selenide ($FeSe_2$) is another suitable candidate for ASC application due to its excellent electrochemical activities and an appropriate operating window at negative potentials [419]. The assembled ASC was based on $NiCo_2O_4$ and $FeSe_2$ as positive and negative electrodes, respectively, and a KOH/PVA electrolyte exhibited an energy density of 10.4 Wh/kg and a maximum power density of 1.2 kW/kg (operating window: 1.5 V). Phytic acid, has a strong chelating ability and can easily bond with metal ions to generate cross-linked metal phytate complexes. Thus, using phytic acid treatment, NiZn-phytate and Fe-phytate were developed to serve as positive and negative electrodes, respectively [420]. The resultant Ni/Fe cell delivered excellent electrochemical properties with long-term stability (~86% retention after 8000 cycles at

20.83 A/g). In addition, the ASC cell maintained its electrochemical performance under various bending conditions, suggesting great potential for application as a power supply for wearable smart products. A summary of the electrochemical performances of flexible solid-state asymmetric designs based on different positive and negative electrodes with their corresponding gel electrolytes is presented in Table 4 [421-465].

6. Some potential practical applications

6.1 Piezoelectric SCs

In recent years, various novel implantable/wearable healthcare devices (spirometers, sphygmomanometers, and wristbands) have been employed in a broad range of applications ranging from physical activity monitoring to more analytical applications such as diet tracking, mental stress detection, and rehabilitation [466]. However, flexible efficiency of the power supplying unit is still one of the bottlenecks for wearable electronics. Thus, a new self-sustainable energy storage device that can harvest/store body energy (breathing, arm pressing, and chest compression) and power smart electronics shows great potential for application in next generation implantable/wearable electronics. The recent discovery of electricity generation using piezoelectric ZnO NWs has attracted significant attention on piezoelectric materials in energy harvesting and transducer technology [467]. Piezoelectric materials can convert ubiquitously irregular and low-frequency mechanical vibrations into electricity and have been extensively studied for their use as nanogenerators [468]. Thus, mechanical vibrations (energy) can be efficiently converted and stored in piezoelectric SCs using a piezoelectric film to replace traditional separators. Owing to their excellent piezoelectric properties and mechanical flexibility, polyamide (PA) and PVDF films have been demonstrated as wearable flexible energy generators [469].

The piezoseparator (piezoelectric film) is a key component in piezoelectric SCs and is typically a well-polarized PVDF film placed between the electrodes. In the piezo-electrochemical

mechanism, the external mechanical impacts develop a piezoelectric potential across the PVDF films and drive ions in the electrolyte to migrate towards the interface of the SC electrode (forming an electronic double layer or pseudocapacitance at the interface), storing the electricity as electrochemical energy (Figure 20 (a)). Thus, the integration of energy generation (mechanical generation of energy from a piezoelectric potential) and storage (storing in SCs) systems can effectively supply power without using an external DC source [470].

FSSC was assembled using functionalized carbon cloth as positive and negative electrodes with polarized PVDF films coated with a H_2SO_4/PVA gel electrolyte [471]. The integrated piezo-supercapacitor exhibited a specific capacitance of 357.6 F/m^2 (current density: 8 A/m^2), a power density of 49.67 mWh/m^2, and an energy density of 400 mW/m^2. Moreover, when the SSC was charged under a continuous compressive force with an average frequency of 4.5 Hz, the voltage of the piezo-supercapacitor increased to 100 mV within 40 s. The stored electric energy was determined from the discharge curve as 0.25 mAh at a constant current of 100 mA. More recently, the integration of a pseudo-supercapacitor and piezoelectric materials as a hybrid energy harvesting and storage device was realized using pseudocapacitive MnO_2 NWs as positive and negative electrodes and PVDF-ZnO coated with H_3PO_4/PVA film as the separator (as well as a piezoelectric) [472]. The addition of ZnO NWs in the PVDF matrix induced polarization of ions in the composite film without electrical poling. When a compressive force with palm impact was applied, the voltage of the device increased from 35 to 145 mV (110 mV charged) in 300 s. In addition, after realising the compression force, the device sustained the stored energy for ~150 s. The fabrication of flexible piezoelectric SCs using a laser engraving technique by integrating a triboelectric nanogenerator and an MSC array into a single device was recently reported [473]. A high degree of integration was realized through double-faced laser engraving of the PI substrate. The triboelectric nanogenerator and MSC were fabricated by using two sides of the laser-induced graphene. The nanogenerator generated

electricity from ambient mechanical vibrations with high output, while the rectified electrical energy was directly stored in the MSC that could be charged to 3 V in 117 min.

6.2 Photo-supercapacitors

Solar energy, the cleanest and most easily available energy source to date, is unfortunately limited by access to sunlight. Integrating solar cells with energy storage devices is an exclusive strategy to extend the practical applications of solar energy beyond the imposed restrictions of sunlight availability [376]. The idea of coupling solar cells and SCs as a complete energy conversion and storage device is known as “photo-supercapacitors,” whereby the solar energy can be efficiently transferred and converted to electrical energy by adopting an SC as the energy delivery system that is schematically shown in Figure 20 (b) [474].

A coaxial, all-solid-state “energy fiber” was introduced by integrating a dye-sensitized solar cell (DSSC) with SCs comprising CNTs@Ti wire electrodes and a PVA-H_3PO_4 gel electrolyte [475]. The photoelectric conversion efficiency was determined as 2.73%, while the energy storage efficiency reached 75.7% with specific capacitances up to 0.156 mF/cm (3.32 mF/cm^2) and power densities up to 0.013 mW/cm (0.27 mW/cm^2) at a current of 50 mA. Likewise, Zhang et al. [476] assembled coaxial SCs by coupling P3HT:PCBM@TiO_2@Ti wire (PCBM: [6,6]-phenyl-C61-butyric acid methyl ester) and PEDOT/PSS as the photo-electrode and MWCNTs as the SC electrode with a PVA/H_3PO_4 electrolyte. The photo-conversion and energy storage efficiencies were investigated as a function of MWCNT length in the SCs, achieving 0.4% and 0.82 optimum performances, respectively. Furthermore, the coaxial structure offers good effective contact area and favors rapid charge transport and it can be easily woven into various structures such as lightweight textiles. In addition to DSSC, a wearable energy-smart ribbons photo-supercapacitor was recently demonstrated by integrating a perovskite solar cell (PSC) on top of a symmetric SC [477]. This flexible integrated device displayed the highest photoconversion efficiency (10.41%), while the energy storage efficiency was ~67%. The SC held an energy density of 1.15 mWh/cm^3 and a power density of

243 mW/cm^3 under solar illumination. Even with their stability and the need for appropriate sealing to prevent fast environmental aging of the PSCs concerned, DSSCs represent a more reliable technology for integrated devices.

6.3 Shape-memory Supercapacitors

Many recent applications (wearable electronics, bendable smart phones, and biomedical devices) and their energy storage devices, undergo irreversible deformation. Therefore, electronic devices and their power units need to exhibit mechanically deformable ability. Thus, stretchable, compressible, and shape-memory (shape-recoverable) SCs have attracted much attention for future applications [12].

Incorporation of shape-memory materials into SCs can recover devices back to their initial shape or size after irreversible deformations in practical applications. There are two main categories of shape-memory materials, namely shape-memory alloys (SMAs) and polymers (SMPs) [478]. The shape-memory effect of SMAs arises from a reversible crystalline phase change known as a martensite-austenite transformation. When heated to a certain temperature, the deformed SMAs return to their original shape and all plastic deformations are removed. The most prominent SMAs are based on nickel-titanium (NiTi) due to its superior mechanical and electrical characteristics.

A shape-memory SC was realized using graphene coated on TiNi alloy flakes as the negative electrode and an ultrathin MnO_2/Ni film as the positive electrode in gel electrolytes [478]. It displayed a specific capacitance of 53.8 F/g at 0.5 A/g. The bent device regained its original planar shape within 550 s when heated to ambient temperature. The recovery speed of this SC was relatively low. Recently, NiTi wires were applied as current collectors and substrates for the active materials (MnO_2 and PPy) in a twisted fiber shape-memory SC, whereby serious plastic deformations were restored to an undistorted state within a few seconds [479] while maintaining near-identical capacitive performances.

Above the glass transition temperature (Tg; amorphous polymers) and melting temperature (Tm; crystalline polymers), SMPs are soft and light-weight and can be extended to several hundreds of percent. SMPs can memorize more than one shape and recover their original form when subjected to various stimuli such as temperature, light, magnetic fields, and electric currents. Wrapping aligned CNT sheets onto a shape-memory polyurethane (SMPU) substrate enabled a shape-memory and fiber-shaped MSC [480]. After 500 cycles of deformation and recovery at a strain of 50%, its electrochemical properties exhibited no significant decrease, suggesting excellent stability of the device structure. However, its maximum specific capacitance was only 42.3 mF/cm, which could be enhanced by introducing pseudocapacitve materials. Densely compacted CNT layers and PANi layers were coated on the PVA/CNT SMPU fibers through layer by layer (LBL) technology [481]. The resulting shape-memory SCs possessed shape memory properties and exhibited outstanding specific capacitance values exceeding 427 F/cm^3.

6.4 Microbial Supercapacitors

A microbial electrochemical technique converts biomass directly to electricity or fuel, harvesting electrons from specific bacterial species known as "*exoelectrogens*" ("exo:" out of and "electrogene:" bacteria-producing electrons) via their unique extracellular electron transport (EET). The schemetic representation of working mechanism of Microbial SCs (MSC) is presented in Figure 20 (c). Exoelectrogens have been implemented in various microbial electrochemical technologies (METs), such as microbial fuel cells (MFCs), microbial electrolysis cells (MECs), and microbial reverse electrodialysis cells (MRCs) [482]. Recently, several reports have demonstrated that exoelectrogens such as Geobacter, Shewanella, and Proteobacteria, store electrons and can be used as capacitors [483] with a current density in the range of 1.2–90 A/m^2. The high current density observed in these reports demonstrated the ability to use biological pseudocapacitance as a potential renewable method for energy generation and storage.

In 2012, Malvankar et al. [484] demonstrated the pseudocapacitive redox nature of c-type cytochrome biofilms. These biofilms displayed low self-discharge and good charge/discharge reversibility. The capacitance of *G. sulfurreducens* biofilms was determined as 620 $\mu F/cm^2$ at the open circuit potential. A novel bio-inspired microbial SC was recently presented utilizing pseudocapacitance generated by an exoelectrogen, *Geobacter spp.,* grown on a single-layer graphene film and 3D graphene-scaffold electrodes [485]. Charging and discharging the microbial SC were performed by regulating the respiration of the exoelectrogen (Figure 20(c)). The microbial SC delivered a specific capacitance of 17.85 mF/cm^2 with outstanding cycling stability over one million cycles. It also demonstrated maximum current and power densities of 531.2 A/m^2 (1,060,000 A/m^3) and 197.5 W/m^2 (395,000 W/m^3), respectively. Notably, its areal power density was 2.5-fold, 19-fold, three orders of magnitude, and four orders of magnitude greater than those of solar cell (outdoor), enzymatic fuel cell, thermoelectric energy harvester, and RF energy harvester, respectively [486]. An overview of several new applications of FSSCs are shown in Figure 21.

7. Conclusions and Future Challenges

FSSCs are emerging as breakthrough miniaturized energy storage systems with diverse technological applications such as wearable electronics, smart clothes, electronic skins, and implantable medical devices. This review introduces recent progress in the fundamentals of charge storage mechanisms, emerging new electrode materials and electrolytes, and novel cell designs of FSSCs. To date, studies have demonstrated that excellent progress has been made in the development of new flexible electrodes and cell designs (symmetric and asymmetric) for FSSCs. Moreover, the latest discoveries of new materials with controlled architecture hold great promise towards performance improvement in terms of high power, energy densities, and cycle life. FSSC performance is commonly defined in terms of gravimetric and volumetric scales that foster the development of new electrode designs such as free-standing and substrate-supported

designs. The former is lightweight and utilizes the entire electrode material to achieve high performance, thereby avoiding the extra weight of current collectors and additives, however, it is fragile and difficult to handle. On the other hand, a large variety of flexible substrates, such as metal foils/wires, paper, textiles, PETs, and fibers have been investigated to achieve high performance FSSCs. Owing to their porous structure, light weight, and high flexibility, textile- and paper-based current collectors are considered promising substrates for FSSC application. In addition to flexible electrodes, extensive efforts have been devoted towards exploring new gel electrolytes that improve the overall performance of the SC. Thus, various new POM-incorporated gels, such as SiWA, PWA, and BWA, have been revealed as promising electrolytes for FSSC application due to their good conductivity and pseudocapacitance. An emerging new strategy of redox-active electrolyte-enhanced devices have emerged through the introduction of pseudocapacitive contribution in electrolytes.

Several new promising materials such as MXenes, MOFs, POMs, and metal nitrides with properties such as high electronic conductivity and surface controlled porosity have been adopted in the field of FSSCs. Moreover, the very recent discovery of MXenes has demonstrated great potential for the design of FSSCs with enhanced volumetric energy density. The application of other layered materials (phosphorene) as electrodes in FSSCs is still in its infancy and needs further development, including new reducing agents, etchants, and intercalants to synthesize high quality large-scale materials. Various potential practical applications have been introduced, including piezoelectric SCs, photo-supercapacitors, and shape-memory SCs. This is a great step towards achieving smart SCs.

Despite the many achievements and encouraging results, the development of a new generation of miniaturized FSSCs is still at its early stage. Much effort is still needed before the emergence of real technological implementations. Herein, we summarize some of the current challenges and future directions for the practical realization of FSSCs:

(1) A detailed analysis is necessary to deeply understand the energy storage mechanisms at the electrode/polymer gel-electrolyte interface. Many theoretical studies have been reported on liquid electrolytes, however, the theoretical basis of the charge storage mechanism in gel electrolytes is complicated and difficult to understand as the ions are trapped in the polymer chains. Therefore, advanced *in-situ* characterization (microscopic and spectroscopic) and simulation techniques need to be developed to elucidate the charge storage mechanisms of FSSCs.

(2) There is no standardized method for the evaluation of electrochemical features and the mechanical flexibility of FSSCs. It is essential to report volumetric electrochemical features since the mass of the active material is negligible when compared to the mass of the whole device. Likewise, different approaches have been undertaken to analyze the mechanical integrity of FSSCs, thereby highlighting the need for standard methods to compare the mechanical feasibility.

(3) The FSSC performance relies entirely on the electrode material and electrolytes. As discussed in section 4, the unusual electronic, chemical, and surface properties of 2D materials beyond graphene (MXenes, phosphorene, germanene, and tinene,) makes them promising electrodes for FSSCs. However, mass production of high quality 2D materials is still a great challenge and therefore, more effort should be taken to elucidate new synthetic methods that meet industrial requirements.

(4) Several new investigations on gel electrolytes resolved the initial problems of low ionic conductivity (10^{-3}-10^{-1} S/cm) and thermal instability. However, more research on improving device performance in terms of capacitance, energy density, stability, and operating cell voltage using new redox-active electrolytes is required.

(5) High production cost is another challenge for the practical implementation of FSSC technology. Therefore, future studies should focus on the development of highly flexible and

energetic FSSCs using cost-effective raw materials. Moreover, single-step processing materials and electrolytes are more favorable for practical application.

(6) The fast-growing popularity of intelligent electronics urges the continuous development of smart power sources with integrated stimulus-response. In this context, new device designs, which are flexible, bendable, foldable, and stretchable, need to be explored. The integration of the different functional electronic devices in a single component is of great interest. With more effort on optimization, smart SCs will play important roles in lightweight, flexible, and wearable capacitive devices in the near future.

Acknowledgment

DPD acknowledges the support of the University of Adelaide, Australia for the grant of a Research Fellowship (VC Fellow), the Secretary for Universities and Research of the Ministry of Economy and Knowledge of the Government of Catalonia, and the Co-fund program of the Marie Curie Actions of the 7th R&D Framework Program of the European Union. This work was also supported by the National Research Foundation of Korea (NRF-2015M3A7B 4050 424).

References

[1] (a) N. A. Kyeremateng, T. Brousse, D. Pech, *Nat. Nanotechnol.*, 2017, 12, 7-15, (b) H. Sun, Y. Zhang, J. Zhang, X. Sun, H. Peng, *Nat. Rev. Mater.* 2017, 2, 17023 (b) M. Beidaghi, Y. Gogotsi, *Energy Environ. Sci.* 2014, 7, 867-884. (b) Z. Liu, J. Xu, D. Chen, G. Shen, *Chem. Soc. Rev.,* 2015, 44, 161-192 (c) D. Yu, Q. Qian, L. Wei, W. Jiang, K. Goh, J. Wei, J. Zhang, Y. Chen, *Chem. Soc. Rev.,* 2015, 44, 647-662.

[2] (a) H. He, Y. Fu, T. Zhao, X. Gao, L. Xing, Y. Zhang, X. Xue, *Nano Energy* 2017, 39, 590-600 (b) D. Qi, Y. Liu, Z. Liu, L. Zhang, X. Chen, *Adv. Mater.*, 2017 DOI: 10.1002/ adma.201602802. (c) X. Peng, L. Peng, C. Wu and Y. Xie, *Chem. Soc. Rev*., 2014, 43, 3303-3323. (d) D. Pech, M. Brunet, H. Durou, P. H. Huang, V. Mochalin, Y. Gogotsi, P. L. Taberna and P. Simon, *Nat. Nanotechnol.*, 2010, 5, 651-654

[3] (a) F. Wang, X. Wu, X. Yuan, Z. Liu, Y. Zhang, L. Fu, Y. Zhu, Q. Zhou, Y. Wu, W. Huang, *Chem. Soc. Rev.*, 2017, DOI: 10.1039/c7cs00205j. (b) F. Bonaccorso, L. Colombo, G. Yu, M. Stoller, V. Tozzini, A. C. Ferrari, R. S. Ruoff and V. Pellegrini, *Science*, 2015, 347, 10, DOI: 10.1126/science.1246501 (c) L. Hu and Y. Cui, *Energy Environ. Sci.*, 2012, 5, 6423-6435, (d) L. Li, C. Fu, Z. Lou, S. Chen, W. Han, K. Jiang, D. Chen, G. Shen, *Nano Energy* 2017, https://doi.org/10.1016/j.nanoen.2017.08.060

[4] (a) S. Bauer, *Nat. Mater* 2013, 12, 871-872 (b) E. Gibney, *Nature* 2015, 528, 26-28 (c) I. M. Mosa, A. Pattammattel, K. Kadimisetty, P. Pande, M. F. El-Kady, G. W. Bishop, M. Novak, R. B. Kaner, A. K. Basu, C. V. Kumar, J. F. Rusling, *Adv. Energy Mater.* 2017, 7, 1700358

[5] (a) X. Pu, L. Li, M. Liu, C. Jiang, C. Du, Z. Zhao, W. Hu, Z. L. Wang, *Adv. Mater.*, 28, 2016, 98-105 (b) F. R. Fan, W. Tang, Z. L. Wang, *Adv. Mater.* 2016, 28, 4283-4305 (c) D. Son, J. Lee, S. Qiao, R. Ghaffari, J. Kim, J. E. Lee, C. Song, S. J. Kim, D. J. Lee, S. W. Jun, S. Yang, M. Park, J. Shin, K. Do, M. Lee, K. Kang, C. S. Hwang, N.S. Lu, T.

Hyeon, D.H. Kim, *Nat. Nanotechnol.* 2014, 9, 397-404 (d) T. Q. Trung, N. E. Lee, *Adv. Mater.* 2016, 28, 4338-4372.

[6] (a) M. Salanne, B. Rotenberg, K. Naoi, K. Kaneko, P.-L. Taberna, C. P. Grey, B. Dunn, P. Simon, *Nat. Energy*, 2016, 1, 16070. (b) D. P. Dubal, O. Ayyad, V. Ruiz, P. Gomez-Romero, *Chem. Soc. Rev.,* 2015, 44, 1777-1790 (c) M. R. Lukatskaya, B. Dunn and Y. Gogotsi, *Nat. Commun.*, 2016, 7, 12647-12659. (d) Y. Wang, Y. Song, Y. Xia, *Chem. Soc. Rev.*, 2016, 45, 5925-5950 (e) Z. Yu, L. Tetard, L. Zhai, J. Thomas, *Energy Environ. Sci.*, 2015, 8, 702-730.

[7] (a) Y. Wang, Y. Song, Y. Xia, *Chem. Soc. Rev.*, 2016, 45, 5925-5950 (b) D. P. Dubal, P. Gomez-Romero, B. R. Sankapal, R. Holze, *Nano Energy* 2015, 11, 377-399, (b) G. P. Wang, L. Zhang and J. J. Zhang, *Chem. Soc. Rev.*, 2012, 41, 797-828. (c) Q. Lu, J. G. Chen and J. Q. Xiao, *Angew. Chem., Int. Ed.*, 2013, 52, 1882-1889

[8] (a) S. Yang, R. E. Bachman, X. Feng and K. Mullen, *Acc. Chem. Res.*, 2013, 46, 116-128; (b) H. B. Wu, G. Zhang, L. Yu and X. W. Lou, *Nanoscale Horiz.*, 2016, 1, 27-40. (c) C. Zhang, W. Lv, Y. Tao and Q. H. Yang, *Energy Environ. Sci.*, 2015, 8, 1390-1403

[9] (a) Z. Wu, L. Li, J. Yan, X. Zhang, *Adv. Sci.* 2017, 4, 1600382 (b) Z. Yang, J. Ren, Z. Zhang, X. Chen, G. Guan, L. Qiu, Y. Zhang, H. Peng, *Chem. Rev.*, 2015, 115, 5159-5223. (c) K. Naoi, W. Naoi, S. Aoyagi, J. Miyamoto, T. Kamino, *Acc. Chem. Res.*, 2013, 46, 1075-1083

[10] (a) B. E. Conway, Electrochemical Supercapacitors Scientific Fundamentals and Technological Applications, Kluwer Academic/Plenum Publishers, New York, 1999; (b) A. Yu, V. Chabot and J. Zhang, Electrochemical supercapacitor for energy storage and delivery: Fundamentals and application, CRC Press, by Taylor & Francis Group, 2013.

[11] (a) C. Yan, P. S. Lee, *Small* 2014, 10, 3443-3460, (b) S. Y. Lee, K. H. Choi, W. S. Choi, Y. H. Kwon, H. R. Jung, H. C. Shin, J. Y. Kim, *Energy Environ. Sci.*, 2013, 6, 2414-

2423, (c) S. Yao, Y. Zhu, *Adv. Mater.* 2015, 27, 1480-1511, (d) Y. Zhang, Y. Huang, J. A. Rogers, *Curr. Opin. Solid State Mater. Sci.* 2015, 19, 190-199

[12] (a) W. Liu, M. S. Song, B. Kong and Y. Cui, *Adv. Mater.*, 2017, DOI: 10.1002/adma.201603436. (b) K. Guo, N. Yu, Z. Hou, L. Hu, Y. Ma, H. Li and T. Zhai, J. Mater. Chem. A, 2017, 5, 16-30 (c) T. Q. Trung, N. E. Lee, *Adv. Mater.*, 2017, DOI: 10.1002/adma.201603167.

[13] (a) Y. Matsuda, M. Morita, M. Ishikawa, M. Ihara, *J. Electrochem. Soc.* 1993, 140, L109-L110 (b) A. Clemente, S. Panero, E. Spila, B. Scrosati, *Solid State Ionics* 1996, 85, 273-277. (c) S. A. Hashmi, R. J. Latham, R. G. Linford, W. S. Schlindwein, *Polym Int* 1998, 47, 28-33.

[14] (a) A. Lewandowski, M. Zajder, E. Frachowiak, F. Beguin, *Electrochim. Acta* 2001, 46, 2777-2780. (b) K. R. Prasad, N. Munichandraiah, *Electrochem. Solid-State* 2002, 5, A271-A274. (c) Y. G. Wang, X. G. Zhang, *Solid State Ionics* 2004, 166, 61-67.

[15] (a) L. Liu, Z. Niu, J. Chen, *Chem. Soc. Rev.,* 2016, 45, 4340-4363. (b) X. Wang, K. Jiang, G. Shen, *Mater. Today.* 2015, 18, 265-272 (c) Y. Z. Zhang, Y. Wang, T. Cheng, W. Y. Lai, H. Pang, W. Huang, *Chem. Soc. Rev.,* 2015, 44, 5181-5199. (d) X. Wang, X. Lu, B. Liu, D. Chen, Y. Tong, G. Shen, *Adv. Mater.* 2014, 26, 4763-4782.

[16] (a) P. Yang, W. Mai, *Nano Energy*, 2014, 8, 274–290 (b) X. Lu, M. Yu, G. Wang, Y. Tong, Y. Li, *Energy Environ. Sci.*, 2014, 7, 2160-2181 (d) A. Tyagi, K. M. Tripathi, R. K. Gupta*, J. Mater. Chem. A*, 2015, 3, 22507-22541, (a) L. Li, Z. Wu, S. Yuan, X. B. Zhang, *Energy Environ. Sci.*, 2014, 7, 2101-2122,

[17] (a) H. Chen, S. Zeng, M. Chen, Y. Zhang, Q. Li, Carbon 2015, 92, 271-296, (c) X. Wang, G. Shi, *Energy Environ. Sci.*, 2015, 8, 790-823 (d) G. Xiong, C. Meng, R. G. Reifenberger, P. P. Irazoqui, T. S. Fisher, *Electroanalysis* 2014, 26, 30-51

[18] (a) W. K. Chee, H. N. Lim, Z. Zainal, N. M. Huang, I. Harrison, Y. Andou, *J. Phys.*

Chem. C 2016, 120, 4153-4172 (b) T. Chen, L. Dai, *J. Mater. Chem. A*, 2014, 2, 10756-10775, (c) Y. Huang, H. Li, Z. Wang, M. Zhu, Z. Pei, Q. Xue, Y. Huang, C. Zhi, *Nano Energy* 2016, 22, 422-438.

[19] (a) J. Sun, Y. Huang, Y. N. S. Sea, Q. Xue, Z. Wang, M. Zhu, H. Li, X. Tao, C. Zhi, H. Hu, *Mater. Today Energy* 2017, 5, 1-14 (b) S. T. Senthilkumar, Y. Wang, H. Huang, *J. Mater. Chem. A*, 2015, 3, 20863-20879 (c) K. Jost, G. Dion, Y. Gogotsi, *J. Mater. Chem. A*, 2014, 2, 10776-10787

[20] (a) H. Wang, A. C. Forse, J. M. Griffin, N. M. Trease, L. Trognko, P. L. Taberna, P. Simon, C. P. Grey, *J. Am. Chem. Soc.*, 2013, 135, 18968-18980 (b) F. Béguin, V. Presser, A. Balducci, E. Frackowiak, *Adv. Mater.* 2014, 26, 2219-2251 (c) P. Simon, Y. Gogotsi, *Acc. Chem. Res.*, 2013, 46, 1094-1103.

[21] (a) V. Augustyn, P. Simon and B. Dunn, *Energy Environ. Sci.*, 2014, 7, 1597-1614 (b) J. R. Miller, A. F. Burke, *Electrochem. Soc. Interface*, 2008, 53-57. (c) P. Simon, Y. Gogotsi, *Nat. Mater.*, 2008, 7, 845-854 (d) J. R. Miller, P. Simon, *Science*, 2008, 321, 651-652

[22] (a) S. Zheng, Z. S. Wu, S. Wang, H. Xiao, F. Zhou, C. Sun, X. Bao, H. M. Cheng, *Energy Storage Mater.*, 2017, 6, 70-97. (b) H. Xiao, Z. S. Wu, L. Chen, F. Zhou, S. Zheng, W. Ren, H. M. Cheng, X. Bao, *ACS Nano*, 2017, 11, 7284-7292. (c) N. A. Choudhury, S. Sampath, A. K. Shukla, *Energy Environ. Sci.*, 2009, 2, 55-67; (d) G. Lota, E. Frackowiak, *Electrochem. Commun.*, 2009, 11, 87-90.

[23] (a) J. Chmiola, G. Yushin, Y. Gogotsi, C. Portet, P. Simon, P. L. Taberna, *Science*, 2006, 313, 1760-1763; (b) C. Largeot, C. Portet, J. Chmiola, P. L. Taberna, Y. Gogotsi, P. Simon, *J. Am. Chem. Soc.*, 2008, 130, 2730-2731.

[24] H. Shi, *Electrochim. Acta,* 1996, 41, 1633-1639.

[25] S. Kondrat, N. Georgi, M. V. Fedorov, A. A. Kornyshev, *Phys. Chem. Chem. Phys.*,

2011, 13, 11359-11366.

[26] (a) C. Merlet, B. Rotenberg, P. A. Madden, P. L. Taberna, P. Simon, Y. Gogotsi and M. Salanne, *Nat. Mater.*, 2012, 11, 306-310 (b) M. Deschamps, E. Gilbert, P. Azais, E. R. Pinero, M. R. Ammar, P. Simon, D. Massiot, F. Beguin, *Nat. Mater.*, 2013, 12, 351-358.

[27] (a) T. Brousse, D. Bélanger, J. W. Long, *J. Electrochem. Soc.* 2015, 162, A5185-A5189 (b) D. P. Dubal, P. Gomez-Romero, Metal oxides in supercapacitors, Elsevier 2017.

[28] E. Herrero, L. J. Buller, H. D. Abruna, *Chem. Rev.*, 2001, 101, 1897-1930.

[29] X. Wang, G. Yushin, *Energy Environ. Sci.*, 2015, 8, 1889-1904.

[30] (a) M. D. Stoller, R. S. Ruoff, *Energy Environ. Sci.*, 2010, 3, 1294-1301 (b) S. Roldan, D. Barreda, M. Granda, R. Menendez, R. Santamaria, C. Blanco, *Phys. Chem. Chem. Phys.,* 2015, 17, 1084-1092 (c) Y. Gogotsi, P. Simon, *Science*, 2011, 334, 917-918 (d) Y. J. Kang, S.-J. Chun, S.-S. Lee, B.-Y. Kim, J. H. Kim, H. Chung, S.-Y. Lee and W. Kim, *ACS Nano*, 2012, 6, 6400–6406.

[31] J. Bae, M. K. Song, Y. J. Park, J. M. Kim, M. Liu and Z. L. Wang, *Angew. Chem., Int. Ed.*, 2011, 50, 1683-1687.

[32] (a) Y. Cheng, S. Lu, H. Zhang, C. V. Varanasi and J. Liu, *Nano Lett.*, 2012, 12, 4206-4211, (b) X. Xiao, T. Li, Z. Peng, H. Jin, Q. Zhong, Q. Hu, B. Yao, Q. Luo, C. Zhang, L. Gong, J. Chen, Y. Gogotsi and J. Zhou, *Nano Energy*, 2014, 6, 1-9.

[33] (a) D. Feng, Y. Lv, Z. Wu, Y. Dou, L. Han, Z. Sun, Y. Xia, G. Zheng, D. Zhao, *J. Am. Chem. Soc.* 2011, 133, 15148-15156 (b) K. Xiao, L. X. Ding, G. Liu, H. Chen, S. Wang, H. Wang, *Adv. Mater.* 2016, 28, 5997-6002

[34] (a) Y. He, W. Chen, X. Li, Z. Zhang, J. Fu, C. Zhao, E. Xie, *ACS Nano* 2013, 7, 174-182, (b) K. Qin, J. Kang, J. Li, C. Shi, Y. Li, Z. Qiao, N. Zhao, *ACS Nano*, 2015, 9, 481-487.

[35] V. L. Pushparaj, M.M. Shaijumon, A. Kumar, S. Murugesan, L. Ci, R. Vajtai, R.J.

Linhardt, O. Nalamasu, P. M. Ajayan*, Proc. Natl. Acad. Sci.* 2007, 104, 13574-13577

[36] (a) Z. Cao, B. B. Wei, *Energy Environ. Sci.* 2013, 6, 3183-3201 (b) Z. Zhang, T. Zhai, X. Lu , M. Yu , Y. Tong , K. Mai , *J. Mater. Chem. A* 2013*,* 1, 505 -509 (c) J. Chang, S. Adhikari, T. H. Lee, B. Li, F. Yao, D. T. Pham, V. T. Le, Y. H. Lee, *Adv. Energy Mater.* 2015, 5, 1500003.

[37] Y. J. Kang, S. J. Chun, S. S. Lee, B. Y. Kim, J. H. Kim, H. Chung, S. Y. Lee, W. Kim, *ACS Nano*, 2012, 6, 6400-6406.

[38] (a) A. K. Geim and K. S. Novoselov, *Nat. Mater.*, 2007, 6, 183-191, (b) A. K. Geim, *Science*, 2009, 324, 1530-1534, (c) L. Dai, *Acc. Chem. Res.*, 2012, 46, 31-42.

[39] (a) L. L. Zhang, R. Zhou, X. Zhao, *J. Mater. Chem.*, 2010, 20, 5983-5992, (b) C. Xu, B. Xu, Y. Gu, Z. Xiong, J. Sun and X. Zhao, *Energy Environ. Sci.*, 2013, 6, 1388-1414.

[40] Z. Weng, Y. Su, D. W. Wang, F. Li, J. Du, H.-M. Cheng, *Adv. Energy Mater.* 2011, 1 917-922

[41] N. Li, G. Yang, Y. Sun, H. Song, H. Cui, G. Yang, C. Wang, *Nano Lett.* 2015, 15, 3195-3203

[42] (a) G. K. Wang, X. Sun, F. Y. Lu, H. T. Sun, M. P. Yu, W. L. Jiang, C. S. Liu and J. Lian, *Small*, 2012, 8, 452–459, (b) Z. Lei, N. Christov, X. S. Zhao, *Energy Environ. Sci.*, 2011, 4, 1866-1873.

[43] C. Liu, Z. Yu, D. Neff, A. Zhamu, B. Z. Jang, *Nano Lett.*, 2010, 10, 4863-4868.

[44] Y. Wang, J. Chen, J. Cao, Y. Liu, Y. Zhou, J. H. Ouyang, D. Jia, *J. Power Sources*, 2014, 271, 269-277.

[45] B. G. Choi, J. Hong, W. H. Hong, P. T. Hammond, H. Park, *ACS Nano*, 2011, 5, 7205-7213.

[46] D. Yu and L. Dai, J. Phys. Chem. Lett., 2009, 1, 467-470.

[47] (a) Y. Shao, M. F. El-Kady, L. J. Wang, Q. Zhang, Y. Li, H. Wang, M. F. Mousaviae, R.

B. Kaner, *Chem. Soc. Rev.,* 2015, 44, 3639-3665 (b) A. Borenstein, O. Hanna, R. Attias, S. Luski, T. Brousse, D. Aurbach, *J. Mater. Chem. A*, 2017, 5, 12653-12672

[48] (a) G. Zhang, X. Xiao, B. Li, P. Gu, H. Xue, H. Pang, *J. Mater. Chem. A*, 2017, 5, 8155-8186 (b) F. Shi, L. Li, X. Wang, C. Gu, J. Tu, *RSC Adv.*, 2014, 4, 41910-41921.

[49] (a) C. Zhang, T. M. Higgins, S. H. Park, S. E. O'Brien, D. Long, J. N. Coleman, V. Nicolosi, *Nano Energy*, 2016, 28, 495-505 (b) Z. Peng, X. Liu, H. Meng, Z. Li, B. Li, Z. Liu, S. Liu, *ACS Appl. Mater. Interfaces*, 2017, 9, 4577-4586

[50] (a) M. Huang, F. Li, F. Dong, Y. X. Zhang, L. L. Zhang, *J. Mater. Chem. A*, 2015, 3, 21380-21423 (b) J. Cao, X. Li, Y. Wang, F. C. Walsh, J. H. Ouyang, D. Jia, Y. Zhou, *J. Power Source*s 2015, 293, 657-674

[51] (a) S. Gu, Z. Lou, L. Li, Z. Chen, X. Ma, G. Shen, *Nano Res.*, 2016, 9, 424-434 (b) K. Chi, Z. Zhang, Q. Lv, C. Xie, J. Xiao, F. Xiao, S. Wang, *ACS Appl. Mater. Interfaces*, 2017, 9, 6044-6053

[52] (a) C. H. Lai, D. Ashby, M. Moz, Y. Gogotsi, L. Pilon, B. Dunn, *Langmuir*, 2017, 33, 9407-9415 (b) L. Kong, C. Zhang, J. Wang, W. Qiao, L. Ling, D. Long, *ACS Nano*, 2015, 9, 11200-11208

[53] (a) W. Li, F. Gao, X. Wang, N. Zhang, M. Ma, *Angew. Chem., Int. Ed.*, 2016, 12, 9342-9347 (b) E. Feng, H. Peng, Z. Zhang, J. Lia, Z. Lei, *New J. Chem.*, 2017, 41, 9024-9032 (c) A. Khosrozadeh, M. A. Darabi, M. Xing, Q. Wang, *ACS Appl. Mater. Interfaces*, 2016, 8, 11379-11389

[54] (a) C. Yang, L. Zhang, N. Hu, Z. Yang, H. Wei, Y. Zhang, *J. Power Sources*, 2016, 302, 39-45 (b) Y. Zhou, X. Hu, Y. Shang, C. Hua, P. Song, X. Li, Y. Zhang, A. Cao, *RSC Adv.*, 2016, 6, 62062-62070 (c) C. Yang, L. Zhang, N. Hu, Z. Yang, H. Wei, Y. Wang, Y. Zhang, *Appl. Surf. Sci.* 2016, 387, 666-673

[55] (a) R. B. Ambade, S. B. Ambade, R. R. Salunkhe, V. Malgras, S. H. Jin, Y. Yamauchi,

S. H. Lee, *J. Mater. Chem. A*, 2016,4, 7406-7415 (b) Y. Li, G. Ren, Z. Zhang, C. Teng, Y. Wu, X. Lu, Y. Zhu, L. Jiang, *J. Mater. Chem. A*, 2016, 4, 17324-17332 (c) Z. S. Wu, Y. Zheng, S. Zheng, S. Wang, C. Sun, K. Parvez, T. Ikeda, X. Bao, K. Müllen, X. Feng, *Adv. Mater.* 2017, 10.1002/adma.201602960

[56] X. Xiao, X. Peng, H. Jin, T. Li, C. Zhang, B. Gao, B. Hu, K. Huo, J. Zhou, *Adv. Mater.* 2013, 25, 5091.

[57] B. Gao, X. Li, X. Guo, X. Zhang, X. Peng, L. Wang, J. Fu, P. K. Chu, K. Huo, *Adv. Mater. Interfaces* 2015, *2*, 1500211.

[58] (a) S. Mondal, U. Rana, S. Malik, *J. Phys. Chem. C*, 2017, 121, 7573-7583 (b) J. Li, W. Lu, Y. Yand, T. W. Chou, *J. Mater. Chem. A*, 2017, 5, 11271-11277 (c) N. Hu, L. Zhang, C. Yang, J. Zhao, Z. Yang, H. Wei, H. Liao, Z. Feng, A. Fisher, Y. Zhang, Z. J. Xu, Sci. Rep. 2016, 6, 19777 (d) L. Negre, B. Daffos, V. Turq, P. L. Taberna P. Simon, *Electrochim. Acta.* 2016, 206, 490-495

[59] K. Chi, Z. Zhang, J. Xi, Y. Huang, F. Xiao, S. Wang, Y. Liu, *ACS Appl. Mater. Interfaces* 2014, 6, 16312-16319.

[60] Y. Chen, L. Du, P. Yang, P. Sun, X. Yu, W. Mai, *J. Power Sources* 2015, 287, 68-74

[61] (a) H. Zhou, H. J. Zhai, G. Han, *J. Power Sources*, 2016, 323, 125-133 (b) T. Cheng, Y. Z. Zhang, J. D. Zhang, W. Y. Lai, W. Huang, *J. Mater. Chem. A*, 2016,4, 10493-10499 (c) S. Lehtimäki, M. Suominen, P. Damlin, S. Tuukkanen, C. Kvarnström, D. Lupo, *ACS Appl. Mater. Interfaces*, 2015, 7, 22137-22147 (d) I. Shown, A. Ganguly, L. C. Chen, K. H. Chen, *Energy Sci. Eng.* 2015, 3, 2-26

[62] Y. Liu, B. Weng, J. M. Razal, Q. Xu, C. Zhao, Y. Hou, S. Seyedin, R. Jalili, G. G. Wallace, J. Chen, *Sci. Rep.* 2015, 5, 17045.

[63] Z. Li, G. Ma, R. Ge, F. Qin, X. Dong, W. Meng, T. Liu, J. Tong, F. Jiang, Y. Zhou, K. Li, X. Min, K. Huo, Y. Zhou, *Angew. Chem. Int. Ed.* 2016, 55, 979-982.

[64] (a) J. Yu, J. Wu, H. Wang, A. Zhou, C. Huang, H. Bai, L. Li, *ACS Appl. Mater. Interfaces*, 2016, 8, 4724–4729 (b) J. Cao, T. Huang, R. Liu, X. Xi, D. Wu, *Electrochim. Acta*, 2017, 230, 265-270 (c) P. A. Shinde, N. R. Chodankar, V. C. Lokhande, A. M. Patil, T. Ji, J. H. Kim, C. D. Lokhande, *RSC Adv.*, 2016, 6, 113442-113451

[65] (a) A. Lamberti, M. Fontana, S. Bianco, E. Tresso, International J. Hydrogen Energy, 2016, 41, 11700-11708 (b) P. Pazhamalai, K. Krishnamoorthy, S. J. Kim, International J. Hydrogen Energy, 2016, 41, 14830-14835

[66] (a) Y. Wang, S. Wang, Y. Wu, Z. Zheng, K. Hong, B. Li, Y. Sun, *Electrochim. Acta*, 2017, 246, 1065-1074 (b) X. Yang, Z. Lin, J. Zheng, Y. Huang, B. Chen, Y. Mai, X. Feng, *Nanoscale*, 2016, 8, 8650-8657 (c) V. S. Kumbhar, Y. R. Lee, C. S. Ra, D. Tum, B. K. Min, J. J. Shim, *RSC Adv.*, 2017, 7, 16348-16359

[67] (a) H. Xia, D. D. Zhu, Z. T. Luo, Y. Yu, X. Q. Shi, G. L. Yuan, J. P. Xie, Sci. Rep. 2013, 3, 2978, (b) L. T. Le, M. H. Ervin, H. Qiu, B. E. Fuchs, W. Y. Lee, Electrochem. Commun. 2011, 13, 355.

[68] (a) N. R. Chodankar, D. P. Dubal, A. C. Lokhande, C. D. Lokhande, *J. Colloid and Interface Science* 2015, 460, 370-376, (b) S. K. Shinde, D. P. Dubal, G. S. Ghodake, D. Y. Kim, V. J. Fulari, *Nano-Structures & Nano-Objects* 2016, 6, 5-13.

[69] (a) N. R. Chodankar, D. P. Dubal, G. S. Gund, C. D. Lokhande, *Electrochim. Acta* 2015, 165, 338-347 (b) N. R. Chodankar, D. P. Dubal, G. S. Gund, C. D. Lokhande, *J. Energy Chem.* 2016, 25, 463-471.

[70] J. Chen, J. Xu, S. Zhou, N. Zhao, C. P. Wong, *J. Mater. Chem. A*, 2015, 3, 17385–17391

[71] K. Sheng, Y. Sun, C. Li, W. Yuan, G. Shi, *Sci. Rep.*, 2012, 2, 247.

[72] (a) R. K. Gupta, J. Candler, S. Palchoudhury, K. Ramasamy, B. K. Gupta, *Sci. Rep.* 2015, 5, 15265, (b) G. Zhu, Z. He, J. Chen, J. Zhao, X. Feng, Y. Ma, Q. Fan, L. Wang,

W. Huang, *Nanoscale*, 2014, 6, 1079-1085, (c) B. Liu, B. Liu, Q. Wang, X. Wang, Q. Xiang, D. Chen, G. Shen, *ACS Appl. Mater. Interfaces* 2013, 5, 10011-10017

[73] Y. Huang, J. Tao, W. Meng, M. Zhu, Y. Huang, Y. Fu, Y. Gao, C. Zhi, Nano Energy, 2015, 11, 518–525.

[74] W. Zhou, X. Liu, Y. Sang, Z. Zhao, K. Zhou, H. Liu, S. Chen, *ACS Appl. Mater. Interfaces* 2014, 6, 4578−4586.

[75] Q. Wang, X. Wang, B. Liu, G. Yu, X. Hou, D. Chen, G. Shen, *J. Mater. Chem. A*, 2013, 1, 2468–2473

[76] M. Shao, Z. Li, R. Zhang, F. Ning, M. Wei, D. G. Evans, X. Duan, *Small* 2015, 11, 3530–3538

[77] (a) W. Liu, C. Lu, H. Li, R. Y. Tay, L. Sun, X. Wang, W. L. Chow, X. Wang, B. K. Tay, Z. Chen, J. Yan, K. Feng, G. Lui, R. Tjandra, L. Rasenthiram, G. Chiu, A. Yu, *J. Mater. Chem. A*, 2016,4, 3754-3764 (b) Z. Liu, Z. S. Wu, S. Yang, R. Dong, X. Feng, K. Müllen, *Adv. Mater.* 2016, 28, 2217-2222

[78] J. Tao, W. Ma, N. Liu, X. Ren, Y. Shi, J. Su, Y. Gao, Nano-Micro Lett. 2015, 7, 276-281

[79] J. Li, X. Cheng, J. Sun, C. Brand, A. Shashurin, M. Reeves, M. Keidar, *J. Appl. Phys.* 2014, 115, 164301

[80] X. Zhang, Z. Lin, B. Chen, S. Sharma, C. Wong, W. Zhang, Y. Deng, *J. Mater. Chem. A*, 2013, 1, 5835-5839

[81] L. Yuan, X. Xiao, T. Ding, J. Zhong, X. Zhang, Y. Shen, B. Hu, Y. Huang, J. Zhou, Z. L. Wang, *Angew. Chem. Int. Ed.* 2012, 51, 4934-4938

[82] L. Zhang, P. Zhu, F. Zhou, W. Zeng, H. Su, G. Li, J. Gao, R. Sun, C. Wong, *ACS Nano*, 2016, *10*, 1273-1282

[83] K. H. Choi, J. T. Yoo, C. K. Lee, S. Y. Lee, *Energy Environ. Sci.*, 2016, 9, 2812-2821

[84] (a) M. Mao, J. Hu, H. Liu, *International J. Energy Res.* 2015, 39, 727-740, (b) S. Zhai,

H. E. Karahan, L. Wei, Q. Qian, A. T. Harris, A. I. Minett, S. Ramakrishna, A. K. Ng, Y. Chen, *Energy Storage Materials*, 2016, 3, 123-139. (c) Q. Xue, J. Sun, Y. Huang, M. Zhu, Z. Pei, H. Li, Y. Wang, N. Li, H. Zhang, C. Zhi, *small*, 2017, DOI: 10.1002/smll.201701827

[85] (a) K. Jost, D. Stenger, C. R. Perez, J. K. McDonough, K. Lian, Y. Gogotsi, G. Dion, *Energy Environ. Sci.*, 2013, 6, 2698-2705 (b) W. Y. Ko, Y. F. Chen, K. M. Lu, K. J. Lin, *Sci. Rep.* 2016, 6, 18887 (c) X. Yu, X. Su, K. Yan, H. Hu, M. Peng, X. Cai, D. Zou, Adv. Mater. Tech. 2016, 1, 1600009 (d) X. Li, J. Wang, Y. Zhao, F. Ge, S. Komarneni, Z. Cai, *ACS Appl. Mater. Interfaces*, 2016, 8, 25905–25914

[86] (a) A. M. Abdelkader, N. Karim, C. Vallés, S. Afroj, K. S Novoselov, S. G. Yeates, *2D Mater.*, 2017, 4, 035016 (b) Q. Lu, L. Liu, S. Yang, J. Liu, Q. Tian, W. Yao, Q. Xue, M. Li, W. Wu, *J. Power Sources* 2017, 361, 31-38 (c) N. Yu, H. Yin, W. Zhang, Y. Liu, Z. Tang, M. Q. Zhu, Adv. Energy. Mater. 2016, doi: 10.1002/aenm.201501458

[87] C. Zhou, J. Liu, *Nanotechnology*, 2014, 25, 035402.

[88] Y. Chen, X. Zhang, Z. Xie, *ACS Nano*, 2015, *9*, 8054–8063

[89] H. Y. Jin, Z. H. Peng, W. M. Tang, H. L. W. Chan, *RSC Adv.*, 2014, 4, 33022-33028

[90] W. Y. Ko, Y. F. Chen, K. M. Lu, K. J. Lin, *Sci. Rep.*, 2016, 6, 18887

[91] M. S. Javed, J. Chen, L. Chen, Y. Xi, C. Zhang, B. Wan, C. Hu, *J. Mater. Chem. A*, 2016, 4, 667-674

[92] Q. Liao, N. Li, S. Jin, G. Yang, C. Wang, *ACS Nano*, 2015, *9*, 5310-5317

[93] (a) Q. Wang, Y. Wu, T. Li, D. Zhang, M. Miao, A. Zhang, *J. Mater. Chem. A*, 2016,4, 3828-3834 (b) J. Sun, Y. Huang, C. Fu, Z. Wang, Y. Huang, M. Zhu, C. Zhi, H. Hu, *Nano Energy* 2016, 27, 230-237 (c) L. Gao, X. Li, X. Li, J. Cheng, B. Wang, Z. Wang, C. Li, *RSC Adv.*, 2016, 6, 57190-57198

[94] (a) C. Choi, H. J. Sim, G. M. Spinks, X. Lepró, R. H. Baughman, S. J. Kim, Adv. Energy

Mater. 2016, 6, 1502119 DOI: 10.1002/aenm.201502119 (b) Q. Wang, D. Zhang, Y. Wu, T. Li, A. Zhang, M. Miao, *Energy Tech.* 2017, 5, 1449-1456

[95] T. Huang, B. Zheng, L. Kou, K. Gopalsamy, Z. Xu, C. Gao, Y. Meng, Z. Wei, *RSC Adv.*, 2013, 3, 23957-23962

[96] L. Kou, T. Huang, B. Zheng, Y. Han, X. Zhao, K. Gopalsamy, H. Sun, C. Gao, *Nat. Commun.*, 2014, 5, 3754

[97] (a) B. Liu, D. Tan, X. Wang, D. Chen, G. Shen, *Small* 2013, 9, 1998-2004 (b) Q. Wang, X. Wang, J. Xu, X. Ouyang, X. Hou, D. Chen, R. Wang, G. Shen, *Nano Energy* 2014, 8, 44-51. (c) X. Dong, Z. Guo, Y. Song, M. Hou, J. Wang, Y. Wang, Y. Xia, *Adv. Funct. Mater.* 2014, 24, 3405-3412

[98] T. Chen, L. Dai, *Energy Storage Mater.*, 2016, 2, 21–26

[99] N. Liu, W. Ma, J. Tao, X. Zhang, J. Su, L. Li, C. Yang, Y. Gao, D. Golberg, Y. Bando, *Adv. Mater.* 2013, 25, 4925-4931

[100] Z. Yu, J. Thomas, *Adv. Mater.* 2014, 26, 4279-4285

[101] Y. Huang, H. Hu, Y. Huang, M. Zhu, W. Meng, C. Liu, Z. Pei, C. Hao, Z. Wang, C. Zhi, *ACS Nano* 2015, 9, 4766–4775

[102] V. T. Le, H. Kim, A. Ghosh, J. Kim, J. Chang, Q. A. Vu, D. T. Pham, J. H. Lee, S. W. Kim, Y. H. Lee, *ACS Nano 2013*, 7, 5940-5947

[103] (a) X. Cao, B. Zheng, W. Shi, J. Yang, Z. Fan, Z. Luo, X. Rui, B. Chen, Q. Yan, H. Zhang, *Adv. Mater.* 2015, 27, 4695-4701 (b) Y. J. Kang, H. Chung, M. S. Kim, W. Kim, *Appl. Surf. Sci.* 2015, 355, 160-165 (c) X. Peng, H. Liu, Q. Yin, J. Wu, P. Chen, G. Zhang, G. Liu, C. Wu, Y. Xie, *Nat. Commun.* 2016, 7, 11782

[104] (a) T. Gu, B. Wei, *ACS Appl. Mater. Interfaces*, 2016, 8, 25243-25250 (b) X. Fan, T. Chen, L. Dai, *RSC Adv.*, 2014, 4, 36996-37002 (c) E. A. Nagelli, L. Huang, A.Q.-Z. Dai, F. Du, L. Dai, *Part. Part. Syst. Charact.* 2017, https://doi.org/10.1002/ppsc.201700131

[105] Z. S. Zhang, T. Zhai, X. H. Lu, M. H. Yu, Y. X. Tong and K. C. Mai, J. Mater. Chem. A, 2013, 1, 505.

[106] (a) Z. Liu, Z. S. Wu, S. Yang, R. Dong, X. Feng, K. Müllen, Adv. Mater. 2016, 28, 2217-2222 (b) P. Yu, W. Fu, Q. Zeng, J. Lin, C. Yan, Z. Lai, B. Tang, K. Suenaga, H. Zhang, Z. Liu, *Adv. Mater.* 2017, DOI: 10.1002/adma.201701909

[107] Y. Gao, Y. S. Zhou, W. Xiong, L. J. Jiang, M. Mahjouri-samani, P. Thirugnanam, X. Huang, M. M. Wang, L. Jiang, Y. F. Lu, *APL Mater.* 2013, 1, 012101

[108] B. G. Choi, J. Hong, W. H. Hong, P. T. Hammond, H. S. Park, *ACS Nano* 2011, 5, 7205–7213

[109] H. Fei, C. Yang, H. Bao, G. Wang, *J. Power Sources* 2014, 266, 488-495

[110] W. Si, C. Yan, Y. Chen, S. Oswald, L. Hana, O. G. Schmidt, *Energy Environ. Sci.*, 2013, 6, 3218–3223

[111] X. Xiao, T. Li, P. Yang, Y. Gao, H. Jin, W. Ni, W. Zhan, X. Zhang, Y. Cao, J. Zhong, L. Gong, W. C. Yen, W. Mai, J. Chen, K. Huo, Y. L. Chueh, Z. L. Wang, J. Zhou, *ACS Nano*, 2012, 6, 9200-9206

[112] N. Kurra, M. K. Hota, H. N. Alshareef, *Nano Energy* 2015, 13, 500-508

[113] (a) Y. Xu, Z. Lin, X. Huang, Y. Liu, Y. Huang, X. Duan, *ACS Nano* 2013, 7, 4042-4049 (b) J. Cai, C. Lv, A. Watanabe, *J. Mater. Chem. A*, 2016, *4*, 1671-1679

[114] J. B. In, B. Hsi, J. H. Yoo, S. Hyun, C. Carraro, R. Maboudian, C. P. Grigoropoulos, *Carbon*, 2015, 83, 144-151

[115] Z. Peng, J. Lin, R. Ye, E. L. G. Samuel, J. M. Tour, *ACS Appl. Mater. Interfaces* 2015, 7, 3414-3419

[116] (a) S. Li, C. Zhao, K. Shu, C. Wang, Z. P. Guo, G. G. Wallace, H. K. Liu, Carbon, 2014, 79, 554-562, (b) B. Hsia, J. Marschewski, S. Wang, J. B. In, C. Carraro, D. Poulikakos, C. P. Grigoropoulos, R. Maboudian, *Nanotechnology* 2014, 25, 055401

[117] Y. S. Moon, D. Kim, G. Lee, S. Y. Hong, K. K. Kim, S. M. Park, J. S. Ha, *Carbon*, 2015, 81, 29-37

[118] J. Maeng, C. Meng, P. P. Irazoqui, *Biomed. Microdevices*, 2015, 17, 7

[119] T. Chen, L. Dai, *Energy Storage Materials*, 2016, 2, 21–26.

[120] H. Xu, X. Hu, Y. Sun, H. Yang, X. Liu, Y. Huang, *Nano Research,* 2015, 8(4) 1148–1158.

[121] X. Dong , Z. Guo , Y. Song , M. Hou , J. Wang , Y. Wang, Y. Xia, *Adv. Funct. Mater.* 2014, *24*, 3405–3412.

[122] W. Ma, S. Chen, S. Yang, W. Chen, Y. Cheng, Y. Guo, S. Peng, S. Ramakrishn, M. Zhu, *J. Power Sources*, 2016, 306, 481-488.

[123] S. Jiang, T. Shi, X. Zhan, H. Long, S. Xi, H. Hu, Z. Tang, *J. Power Sources* 2014, 272, 16-23.

[124] D. Zhao, C. Chen, Q. Zhang, W. Chen, S. Liu, Q. Wang, Y. Liu, J. Li, H. Yu, *Adv. Energy Mater.* 2017, 1700739-1700748.

[125] K. Wang, X. Zhang, C. Li, H. Zhang, X. Sun, N. Xu, Y. Ma, *J. Mater. Chem. A*, 2014, 2, 19726-19732.

[126] J. Yu, J. Wu, H. Wang, A. Zhou, C. Huang, H. Bai, L. Li, *ACS Appl. Mater. Interfaces*, 2016, 8, 4724–4729.

[127] P. Zhang, Z. Liu, Y. Liu, H. Fan, Y. Jiao, B. Chen, *Electrochim.. Acta* 2015, 184, 1–7.

[128] P. Wu, S. Cheng, M. Yao, L. Yang, Y. Zhu, P. Liu, O. Xing, J. Zhou, M. Wang, H. Luo, M. Liu, *Adv. Funct. Mater.* 2017, 1702160-1702169.

[129] X. Li, S. Ding, X. Xiao, J. Shao, J. Wei, H. Pang, Y. Yu, *J. Mater. Chem. A*, 2017, 5, 12774-12781

[130] J. Noh, C. Yoon, Y. Kim, J. Jang, *Carbon*, 2017, 116, 470-478.

[131] M. Yu, T. Zhai, X. Lu, X. Chen, S. Xie, W. Li, C. Liang, W. Zhao, L. Zhang, Y. Tong, J.

Power Sources, 2013, 239, 64-71.

[132] B. S. Shen, H. Wang, L. J. Wu, R. S. Guo, Q. Huang, X. B. Yan, *Chin. Chem. Lett.* 2016, 27, 1586-1591

[133] K. Ye, Z. Liu, C. Xu, N. Li, Y. Chen, Y. Su, Inorganic Chemistry Communications, 2013, 30, 1–4.

[134] M. S. Javed, S. Dai, M. Wang, D. Guo, L. Chen, X. Wang, C. Hu, Y. Xi, *J. Power Sources* 2015, 285, 63-69.

[135] C. Liu, S. Zhao, Y. Lu, Y. Chang, D. Xu, Q. Wang, Z. Dai, J. Bao, M. Han, *small* 2017, DOI: 10.1002/smll.201603494.

[136] P. Yang, Y. Li, Z. Lin, Y. Ding, S. Yue, C. P. Wong, X. Cai, S. Tan, W. Mai, *J. Mater. Chem. A*, 2014, 2, 595–599.

[137] Q. Liao, N. Li, S. Jin, G. Yang, C. Wang, *ACS nano* 2015, 9, 5310–5317.

[138] J. Zhao, J. Chen, S. Xu, M. Shao, D. Yan, M. Wei, D. G. Evans, X. Duan, *J. Mater. Chem. A*, 2013, 1, 8836–8843

[139] H. Y. Jin, Z. H. Peng, W. M. Tang, H. L. W. Chan, *RSC Adv*., 2014, 4, 33022–33028.

[140] Q. Wang, J. Xu, X. Wang, B. Liu, X. Hou, G. Yu, P. Wang, D. Chen, G. Shen, *ChemElectroChem* 2014, 1, 559 – 564.

[141] X. F. Lu, A. L. Wang, H. Xu, X. J. He, Y. X. Tong, G. R. Li, *J. Mater. Chem. A*, 2015, 3, 16560–16566 (301a)

[142] M. S. Javed, S. Dai, M. Wang, Y. Xi, Q. Lang, D. Guo, C. Hu, *Nanoscale*, 2015, 7, 13610–13618.

[143] G. Zhu, Z. He, J. Chen, J. Zhao, X. Feng, Y. Ma, Q. Fan, L. Wang, W. Huang, Nanoscale, 2014, 6, 1079–1085.

[144] T. Qin, S. Peng, J. Hao, Y. Wen, Z. Wang, X. Wang, D. He, J. Zhang, J. Hou, G. Cao, *Adv. Energy Mater.* 2017, 1700409-1700419.

[145] W. Y. Ko, Y. F. Chen, K. M. Lu, K. J. Lin, *Sci. Rep.* 2015, 6, 18887.

[146] K. Parvez, Z. Wu, R. Li, X. Liu, R. Graf, X. Feng, K. Müllen *, J. Am. Chem. Soc.*, 2014, 136, 6083−6091.

[147] X. Wang, A. Sumboja, W. L. Foo, C. Yan, K. Tsukagoshi, P. Lee, *RSC Adv*., 2013, 3, 15827–15833.

[148] Y. Gao, H. Jin, Q. Lin, X. Li, M. Tavakoli, S. Leung, W. Tang, L. Zhou, H. Chan, Z. Fan, *J. Mater. Chem. A*, 2015, 3, 10199–10204.

[149] J. Zhang, X. Zhao, Z. Huang, T. Xu, Q. Zhang, *Carbon* 2016, 107, 844-851

[150] B. Yao, L. Yuan, X. Xiao, J. Zhang, Y. Qi, J. Zhou, J. Zhou, B. Hub, W. Chen, *Nano Energy* 2013, 2, 1071–1078.

[151] S. Dai, W. Xu, Y. Xin, M. Wang, X. Gun, D. Guo, C. Hun, *Nano Energy* 2016, 19, 363–372.

[152] H. Lee, S. Hong, J. Kwon, Y. Suh, J. Lee, H. Moon, J. Yeo, S. Ko, *J. Mater. Chem. A,* 2015, 3, 8339–8345.

[153] J. Yun, D. Kim, G. Lee, J. Ha, *Carbon* 2014, 79, 156-164.

[154] Y. Kang, H. Chung, M. Kim, W. Kim, *Applied Surface Science* 2015, 355, 160–165.

[155] H. Hu, K. Zhang, S. Li, S. Jia, C. Ye, *J. Mater. Chem. A*, 2014, 2, 20916–20922.

[156] X. Xu, W. Shi, P. Li, S. Ye, C. Ye, H. Ye, T. Lu, A. Zheng, J. Zhu, L. Xu, M. Zhong, X. Cao, *Chem. Mater.*, 2017, 29, 6058-6065

[157] K. Zhang, H. Hu, W. Yao, C. Ye, *J. Mater. Chem. A*, 2015, 3, 617–623.

[158] X. Liu, T. Qian, N. Xu, J. Zhou, J. Guo, C. Yan, *Carbon* 2015, 92, 348-353.

[159] S. Liu, J. Xie, H. Li, Y. Wang, H. Yang, T. Zhu, S. Zhang, G. Cao, X. Zhao, *J. Mater. Chem. A*, 2014, 2, 18125–18131.

[160] C. Hao, F. Wen, J. Xiang, L. Wang, H. Hou, Z. Su, W. Hu, Z. Liu, *Adv. Funct. Mater.* 2014, *24*, 6700–6707.

[161] X. Cao, B. Zheng, W. Shi, J. Yang, Z. Fan, Z. Luo, X. Rui, B. Chen, Q. Yan, H. Zhang, *Adv. Mater.* 2015, *27*, 4695–4701.

[162] L. Li, J. Gong, C. Liu, Y. Tian, M. Han, Q. Wang, X. Hong, Q. Ding, W. Zhu, J. Bao, *ACS Omega*, 2017, 2, 1089-1096.

[163] G. Sun, J. An, C. Chua, H. Pang, J. Zhang, P. Chen, *Electrochemistry Communications* 2015, 51, 33–36.

[164] J. Xie, X. Sun, N. Zhang, K. Xu, M. Zhou, Y. Xie, *Nano Energy* 2013, 2, 65–74.

[165] Y. Chen, K. Cai, C. Liu, H. Song, X. Yang, *Adv. Energy Mater.* 2017, 1701247-1701258.

[166] X. Li, T. Zhao, Q. Chen, P. Li, K. Wang, M. Zhong, J. Wei, D. Wu, B. Weief, H. Zhu, *Phys. Chem. Chem. Phys.,* 2013, 15, 17752—17757.

[167] X. Fan, T. Chen, L. Dai, *RSC Adv*., 2014, 4, 36996–37002.

[168] R. Yuksel, Z. Sariob, A. Cirpan, P. Hiralal, H. Unalan, *ACS Appl. Mater. Interfaces* 2014, 6, 15434−15439.

[169] M. Sawangphruk, M. Suksomboon, K. Kongsupornsak, J. Khuntilo, P. Srimuk, Y. Sanguansak, P. Klunbud, P. Suktha, P. Chiochan, J. Mater. Chem. A, 2013, 1, 9630–9636

[170] B. Pandit, D. P. Dubal, B. R. Sankapal, *Electrochim. Acta* 2017, 242, 382-389.

[171] H. Niu, X. Yang, H. Jiang, D. Zhou, X. Li, T. Zhang, J. Liu, Q. Wang, F. Qu*, J. Mater. Chem. A*, 2015, 3, 24082–24094.

[172] Y. Shao, H. Wang, Q. Zhang, Y. Li, *NPG Asia Materials*, 2014, 6, 119

[173] (a) B. E. Francisco, C. M. Jones, S. H. Lee and C. R. Stoldt, *Appl. Phys. Lett.*, 2012, 100, 103902 (b) A. S. Ulihin, Y. G. Mateyshina and N. F. Uvarov, *Solid State Ionics*, 2013, 251, 62–65.

[174] (a) N. A. Choudhury, S. Sampath and A. K. Shukla, *Energy Environ. Sci.*, 2009, 2, 55-

67 (b) H. Gao, K. Lian, *RSC Adv.*, 2014, 4, 33091-33113, (c) C. Zhong, Y. Deng, W. Hu, J. Qiao, L. Zhang, J. Zhang, *Chem. Soc. Rev*., 2015,44, 7484-7539

[175] A. A. Łatoszynska, G. Z. Zukowska, I. A. Rutkowska, P. L. Taberna, P. Simon, P. J. Kulesza, W. Wieczorek, *J. Power Sources*, 2014, 274, 1147-1154

[176] (a) C. Meng, C. Liu, L. Chen, C. Hu and S. Fan, *Nano Lett.*, 2010, 10, 4025 (b) H. J. Yu, J. H. Wu, L. Q. Fan, Y. Z. Lin, K. Q. Xu, Z. Y. Tang, C. X. Cheng, S. Tang, J. M. Lin, M. L. Huang and Z. Lan, *J. Power Sources*, 2012, 198, 402 (257)

[177] J. Duay, E. Gillette, R. Liu and S. B. Lee, *Phys. Chem. Chem. Phys.*, 2012, 14, 3329.

[178] K. T. Lee, N. L. Wu, *J. Power Sources*, 2008, 179, 430.

[179] X. L. Hu, G. M. Hou, M. Q. Zhang, M. Z. Rong, W. H. Ruan, E. P. Giannelis, J. Mater. Chem., 2012, 22, 18961.

[180] P. Sivaraman, A. Thakur, R. K. Kushwaha, D. Ratna, A. B. Samui, *Electrochem. Solid-State Lett.*, 2006, 9, A435.

[181] C. W. Huang, C. A. Wu, S. S. Hou, P. L. Kuo, C. T. Hsieh, H. S. Teng, *Adv. Funct. Mater.*, 2012, 22, 4677.

[182] Y. S. Lee, S. H. Ju, J. H. Kim, S. S. Hwang, J. M. Choi, Y. K. Sun, H. Kim, B. Scrosati, D. W. Kim, *Electrochem. Commun.*, 2012, 17, 18.

[183] L. Q. Fan, J. Zhong, J. H. Wu, J. M. Lin, Y. F. Huang, *J. Mater. Chem. A*, 2014, 2, 9011-9014.

[184] G. M. Wang, X. H. Lu, Y. C. Ling, T. Zhai, H. Y. Wang, Y. X. Tong and Y. Li, ACS Nano, 2012, 6, 10296-10302.

[185] Y. J. Kang, H. Chung and W. Kim, Synth. Met., 2013, 166, 40-44.

[186] M. Sawangphruk, P. Srimuk, P. Chiochan, A. Krittayavathananon, S. Luanwuthi and J. Limtrakul, Carbon, 2013, 60, 109-116.

[187] X. Li, M. Zhou, J. Wang, F. Ge, Y. Zhao, S. Komarneni, Z. Cai, *J. Power Sources* 2017,

342, 762-771

[188] X. Jian, H. Yang, J. Li, E. Zhang, L. Cao, Z. Liang, *Electrochim. Acta* 2017, 228, 483-493

[189] T. Qian, N. Xu, J. Zhou, T. Yang, X. Liu, X. Shen, J. Liang, C. Yan, J. Mater. Chem. A, 2015, 3, 488–493.

[190] A. Virya, K. Lian, *Electrochem. Commun.*, 2017, 74, 33-37

[191] N. Li, T. Lv, Y. Yao, H. Li, K. Liu, T. Chen, *J. Mater. Chem. A*, 2017, 5, 3267

[192] Y. Yu, J. Zhong, W. Sun, R. Kumar, N. Koratkar, *Adv. Funct. Mater.* 27, 2017, 1606461

[193] Y. Xu, Z. Lin, X. Huang, Y. Wang, Y. Huang and X. Duan, *Adv. Mater.*, 2013, 25, 5779-5784.

[194] G. Huang, C. Hou, Y. Shao, B. Zhu, B. Jia, H. Wang, Q. Zhang and Y. Li, *Nano Energy*, 2015, 12, 26–32.

[195] G. M. Wang, H. Y. Wang, X. H. Lu, Y. C. Ling, M. H. Yu, T. Zhai, Y. X. Tong and Y. Li, *Adv. Mater.*, 2014, 26, 2676–2682.

[196] H. F. Ju, W. L. Song and L. Z. Fan, *J. Mater. Chem. A*, 2014, 2, 10895–10903.

[197] Q. Chen, X. M. Li, X. B. Zang, Y. C. Cao, Y. J. He, P. X. Li, K. L. Wang, J. Q. Wei, D. H. Wu and H. W. Zhu, *RSC Adv.*, 2014, 4, 36253-36256.

[198] H. Gao, K. Lian, *J. Power Sources*, 2011, 196, 8855

[199] H. Gao, K. Lian, *J. Mater. Chem.*, 2012, *22*, 21272

[200] H. Gao, K. Lian, *J. Electrochem. Soc.* 2013, 160, A505-A510

[201] (a) B. Scrosati, F. Croce, and L. Persi, *J. Electrochem. Soc.*, 2000, 147, 1718, (b) J. A. Kerres, *Fuel Cells*, 2005, 5, 230 (c) Y. Jin, S. Qiao, L. Zhang, Z. P. Xu, S. Smart, J. C. D. d. Costa, and G. Q. Lu, *J. Power Sources*, 2008, 185, 664

[202] K. Lian, Q. Tian, *Electrochem. Commun.* 2010, 12, 517-519

[203] (a) W. Li, T. Li, X. Ma, Y. Li, L. An, Z. Zhang, *RSC Adv.*, 2016, 6, 12491-12496 (b) H.

Gao, A. Virya, K. Lian, *J. Mater. Chem. A,* 2015, 3, 21511-21517

[204] K. M. Kim, J. H. Nam, Y. G. Lee, W. I. Cho, J. M. Ko, *Curr. Appl. Phys.*, 2013, 13, 1702-1706.

[205] D. Z. Chen, J. Yu, W. Lu, Y. Zhao, Y. Yan, T. W. Chou, *Electrochim. Acta* 2017, 233, 181-189

[206] (a) X. H. Lu, G. M. Wang, T. Zhai, M. H. Yu, S. L. Xie, Y. C. Ling, C. L. Liang, Y. X. Tong, Y. Li, *Nano Lett.*, 2012, 12, 5376, (b) C. C. Yang, S. J. Lin, *J. Appl. Electrochem.*, 2003, 33, 777.

[207] (a) J. Qiao, J. Fu, R. Lin, J. Ma, J. Liu, Polymer 2010, 51, 4850-4859 (b) C. C. Yang, S. J. Lin, G. M. Wu, *Mater. Chem. Phys.* 2005, 92, 251-255, (c) J. M. Yang, S. A. Wang, *J. Membr. Sci.* 2015, 477, 49-57.

[208] I. K. Moon, S. Yoon, J. Oh, *Chem. Eur. J.* 2017, 23, 597-604

[209] C. C. Yang, S. T. Hsu, W. C. Chien, *J. Power Sources*, 2005, 152, 303

[210] H. Zhang, C. Lu, C. Chen, L. Xie, P. Zhou, Q. Kong, *ChemElectroChem* 2017, 10.1002/celc.201700253

[211] A. Lewandowski, M. Zajder, E. Frackowiak, F. Beguin, *Electrochim. Acta*, 2001, 46, 2777

[212] H. Gao, K. Lian, *J. Electrochem. Soc.*, 2013, 160, A505-A510.

[213] Y. F. Huang, P. F. Wu, M. Q. Zhang, W. H. Ruan, E. P. Giannelis, *Electrochim. Acta*, 2014, 132, 103-111.

[214] N. Vassal, E. Salmon and J. F. Fauvarque, *Electrochim. Acta*, 2000, 45, 1527.

[215] D. Kalpana, N. G. Renganathan and S. Pitchumani, J. Power Sources, 2006, 157, 621.

[216] (a) C. Iwakura, H. Wada, S. Nohara, N. Furukawa, H. Inoue, M. Morita, *Electrochem. Solid-State Lett.*, 2003, 6, A37 (b) H. Wada, S. Nohara, N. Furukawa, H. Inoue, N. Sugoh, H. Iwasaki, M. Morita, C. Iwakura, *Electrochim. Acta*, 2004, 49, 4871.

[217] H. Gao, J. Li, K. Lian, *RSC Adv.*, 2014, 4, 21332–21339

[218] J. Li, K. Lian, *Polymer* 2016, 99, 2016, 140-146

[219] C. W. Huang, C. A. Wu, S. S. Hou, P. L. Kuo, C. T. Hsieh, H. S. Teng, *Adv. Funct. Mater.*, 2012, 22, 4677-4685.

[220] Y. N. Sudhakar, M. Selvakumar, D. K. Bhat, *Ionics*, 2013, 19, 277-285.

[221] C. Ramasamy, J. P. del Vel, M. Anderson, *J. Solid State Electrochem.*, 2014, 18, 2217–2223.

[222] M. Schroeder, P. Isken, M. Winter, S. Passerini, A. Lex-Balducci, A. Balducci, *J. Electrochem. Soc.*, 2013, 160, A1753-A1758.

[223] P. M. DiCarmine, T. B. Schon, T. M. McCormick, P. P. Klein, D. S. Seferos, *J. Phys. Chem. C*, 2014, 118, 8295-8307.

[224] C. W. Huang, C. A. Wu, S. S. Hou, P. L. Kuo, C. T. Hsieh, H. Teng, *Adv. Funct. Mater.* 2012, 22, 4677-4685

[225] J. Rodrıguez, E. Navarrete, E. A. Dalchiele, L. Sanchez, J. R. Ramos-Barrado, F. Martın, *J. Power Sources*, 2013, 237, 270–276.

[226] M. F. Hsueh, C. W. Huang, C. A. Wu, P. L. Kuo, H. Teng, *J. Phys. Chem. C*, 2013, 117, 16751-16758.

[227] Y. D. Chiou, D. S. Tsai, H. H. Lam, C. H. Chang, K. Y. Lee, Y. S. Huang, Nanoscale, 2013, 5, 8122-8129

[228] R. Yuksel, Z. Sarioba, A. Cirpan, P. Hiralal, H. E. Unalan, *ACS Appl. Mater. Interfaces*, 2014, 6, 15434–15439.

[229] C. Ramasamy, J. Palma and M. Anderson, *J. Solid State Electrochem.*, 2014, 18, 2903-2911.

[230] S. N. Syahidah, S. R. Majid, *Electrochim. Acta*, 2013, 112, 678-685

[231] A. Jain and S. K. Tripathi, *Ionics*, 2013, 19, 549-557

[232] B. Anothumakkool, Arun Torris A. T., S. Veeliyath, V. Vijayakumar, M. V. Badiger, S. Kurungot, *ACS Appl. Mater. Interfaces* 2016, 8, 1233-1241

[233] V. Vijayakumar, B. Anothumakkool, Arun Torris A. T., S. B. Nair, M. V. Badiger, S. Kurungot, *J. Mater. Chem. A*, 2017, 5, 8461-8476

[224] (a) Y. Lim, J. Yoon, J. Yun, D. Kim, S. Y. Hong, S. J. Lee, G. Zi, J. S. Ha, ACS Nano, 2014, 8, 11639-11650 (b) S. Wang, B. Hsia, C. Carraro, R. Maboudian, *J. Mater. Chem. A*, 2014, 2, 7997-8002.

[235] (a) G. P. Pandey and S. A. Hashmi, *J. Mater. Chem. A*, 2013, 1, 3372-3378, (b) M. Suleman, Y. Kumar and S. A. Hashmi, *J. Phys. Chem. B*, 2013, 117, 7436-7443

[236] C. W. Liew, S. Ramesh and A. K. Arof, *Int. J. Hydrogen Energy*, 2014, 39, 2953-2963.

[237] S. Ketabi, K. Lian, *Electrochim. Acta*, 2013, 103, 174-178.

[238] P. Tamilarasan, S. Ramaprabhu, *Energy* 2013, 51, 374-381.

[239] X. Zhang, L. Wang, J. Peng, P. Cao, X. Cai, J. Li, M. Zhai, *Adv. Mater. Interfaces* 2015, *2*, 1500267

[240] (a) Y. J. Kang, S. J. Chun, S. S. Lee, B. Y. Kim, J. H. Kim, H. Chung, S. Y. Lee, W. Kim, *ACS Nano* 2012, 6, 6400–6406, (b) X. Yang, F. Zhang, L. Zhang, T. Zhang, Y. Huang, Y. Chen, *Adv. Funct. Mater.* 2013, *23*, 3353-3360

[241] A. Revzin, R. J. Russell, V. K. Yadavalli, W. G. Koh, C. Deister, D. D. Hile, M. B. Mellott, M. V. Pishko, *Langmuir* 2001, 17, 5440-5447

[242] D. Kim, G. Lee, D. Kim, J. S. Ha, *ACS Appl. Mater. Interfaces* 2015, 7, 4608-4615

[243] X. Zhong, J. Tang, L. Cao, W. Kong, Z. Sun, H. Cheng, Z. Lu, H. Pan, B. Xu, *Electrochim. Acta* 2017, 244, 112-118

[244] X. Liu, B. Wu, N. Brandon, Q. Wang, *Energy Technol.* 2017, 5, 220-224

[245] G. P. Pandey, A. C. Rastogi, C. R. Westgate, *J. Power Sources*, 2014, 245, 857–865.

[246] S. Ketabi, B. Decker, K. Lian, *Sol. State Ionics* 2016, 298, 73-79

[247] Y.Gao, Y. S. Zhou,M. Qian,H.M. Li, J. Redepenning, L. S. Fan, X. N. He, W. Xiong, X. Huang, M. Majhouri-Samani, L. Jiang, Y. F. Lu, *RSC Adv.*, 2013, 3, 20613–20618

[248] (a) N. R. Chodankar, D. P. Dubal, A. C. Lokhande, A. M. Patil, J. H. Kim, C. D. Lokhande, *Sci. Rep.* 2016, 6, 39205. (b) E. Frackowiak, K. Fic, M. Meller, G. Lota, *ChemSusChem* 2012, 5, 1181-1185. (c) E. Frackowiak, M. Meller, J. Menzel, D. Gastol, K. Fic, *Faraday Discuss.*, 2014, 172, 179-198. (d) B. Akinwolemiwa, C. Peng, G. Z. Chena, *J. Electrochem. Soc.* 2015, 162, A5054-A5059

[249] (a) G. Lota, K. Fic and E. Frackowiak, *Electrochem. Commun.*, 2011, 12, 38-41 (b) K. Fic, G. Lota, M. Meller and E. Frackowiak, *Energy Environ. Sci.*, 2012, 5, 5842-5850

[250] (a) H. Yu, J. Wu, L. Fan, K. Xu, X. Zhong, Y. Lin, J. Lin, *Electrochim. Acta* 2011, 56, 6881-6886. (b) S. T. Senthilkumar, R. Kalai Selvan, Y. S. Lee, J. S. Melo, *J. Mater. Chem. A*, 2013, 1, 1086–1095.

[251] G. Ma, J. Li, K. Sun, H. Peng, J. Mu, Z. Lei, *J. Power Sources* 2014, 256, 281-287

[252] (a) K. Sun, E. Feng, H. Peng, G. Ma, Y. Wu, H. Wang, Z. Lei, *Electrochim. Acta* 2015, 158, 361-367, (b) S. T. Senthilkumar, R. K. Selvan, J. S. Melo and C. Sanjeeviraja, ACS Appl. Mater. Interfaces, 2013, 5, 10541–10550

[253] S. T. Senthilkumar, R. K. Selvan, N. Ponpandian, J. S. Melo, RSC Adv., 2012, 2, 8937–8940.

[254] G. F. Ma, E. K. Feng, K. J. Sun, H. Peng, J. J. Li and Z. Q. Lei, Electrochim. Acta, 2014, 135, 461–466

[255] F. D. Yu, M. L. Huang, J. H. Wu, Z. Y. Qiu, L. Q. Fan, J. M. Lin and Y. B. Lin, J. Appl. Polym. Sci., 2014, 131, 39784.

[256] Y. Tian, R. Xue, X. Zhou, Z. Liu, L. Huang, *Electrochim. Acta* 2015, 152, 135-139

[257] S. Roldán, Z. González, C. Blanco, M. Granda, R. Menéndez, R. Santamaría, *Electrochim. Acta* 2011, 56, 3401-3405.

[258] E. Feng, G. Ma, K. Sun, F. Ran, H. Peng, Z. Lei, *New J. Chem.,* 2017, 41, 1986-1992

[259] E. Feng, G. Ma, K. Sun, Q. Yang, H. Peng, Z. Lei, *RSC Adv.*, 2016, 6, 75896-75904

[260] (a) D. P. Dubal, J. Suarez-Guevara, D. Tonti, E. Enciso, P. Gomez-Romero, *J. Mater. Chem. A*, 2015, 3, 23483-23492, (b) D. P. Dubal, B. Nagar, J. Suarez-Guevara, D. Tonti, E. Enciso, P. Palomino, P. Gomez-Romero, *Materials Today Energy* 2017, 5, 58-65

[261] S. Pan, J. Deng, G. Guan, Y. Zhang, P. Chen, J. Ren, H. Peng, *J. Mater. Chem. A*, 2015, 3, 6286-6290

[262] M. Kim, J. Yoo, J. Kim, *Chem. Eng. J.* 2017, 324, 93-103

[263] G. K. Veerasubramani, K. Krishnamoorthy, P. Pazhamalai, S. J. Kim, *Carbon*, 2016, 105, 638-648.

[264] H. Zhang, J. Li, C. Gu, M. Yao, B. Yang, P. Lu, Y. Ma, *J. Power Sources* 2016, 332, 413-419

[265] J. Zhou, J. Cai, S. Cai, X. Zhou and A. N. Mansour, *J. Power Sources*, 2011, 196, 10479-10483

[266] D. Kim, G. Lee, D. Kim, J. Yun, S. S. Lee, J. S. Ha, *Nanoscale*, 2016, 8, 15611-15620

[267] H. S. Jang, C. J. Raj, W. G. Lee, B. C. Kim, K. H. Yu, *RSC Adv.*, 2016, 6, 75376-75383

[268] J. K. Lee, Y. J. Lee, W. S. Chae, Y. M. Sung, *J. Electroceram.* 2006, *17*, 941.

[269] J. Reiter, J. Vondrak, J. Michalek, Z. Micka, *Electrochim. Acta* 2006, *52*, 1398

[270] X. Liu, D. Wu, H. Wang, Q. Wang, *Adv. Mater.* 2014, *26*, 4370

[271] G. P. Pandey, S. A. Hashmi, Y. Kumar, *Energy Fuels* 2010, *24*, 6644

[272] D. Kumar, S. A. Hashmi, *Solid State Ionics* 2010, 181, 416-423

[273] Sellam, S. A. Hashmi, *J. Solid State Electrochem* 2014, 18, 465-475

[274] S. A. Hashmi, A. Kumar, S. K. Tripathi, *European Polymer J.* 2005, 41, 1373-1379

[275] T. Chen, H. Peng, M. Durstock, L. Dai, *Sci. Rep.* 2014, 4, 3612

[276] F. Miao, C. Shao, X. Li, K. Wang, Y. Liu, *J. Mater. Chem. A*, 2016, 4, 4180-4187.

[277] B. Hsia, J. Marschewski, S. Wang, J. B. In, C. Carraro, D. Poulikakos, C. P. Grigoropoulos, R. Maboudian, *Nanotechnology* 2014, 25, 55401.

[278] M. F. El-Kady, V. Strong, S. Dubin, R. B. Kaner, Science, 2012, *335*, 1326.

[279] Y. Xu, Z. Lin, X. Huang, Y. Liu, Y. Huang, X. Duan, *ACS Nano*, 2013, 7, 4042-4049

[280] K. Gao, Z. Shao, J. Li, X. Wang, X. Peng, W. Wang, F. Wang, *J. Mater. Chem. A*, 2013, 1, 63-67

[281] (a) J. Sun, C. Wu, X. Sun, H. Hu, C. Zhi, L. Hou, C. Yuan, *J. Mater. Chem. A*, 2017, 5, 9443–9464 (b) Y. Zhang, L. Li, H. Su, W. Huang, X. Dong, *J. Mater. Chem. A*, 2015, 3, 43-59 (c) K. Wang, H. Wu, Y. Meng, Z. Wei, *small* 2014, 10, 14-31

[282] (a) Y. Zhong, X. Xia, F. Shi, J. Zhan, J. Tu, H. J. Fan, *Adv. Sci.* 2016, 3, 1500286 (b) X. Rui, H. Tan, Q. Yan, *Nanoscale*, 2014, 6, 9889-9924, (c) M. S. Balogun, W. Qiu, W. Wang, P. Fang, X. Lu, Y. Tong, *J. Mater. Chem. A*, 2015, 3, 1364-1387 (d) J. Zhu, S. Tang, J. Wu, X. Shi, B. Zhu, X. Meng, *Adv. Energy Mater.* 7, 2017 DOI: 10.1002/aenm.201601234

[283] (a) Y. Shi, L. Peng, Y. Ding, Y. Zhao, G. Yu, *Chem. Soc. Rev.,* 2015, 44, 6684-6696, (b) F. Wolfart, B. M. Hryniewicz, M. S. Góes, C. M. Corrêa, R. Torresi, M. A. O. S. Minadeo, S. I. Córdoba de Torresi, R. D. Oliveira, L. F. Marchesi, M. Vidotti, *J. Solid State Electrochem.* 2017, 21, 2489–2515 (c) R. Holze, Y. P. Wu, *Electrochim. Acta* 2014, 122, 93-107 (d) A. Eftekhari, L. Li, Y. Yang, *J. Power Sources* 2017, 347, 86-107

[284] A. Ferris, S. Garbarino, D. Guay, D. Pech, *Adv. Mater.* 2015, 27, 6625-6629

[285] T. M. Dinha, A. Achour, S. Vizireanu, G. Dinescu, L. Nistor, K. Armstrong, D. Guay, D. Pech, *Nano Energy* 2014, 10, 288-294

[286] J. Zhang, X. Zhao, Z. Huang, T. Xu, Q. Zhang, *Carbon* 2016, *107*, 844-851

[287] P. Shi, L. Li, L. Hua, Q. Qian, P. Wang, J. Zhou, G. Sun, W. Huang, *ACS Nano* 2017,

11, 444-452.

[288] W. Ma, S. Chen, S. Yang, W. Chen, Y. Cheng, Y. Guo, S. Peng, S. Ramakrishna, M. Zhu, *J. Power Sources* 2016, 306, 481-488

[289] S. Yang, X. Song, P. Zhang, L. Gao, *J. Mater. Chem. A*, 2015, 3, 6136-6145

[290] (a) B. Pandit, D. P. Dubal, P. Gómez-Romero, B. B. Kale, B. R. Sankapal, *Sci. Rep.*, 2017, 7, 43430 (b) B. Pandit, D. P. Dubal, B. R. Sankapal, *Electrochim. Acta* 2017, 242, 382-389

[291] D. Kim, J. Yun, G. Lee, J. S. Ha, *Nanoscale* 2014, 6, 12034-12041

[292] Y. Qian, R. Liu, Q. Wang, J. Xu, D. Chen, G. Shen, *J. Mater. Chem. A*, 2014, 2, 10917-10922

[293] Y. Zheng, Z. Lin, W. Chen, B. Liang, H. Du, R. Yang, X. He, Z. Tang, X. Gui, *J. Mater. Chem. A*, 2017, 5, 5886-5894

[294] B. D. Boruah, A. Misra, *J. Mater. Chem. A*, 2016, 4, 17552-17559

[295] H. Niu, X. Yang, H. Jiang, D. Zhou, X. Li, T. Zhang, J. Liu, Q. Wang, F. Qu, *J. Mater. Chem. A*, 2015, *3*, 24082-24094

[296] W. Cai, T. Lai, W. Dai, J. Ye, *J. Power Sources* 2014, 255, 170-178

[297] (a) D. Choi, G. E. Blomgren and P. N. Kumta, *Adv. Mater.*, 2006, 18, 1178-1182 (b) P. Pande, P. G. Rasmussen, L. T. Thompson, J. Power Sources, 2012, 207, 212-215.

[298] X. Xiao, X. Peng, H. Jin, T. Li, C. Zhang, B. Gao, B. Hu, K. Huo, J. Zhou, *Adv. Mater.* 2013, *25*, 5091-5097

[299] G. Ma, Z. Wang, B. Gao, T. Ding, Q. Zhong, X. Peng, J. Su, B. Hu, L. Yuan, P. K. Chu, J. Zhou, K. Huo, *J. Mater. Chem. A*, 2015, 3, 14617-14624

[300] X. Lu, G. Wang, T. Zhai, M. Yu, S. Xie, Y. Ling, C. Liang, Y. Tong, Y. Li, *Nano Lett.* 2012, 12, 5376-5381

[301] M. S. Javed, S. Dai, M. Wang, Y. Xi, Q. Lang, D. Guo, C. Hu, *Nanoscale*, 2015, 7,

13610-13618

[302] (a) X. Li, A. M. Elshahawy, C. Guan, J. Wang, *small*, 2017, DOI: 10.1002/smll.201701530 (b) M. C. Liu, Y. M. Hu, W. Y. An, Y. X. Hu, L. Y. Niu, L. B. Kong, L. Kang, *Electrochim. Acta.* 2017,232, 387-395. (c) C. Yang, L. Dong, Z. Chen, H. Lu, *J. Phys. Chem. C*, 2014, 118, 18884-18891.

[303] (a) R. Soni, B. Anothumakkool, S. Kurungot, ChemElectroChem, 2016, 3, 1329-1336 (b) C. Yang, L. Zhang, N. Hu, Z. Yang, H. Wei, Z. J. Xu, Y. Wang, Y. Zhang, Appl. Surf. Sci. 2016, 379, 206-212 (c) J. M. DArcy, M. F. El-Kady, P. P. Khine, L. Zhang, S. H. Lee, N. R. Davis, D. S. Liu, M. T. Yeung, S. Y. Kim, C. L. Turner, A. T. Lech, P. T. Hammond, R. B. Kaner, *ACS Nano*, 2014, 8, 1500-1510.

[304] F. Xiao, S. Yang, Z. Zhang, H. Liu, J. Xiao, L. Wan, J. Luo, S. Wang, Y. Liu, Sci. Rep. 2015, 5, 9359.

[305] L. Yuan, B. Yao, B. Hu, K. Huo, W. Chen, J. Zhou, *Energy Environ. Sci.*, 2013, 6, 470-476

[306] C. Yu, P. Ma, X. Zhou, A. Wang, T. Qian, S. Wu, Q. Chen, *ACS Appl. Mater. Interfaces* 2014, 6, 17937-17943

[307] R. Liu, L. Ma, S. Huang, J. Mei, J. Xu, G. Yuan, *New J. Chem.*, 2017, 41, 857-864

[308] (a) R. Dong, M. Pfeffermann, H. Liang, Z. Zheng, X. Zhu, J. Zhang and X. Feng, *Angew. Chem., Int. Ed.*, 2015, 54, 12058-12063 (b) M. Chhowalla, H. S. Shin, G. Eda, L. J. Li, K. P. Loh, H. Zhang, *Nat. Chem.*, 2013, 5, 263-275. (c) S. Liu, F. Wang, R. Dong, T. Zhang, J. Zhang, X. Zhuang, Y. Mai and X. Feng, *Adv. Mater.*, 2016, 28, 8365-8370. (d) P. Xiong, J. Zhu, L. Zhang and X. Wang, *Nanoscale Horiz.*, 2016, 1, 340-374.

[309] (a) B. Anasori, M. R. Lukatskaya, Y. Gogotsi, *Nat. Rev. Mater.* 2017, 2, 16098 (b) M. Naguib, M. Kurtoglu, V. Presser, J. Lu, J. Niu, M. Heon, L. Hultman, Y. Gogotsi, M. W.

Barsoum, *Adv. Mater.*, 2011, 23, 4248–4253 (c) V. M. H. Ng, H. Huang, K. Zhou, P. S. Lee, W. Que, J. Z. Xu, L. B. Kong, *J. Mater. Chem. A*, 2017, 5, 3039-3068

[310] (a) B. Anasori, Y. Xie, M. Beidaghi, J. Lu, B. C. Hosler, L. Hultman, P. R. C. Kent, Y. Gogotsi, M. W. Barsoum, *ACS Nano* 2015, 9, 9507-9516. (b) J. C. Lei, X. Zhang, Z. Zhou, *Front. Phys.* 2015, 10, 107303

[311] (a) F. Shahzad, M. Alhabeb, C. B. Hatter, B. Anasori, S. M. Hong, C. M. Koo, Y. Gogotsi, *Science* 2016, 353, 1137-1140 (b) A. Lipatov, M. Alhabeb, M. R. Lukatskaya, A. Boson, Y. Gogotsi, A. Sinitskii, *Adv. Electron. Mater.* 2016, 2, 1600255

[312] M. R. Lukatskaya, O. Mashtalir, C. E. Ren, Y. Dall Agnese, P. Rozier, P. L. Taberna, M. Naguib, P. Simon, M. W. Barsoum, Y. Gogotsi, *Science*, 2013, 341, 1502-1505

[313] M. Ghidiu, M. R. Lukatskaya, M. Q. Zhao, Y. Gogotsi, M. W. Barsoum, *Nature*, 2014, 516, 78-81

[314] C. Zhang, B. Anasori, A. Seral-Ascaso, S. H. Park, N. McEvoy, A. Shmeliov, G. S. Duesberg, J. N. Coleman, Y. Gogotsi, V. Nicolosi, *Adv. Mater.* 2017, DOI: 10.1002/adma.201702678

[315] M. Zhu, Y. Huang, Q. Deng, J. Zhou, Z. Pei, Q. Xue, Y. Huang, Z. Wang, H. Li, Q. Huang, C. Zhi, *Adv. Energy Mater.* 2016, 6, DOI: 10.1002/aenm.201600969

[316] H. Li, Y. Hou, F. Wang, M. R. Lohe, X. Zhuang, L. Niu, X. Feng, *Adv. Energy Mater*. 2017, DOI: 10.1002/aenm.201601847

[317] (a) J. Suarez-Guevara, V. Ruiz, P. Gomez-Romero, *J. Mater. Chem. A*, 2014, 2, 1014–1021 (b) J. Suarez-Guevara, V. Ruiz, P. Gomez-Romero, *Phys. Chem. Chem. Phys*., 2014, 16, 20411-20414.

[318] (a) A. K. Cuentas-Gallegos, M. Lira-Cantú, N. Casañ-Pastor, P. Gómez-Romero, *Adv. Fun. Mater.* 2005, 15, 1125-1133 (b) Y. Ji, L. Huang, J. Hu, C. Streb, Y. F. Song, *Energy Environ. Sci.*, 2015, 8, 776-789

[319] (a) M. Ammam, *J. Mater. Chem. A* 2013, 1, 6291-6312 (c) M. Genovese, K. Lian, *Electrochem. Commun.* 2014, 43, 60–62. (d) T. Akter, K. W. Hu, K. Lian, *Electrochim. Acta* 2011, 56, 4966–4971.

[320] (a) D. P. Dubal, B. Ballesteros, A. A. Mohite, P. Gomez-Romero, *ChemSusChem* 2017, 10, 731-737 (b) D. P. Dubal, N. R. Chodankar, A. Vinu, D. H. Kim, P. Gomez-Romero, *ChemSusChem* 2017, 10, 2742-2750 (c) V. Ruiz, J. Suarez-Guevara, P. Gomez-Romero, *Electrochem. Commun.* 2012, 24, 35–38

[321] (a) M. Genovese and K. Lian, *J. Mater. Chem. A*, 2017, 5, 3939-3947 (b) M. Genovese, K. Lian, *Curr. Opin. Solid State Mater. Sci.* 2015, 19, 126-137. (c) H. Y. Chen, R. Al-Oweini, J. Friedl, C. Y. Lee, L. Li, U. Kortz, U. Stimming, M. Srinivasan, *Nanoscale*, 2015, 7, 7934–7941

[322] Y. Chen, M. Han, Y. Tang, J. Bao, S. Li, Y. Lan, Z. Dai, *Chem. Commun.*, 2015, 51, 12377-12380

[323] V. Prabhakaran, B. L. Mehdi, J. J. Ditto, M. H. Engelhard, B. Wang, K. Don D. Gunaratne, D. C. Johnson, N. D. Browning, G. E. Johnson, J. Laskin, *Nat. Commun.* 2016, 7, 11399

[324] (a) R. R Salunkhe, Y. V. Kaneti, J. Kim, J. H. Kim, Y. Yamauchi, *Acc. Chem. Res.* 2016, 49, 2796-2806 (b) R. R Salunkhe, Y. V. Kaneti, Y. Yamauchi, *ACS Nano*, 2017, 11, 5293-5308. (c) W. Xuan, C. Zhu, Y. Liu and Y. Cui, *Chem. Soc. Rev.*, 2012, 41, 1677-1695

[325] (a) O. M. Yaghi, H. Li, *J. Am. Chem. Soc.*, 1995, 117, 10401-10402; (b) C. K. Brozeka, M. Dinca, *Chem. Soc. Rev.*, 2014, 43, 5456-5467; (c) N. Campagnol, T. R. C. Van Assche, M. Li, L. Stappers, M. Dinca, J. F. M. Denayer, K. Binnemans, D. E. DeVose, J. Fransaer, *J. Mater. Chem. A*, 2016, 4, 3914-3925.

[326] A. Mahmood, W. Guo, H. Tabassum and R. Zou, *Adv. Energy Mater.*, 2016, 6, DOI:

10.1002/aenm.201600423.

[327] (a) D. Y. Lee, S. J. Yoon, N. K. Shresth, S. H. Lee, H. Ahn, S. H. Han, *Microporous Mesoporous Mater.*, 2012, 153, 163-165. (b) R. Dıaz, M. G. Orcajo, J. A. Botas, G. Calleja, J. Palma, *Mater. Lett.*, 2012, 68, 126-128.

[328] A. Basu, K. Roy, N. Sharma, S. Nandi, R. Vaidhyanathan, S. Rane, C. Rode, S. Ogale, *ACS Appl. Mater. Interfaces* 2016, 8, 31841-31848

[329] F. Yu, T. Wang, Z. Wen, H. Wang, *J. Power Sources* 2017, 364, 9-15

[330] D. Fu, H. Zhou, X. M. Zhang, G. Han, Y. Chang, H. Li, *ChemistrySelect* 2016, 2, 285-289

[331] L. Wang, X. Feng, L. Ren, Q. Piao, J. Zhong, Y. Wang, H. Li, Y. Chen, B. Wang, *J. Am. Chem. Soc.*, 2015, 137, 4920-4923

[332] Y. Zhang, B. Lin, Y. Sun, P. Han, J. Wang, X. Ding, X. Zhang, H. Yang, *Electrochim. Acta* 2016, 188, 490-498

[333] L. Sun, M. G. Campbell, M. Dinca, *Angew. Chem. Int. Ed.* 2016, 55, 3566-3579

[334] D. Sheberla, J. C. Bachman, J. S. Elias, C. J. Sun, Y. Shao-Horn, M. Dinca, *Nat. Mater.* 2017, 16, 220-224

[335] W. H. Li, K. Ding, H. R. Tian, M. S. Yao, B. Nath, W. H. Deng, Y. Wang, G. Xu, *Adv. Funct. Mater.* 2017, DOI: 10.1002/adfm.201702067

[336] L. Li, Y. Yu, G. J. Ye, Q. Ge, X. Ou, H. Wu, D. Feng, X. H. Chen, Y. Zhang, *Nat. Nanotechnol.*, 2014, 9, 372–377.

[337] M. Köpf, N. Eckstein, D. Pfister, C. Grotz, I. Krüger, M. Greiwe, T. Hansen, H. Kohlmann, T. Nilges, *J. Cryst. Growth* 2014, 405, 6-10

[338] C. Hao, B. Yang, F. Wen, J. Xiang, L. Li, W. Wang, Z. Zeng, B. Xu, Z. Zhao, Z. Liu and Y. Tian, *Adv. Mater.*, 2016, 28, 3194–3201.

[339] (a) T. Lu, S. Dong, C. Zhang, L. Zhang, G. Cui, *Coordination Chem. Rev.,* 2017, 332,

75-99 (b) S. S. Karade, B. R. Sankapal, *J. Electroanal. Chem.* 2017, 802, 131-138 (c) Y. Qiu, X. Li, M. Bai, H. Wang, D. Xue, W. Wang, J. Cheng, *Inorg. Chem. Front.*, 2017, 4, 675-682 (d) P. Xu, W. Zeng, S. Luo, C. Ling, J. Xiao, A. Zhou, Y. Sun, K. Liao, *Electrochim. Acta* 2017, 241, 41-49

[340] C. Zhang, H. Yin, M. Han, Z. Dai, H. Pang, Y. Zheng, Y. Q. Lan, J. Bao, J. Zhu, *ACS Nano*, 2014, 8, 3761-3770

[341] P. Yu, W. Fu, Q. Zeng, J. Lin, C. Yan, Z. Lai, B. Tang, K. Suenag, H. Zhang, Z. Liu, *Adv. Mater.* 2017, 29, 1701909-1701918, DOI: 10.1002/adma.201701909

[342] H. Wang, J. Deng, C. Xu, Y. Chen, F. Xu, J. Wang, Y. Wang, Energy Storage Materials 2017, 7, 216–221.

[343] A. Ramadoss., K. Yoon, M. Kwak, S. Kim, S. Ryu, J. Jang, J. Power Sources 2017, 337, 159-165.

[344] H. Li,, J. Song, L. Wang, X. Feng, R. Liu, W. Zeng, Z. Huang, Y. Ma, L. Wang, Nanoscale, 2017, 9, 193–200.

[345] H. Zhang, C. Lu, C. Chen, L. Xie, P. Zhou, Q. Kong, ChemElectroChem 2017, 4, 1–8.

[346] X. Jian, H. Yang, J. Li, E. Zhang, L. Cao, Z. Liang, Electrochim. Acta 2017, 228, 483–493.

[347] Z. Li, Y. Li, L. Wang, L. Cao, X. Liu, Z. Chen, D. Pan, M. Wu, Electrochim. Acta 2017, 235, 561–569.

[348] L. Liu, D. Ye, Y. Yu, L. Liu, Y. Wu, *Carbon* 2017, 111, 121-127

[349] L. Song, X. Cao, L. Li, Q. Wang, H. Ye, L. Gu, C. Mao, J. Song, S. Zhang, H. Niu, *Adv. Funct. Mater.* 2017, 27, 1700474-1700487.

[350] Y. Zheng, Z. Lin, W. Chen, B. Liang, H. Du, R. Yang, X. He, Z. Tang, X. Gui, J. Mater. Chem. A, 2017, 5, 5886–5894.

[351] Y. Li, X. Wang, Q. Yang, M. Javed, Q. Liu, Weina Xu, C. Hu, D. Wei, Electrochim. Acta

2017, 234, 63–70

[352] H. Li, Y. Yu, L. Liu, L. Liu, Y. Wu, Electrochim. Acta 2017, 228, 553–561.

[353] J. Zhu, S. Tang, J. Wu, X. Shi, B. Zhu, X. Meng, *Adv. Energy Mater*. 2017, *7*, 1601234-1601245

[354] H. Li, Y. Hou, F. Wang, M. Lohe, X. Zhuang, L. Niu, X. Feng, *Adv. Energy Mater*. 2017, *7*, 1601847-1601853.

[355] R. Soni, A. Raveendrana, S. Kurungot, *Nanoscale*, 2017, 9, 3593–3600.

[356] K. Li, J. Liu, Y. Huang, F. Bu, Y. Xu, *J. Mater. Chem. A*, 2017, 5, 5466–5474.

[357] Y. Fan, W. Song, X. Li, L. Fan, *Carbon* 2017, 111, 658-666.

[358] N. Li, X. Huang, H. Zhang, Y. Li, C. Wang, *ACS Appl. Mater. Interfaces* 2017, 9, 9763-9771

[359] P. Li, J. Li, Z. Zhao, Z. Fang, M. Yang, Z. Yuan, Y. Zhang, Q. Zhang, W. Hong, X. Chen, D. Yu, *Adv. Sci.* 2017, 1700003-1700012.

[360] S. Akbulut, M. Yilmaz, S. Raina, S. Hsu, W. Kang, Diamond & Related Materials 2017, 74, 222–228.

[361] A. Liu, H. Lv, H. Liu, Q. Li, H. Zhao, J Mater Sci: Mater Electron 2017, 28, 8452–8459.

[362] Y. Qiu, X. Li, M. Bai, H. Wang, D. Xue, W. Wang, J. Cheng, *Inorg. Chem. Front*., 2017, 4, 675–682.

[363] D. Zhao, Q. Zhang, W. Chen, X. Yi, S. Liu, Q. Wang, Y. Liu, J. Li, X. Li, H. Yu, *ACS Appl. Mater. Interfaces* 2017, 9, 13213-13222.

[364] J. Cao, T. Huang, R. Liu, X. Xi, D. Wu, *Electrochim. Acta* 2017, 230, 265–270.

[365] B. Yao, H. Wang, Q. Zhou, M. Wu, M. Zhang, C. Li, G. Shi, *Adv. Mater.* 2017, 1700974-1700981.

[366] F. Chen, P. Wan, H. Xu, X. Sun, *ACS Appl. Mater. Interfaces* 2017, 9, 17865−17871.

[367] X. Hou, T. Peng, J. Cheng, Q. Yu, R. Luo, Y. Lu, X. Liu, J. Kim, J. He, Y. Luo, Nano

Research, DOI 10.1007/s12274-017-1459-9.

[368] I. Moon, S. Yoon, J. Oh, *Chem. Eur. J.* 2017, 23, 597 – 604.

[369] Y. Wu, Q. Wang, T. Li, D. Zhang, M. Miao, *Electrochim. Acta* 2017, 245, 69–78

[370] H. Su, P. Zhu, L. Zhang, F. Zhou, G. Li, T. Li, Q. Wang, R. Sun, C. Wong, *J. Electroanal. Chem.* 2017, 786, 28–34.

[371] X. Li, K. Liu, Z. Liu, Z. Wang, B. Lia, D. Zhang, *Electrochim. Acta* 2017, 240, 43–52.

[372] C. Chen, J. Cao, Q. Lu, X. Wang, L. Song, Z. Niu, J. Chen, *Adv. Funct. Mater.* 2017, 27, 1604639-1604646.

[373] C. Liu, S. Zhao, Y. Lu, Y. Chang, D. Xu, Q. Wang, Z. Dai, J. Bao, M. Han, small 2017, *13,* 1603494-1603502.

[374] S. Chen, L. Wang, M. Huang, L. Kang, Z. Lei, H. Xu, F. Shi, Z. Liu, *Electrochim. Acta* 2017, 242, 10–18.

[375] C. Wan, Y. Jiao, J. Li, *J. Mater. Chem. A*, 2017, 5, 3819-3831.

[376] S. Xu, G. Wei, J. Li, W. Han, Y. Gogotsi, *J. Mater. Chem. A*, 2017, 5, 17442-17451

[377] (a) X. Xiao, T. Ding, L. Yuan, Y. Shen, Q. Zhong, X. Zhang, Y. Cao, B. Hu, T. Zhai, L. Gong, J. Chen, Y. Tong, J. Zhou, Z. L. Wang, *Adv. Energy Mater*., 2012, 2, 1328-1332. (b) Ji. Sun, Y. Huang, Y. N. S. Sea, Q. Xue, Z. Wang, M. Zhu, H. Li, X. Tao, C. Zhi, H. Hu, *Mater. Today Energy* 2017, 5, 1-14 (c) S. C. Lee, U. M. Patil, S. J. Kim, S. Ahn, S. W. Kang, S. C. Jun, *RSC Adv.*, 2016, 6, 43844–43854.

[378] (a) W. Tang, Y. Zhu, Y. Hou, L. Liu, Y. Wu, K. P. Loh, H. Zhang, K. Zhu, *Energy Environ. Sci.*, 2013, 6, 2093-2104 (b) J. Yan, Z. Fan, W. Sun, G. Ning, T. Wei, Q. Zhang, R. Zhang, L. Zhi, F. Wei, *Adv. Funct. Mater.*, 2012, 22, 2632-2641

[379] F. Luan, G. Wang, Y. Ling, X. Lu, H. Wang, Y. Tong, X. X. Liu, Y. Li, *Nanoscale*, 2013, 5, 7984-7990

[380] (a) L. Wu, R. Li, J. Guo, C. Zhou, W. Zhang, C. Wang, Y. Huang, Y. Li, J. Liu, *AIP Adv.*

2013, 3, 082129 (b) Y. Zhang, M. Zheng, M. Qu, M. Sun, H. Pang, *J. Alloys Compd.* 2015, 651, 214-221

[381] H. Pang, X. Li, Q. Zhao, H. Xue, W. Y. Lai, Z. Hu, W. Huang, *Nano Energy* 2017, 35, 138-145

[382] (a) Z. Gao, W. Yang, J. Wang, N. Song, X. Li, *Nano Energy* 2015, 13, 306-317, (b) J. Zhao, S. Wang, Z. Run, G. Zhang, W. Du, H. Pang, *Part. Part. Syst. Charact.* 2015, *32*, 880-885, (c) J. Zhao, J. Chen, S. Xu, M. Shao, Q. Zhang, F. Wei, J. Ma, M. Wei, D. G. Evans, X. Duan, *Adv. Funct. Mater.* 2014, *24*, 2938-2946

[383] Z. Pan, Y. Qiu, J. Yang, F. Ye, Y. Xu, X. Zhang, M. Liu, Y. Zhang, *Nano Energy* 2016, 26, 610-619

[384] J. Zhao, M. Zheng, Z. Run, J. Xia, M. Sun, H. Pang, *J. Power Sources* 2015, 285, 385-392

[385] S. Zhu, Z. Wang, F. Huang, H. Zhang, S. Li, *J. Mater. Chem. A*, 2017, 5, 9960-9969

[386] J. Sun, P. Zan, L. Ye, X. Yang, L. Zhao, *J. Mater. Chem. A*, 2017, 5, 9815-9823

[387] Y. Shao, H. Wang, Q. Zhang, Y. Li, *J. Mater. Chem. C*, 2013, 1, 1245-1251

[388] J. Yang, G. Li, Z. Pan, M. Liu, Y. Hou, Y. Xu, H. Deng, L. Sheng, X. Zhao, Y. Qiu, Y. Zhang, *ACS Appl. Mater. Interfaces* 2015, 7, 22172-22180

[389] (a) X. Wang, B. Liu, R. Liu, Q. Wang, X. Hou, D. Chen, R. Wang, G. Shen, Angew. Chem. Int. Ed. 2014, 53, 1849-1853, (b) D. Ghosh, M. Mandal, C. K. Das, *Langmuir* 2015, *31*, 7835-7843

[390] D. Kong, W. Ren, C. Cheng, Y. Wang, Z. Huang, H. Y. Yang, *ACS Appl. Mater. Interfaces* 2015, 7, 21334−21346

[391] J. Tao, N. Liu, L. Li, J. Su, Y. Gao, *Nanoscale* 2014, 6, 2922-2928

[392] H. Yang, H. Xu, M. Li, L. Zhang, Y. Huang, X. Hu, *ACS Appl. Mater. Interfaces* 2016, 8, 1774-1779

[393] C. Guan, W. Zhao, Y. Hu, Z. Lai, X. Li, S. Sun, H. Zhang, A. K. Cheetham, J. Wang, *Nanoscale Horiz.*, 2017, 2, 99-105

[394] (a) N. R. Chodankar, D. P. Dubal, A. C. Lokhande, A. M. Patil, J. H. Kim, C. D. Lokhande, *Sci. Rep.* 2016, 6, 39205 (b) G. S. Gund, D. P. Dubal, N. R. Chodankar, J. Y. Cho, P. Gomez-Romero, C. Park, C. D. Lokhande, *Sci. Rep.* 2015, 5, 12454

[395] (a) S. Trasatti, *Pure Appl. Chem.* 1986, 58, 955-966 (b) P. V. Rysselberghe, *Appl. Phys. Lett.* 1953, 21, 1550-1551 (c) J. Cheng, M. Sprik, *Phys. Chem. Chem. Phys.* 2012, 14, 11245-11267.

[396] (a) M. T. Greiner, M. G. Helander, W. M. Tang, Z. B. Wang, J. Qiu, Z. H. Lu, *Nat. Mater.* 2012, 11, 76-81 (b) C. A. Pan, T. B. Ma, *Appl. Phys. Lett.* 1980, 37, 714. (c) Z. Viskadourakis, M. L. Parames, O. Conde, M. Zervos, J. Giapintzakis, *Appl. Phys. Lett.* 2012, 101, 033505. (d) F. Chen, R. Schafranek, W. Wu, A. Klein, *J. Phys. D: Appl. Phys.* 2011, 44, 1. (e) M. N. Islam, M. O. Hakim, *J. Mater. Science Lett.* 1986, 5, 63

[397] (a) G. R. Li, Z. L. Wang, F. L. Zheng, Y. N. Ou, Y. X. Tong, *J. Mater. Chem.*, 2011, 21, 4217, (b) J. Chang, M. Jin, F. Yao, T. H. Kim, V. T. Le, H. Yue, F. Gunes, B. Li, A. Ghosh, S. Xie, Y. H. Lee, *Adv. Funct. Mater.* 2013, *23*, 5074-5083

[398] (a) Q. T. Qu, S. B. Yang, X. L. Feng, *Adv. Mater.*, 2011, 23, 5574, (b) X. Lu, Y. Zeng, M. Yu, T. Zhai, C. Liang, S. Xie, M. S. Balogun, Y. Tong, *Adv. Mater.* 2014, 26, 3148-3155 (c) Q. Tang, W. Wang, G. Wang, *J. Mater. Chem. A* 2015, 3, 6662-6670

[399] P. Yang, Y. Ding, Z. Lin, Z. Chen, Y. Li, P. Qiang, M. Ebrahimi, W. Mai, C. P. Wong, Z. L. Wang, *Nano Lett.*, 2014, *14*, 731-736

[400] W. Ma, H. Nan, Z. Gu, B. Geng, X. Zhang, *J. Mater. Chem. A*, 2015, 3, 5442

[401] J. Xu, Q. Wang, X. Wang, Q. Xiang, B. Liang, D. Chen, G. Shen, *ACS Nano*, 2013, 7, 5453-5462

[402] X. Lu, T. Zhai, X. Zhang, Y. Shen, L. Yuan, B. Hu, L. Gong, J. Chen, Y. Gao, J. Zhou,

Y. Tong, Z. L. Wang, *Adv. Mater.* 2012 , *24* , 938

[403] Z. Yu, J. Moore, J. Calderon, L. Zhai, J. Thomas, *Small* 2015, *11,* 39, 5289-5295

[404] T. Gu, B. Wei, *J. Mater. Chem. A*, 2016, 4, 12289

[405] X. Lu, M. Yu, G. Wang, T. Zhai, S. Xie, Y. Ling, Y. Tong, Y. Li, *Adv. Mater.* 2013, *25*, 267-272

[406] (a) S. Murugesan, P. Kuppusami, N. Parvathavarthini, E. Mohandas, *Surf. Coat. Technol.* 2007, *201*, 7713 (b) G. M. Wang, H. Y. Wang, Y. C. Ling, Y. C. Tang, X. Y. Yang, R. C. Fitzmorris, C. C. Wang, J. Z. Zhang, Y. Li, *Nano Lett.* 2011, *11*, 3026

[407] (a) L. Y. Yuan, X. H. Lu, X. Xiao, T. Zhai, J. J. Dai, F. C. Zhang, B. Hu, X. Wang, L. Gong, J. Chen, C. G. Hu, Y. X. Tong, J. Zhou, Z. L. Wang, *ACS Nano* 2012, *6*, 656. (b) X. H. Lu, D. Z. Zheng, T. Zhai, Z. Q. Liu, Y. Y. Huang, S. L. Xie, Y. X. Tong, *Energy Environ. Sci.* 2011, *4*, 2915.

[408] J. X. Feng, S. H. Ye, X. F. Lu, Y. X. Tong, G. R. Li, *ACS Appl. Mater. Interfaces* 2015, 7, 11444-11451

[409] H. Gao, F. Xiao, C. B. Ching, H. Duan, *ACS Appl. Mater. Interfaces* 2012, 4, 7020-7026

[410] (a) B. Avasarala, P. Haldar, *Electrochim. Acta* 2010, 55, 9024 (b) I. Milošv, H. H. Strehblow, B. Navinšek, M. Metikoš-Hukovic, *Surf. Interface Anal.* 1995, 23, 529.

[411] X. Lu, M. H. Yu, T. Zhai, G. Wang, S. Xie, T. Lu, C. Liang, Y. X. Tong, Y. Li, *Nano Lett.*, 2013, 13, 2628

[412] (a) A. Achour, J. B. Ducros, R. L. Porto, M. Boujtita, E. Gautron, L. Le Brizoual, M. A. Djouadi, T. Brousse, *Nano Energy* 2014, 7, 104 (b) Z. L. Wang, *Nano Today* 2010, 5, 540.

[413] (a) Y. Yue, P. Han, X. He, K. Zhang, Z. Liu, C. Zhang, S. Dong, L. Gu, G. Cui, *J. Mater. Chem.* 2012, 22, 4938 (b) Y. Qiu, K. Yan, S. Yang, L. Jin, H. Deng, W. Li, *ACS Nano* 2010, 4, 6515 (c) F. Tian, Y. Xie, H. Du, Y. Zhou, C. Xia, W. Wang, *RSC Adv.* 2014, 4,

41856

[414] C. Zhu, P. Yang, D. Chao, X. Wang, X. Zhang, S. Chen, B. K. Tay, H. Huang, H. Zhang, W. Mai, H. J. Fan, *Adv. Mater.* 2015, 27, 4566–4571.

[415] X. F. Lu, X. Y. Chen, W. Zhou, Y. X. Tong, G. R. Li, *ACS Appl. Mater. Interfaces* 2015, 7, 14843-14850

[416] Y. Jin, H. Chen, M. Chen, N. Liu, Q. Li, *ACS Appl. Mater. Interfaces* 2013, 5, 3408-3416

[417] N. Kurra, R. Wang, H. N. Alshareef, *J. Mater. Chem. A*, 2015, 3, 7368

[418] Z. Zheng, M. Retana, X. Hu, R. Luna, Y. Ikuhara, W. Zhou, *ACS Appl. Mater. Interfaces* 2017, 9, 16986-16994

[419] C. Ji, F. Liu, L. Xu, S. Yang, *J. Mater. Chem. A*, 2017, 5, 5568-5576

[420] P. Li, Z. Jin, D. Xiao, *J. Mater. Chem. A*, 2017, 5, 3274-3283

[421] J. Zhao, M. Zheng, Z. Run, J. Xia, M. Sun, H. Pang, *J. Power Sources*, 2015, 285, 385-392.

[422] Z. Zhang, K. Chi, F. Xiao, S. Wang, *J. Mater. Chem. A*, 2015, 3, 12828-12835.

[423] H. Yang, H. Xu, M. Li, L. Zhang, Y. Huang, X. Hu, *ACS Appl. Mater. Interfaces*, 2016, 8, 1774-1779

[424] J. X. Feng, S. H. Ye, X. F. Lu, Y. X. Tong, G. R. Li, *ACS Appl. Mater. Interfaces*, 2015, 7, 11444-11451.

[425] J. Zhao, S. Wang, Z. Run, G. Zhang, W. Du, H. Pang, *Part. Part. Syst. Charact.*, 2015, 32, 880-885.

[426] C. Wei, C. Cheng, B. Zhou, X. Yuan, T. Cui, S. Wang, M. Zheng, H. *Pang, Part. Part. Syst. Charact.* 2015, 32, 831-839.

[427] D. Kong, W. Ren, C. Cheng, Y. Wang, Z. Huang, H. Y. Yang, *ACS Appl. Mater. Interfaces*, 2015, 7, 21334-21346.

[428] D. Kong, C. Cheng, Y. Wang, J. I. Wong, Y. Yang, H. Y. Yang, *J. Mater. Chem. A*, 2015, 3, 16150-16161.

[429] G. Sun, X. Zhang, R. Lin, J. Yang, H. Zhang, P. Chen, *Angew. Chem. Int. Ed.*, 2015, 54, 4651-4656.

[430] D. Ghosh, M. Mandal, C. K. Das, *Langmuir*, 2015, 31, 7835-7843.

[431] H. Pang, Y. Zhang, W. Y. Laib, Z. Huc, W. Huang, *Nano Energy*, 2015, 15, 303-312.

[432] Z. Zhang, F. Xiao, S. Wang, *J. Mater. Chem. A*, 2015, 3, 11215-11223.

[433] Z. Zhang, F. Xiao, J. Xiao, S. Wang, *J. Mater. Chem. A,* 2015, 3, 11817-11823.

[434] N. Yu, M. Q. Zhu, D. Chen, *J. Mater. Chem. A*, 2015, 3, 7910-7918.

[435] Z. Gao, W. Yang, J. Wang, N. Song, X. Li, *Nano Energy*, 2015, 13, 306-317

[436] Y. Zhang, M. Zheng, M. Qu, M. Sun, H. Pang, *J. Alloys Compd.,* 2015, 651, 214-221.

[437] Y. Chen, B. Liu, Q. Liu, J. Wang, Z. Li, X. Jing, L. Liu, *Nanoscale*, 2015, 7, 15159-15167.

[438] N. R. Chodankar, D. P. Dubal, G. S. Gund, C. D. Lokhande, *Energy Technol.*, 2015, 3, 625-631.

[439] A. V. Shinde, N. R. Chodankar, V. C. Lokhande, A. C. Lokhande, T. Ji, J. H. Kim, C. D. Lokhande, *RSC Adv.*, 2016, 6, 58839-58843

[440] H. Xie, S. Tang, J. Zhu, S. Vongehr, X. Meng, *J. Mater. Chem. A,* 2015, 3, 18505-18513.

[441] T. Chen, Y. Tang, Y. Qiao, Z. Liu, W. Guo, J. Song, S. Mu, S. Yu, Y. Zhao, F. Gao, *Sci. Rep.*, 2016, 6, 23289.

[442] Q. Wang, Y. Ma, Y. Wu, D. Zhang, M. Miao, *ChemSusChem* 2017, 10, 1427 – 1435.

[443] K. Subramani, N. Sudhan, R. Divya, M. Sathish, *RSC Adv.*, 2017, 7, 6648–6659.

[444] W. Liu, K. Feng, Y. Zhang, T. Yu, L. Han, G. Lui, M. Li, G. Chiu, P. Fung, A. Yu, *Nano Energy* 2017, 34, 491–499.

[445] J. Noh, C. Yoon, Y. Kim, J. Jang, *Carbon* 2017, 116, 470-478.

[446] H, Pang, X. Li, Q. Zhao, H. Xue, W. Lai, Z. Hu, W. Huang, *Nano Energy* 2017, 35, 138–145.

[447] Z. Zheng, M. Retana, X. Hu, R. Luna, Y. Ikuhara, W. Zhou, *ACS Appl. Mater. Interfaces* 2017, 9, 16986−16994.

[448] K. Chi, Z. Zhang, Q. Lv, C. Xie, J. Xiao, F. Xiao, S. Wang, *ACS Appl. Mater. Interfaces* 2017, 9, 6044−6053.

[449] J. Wang, L. Zhang, X. Liu, X. Zhang, Y. Tian, X. Liu, J. Zhao, Y. Li, *Sci. Rep*., 2017, 7, 41088

[450] Z. Tian, H. Dou, B. Zhang, W. Fan, X. Wang, *Electrochimica Acta* 2017, 237, 109–118.

[451] M. Zheng, L. Li, P. Gu, Z. Lin, W. Du, H. Xue, H. Pang, *Energy Technol*. 2017, 5, 544-548

[452] H. Wang, C. Xu, Y. Chen, Y. Wang, *Energy Storage Materials* 2017, 8, 127–133.

[453] Z. Pan, M. Liu, J. Yang, Y. Qiu, W. Li, Y. Xu, X. Zhang, Y. Zhang, *Adv. Funct. Mater.* 2017, 1701122-1701131.

[454] K. Ghosh, C. Yue, M. Sk, R. Jena, *ACS Appl. Mater. Interfaces* 2017, 9, 15350−15363.

[455] H. Xie, S. Tang, D. Li, S. Vongehr, X. Meng, *ChemSusChem* 2017, 10, 2301 – 2308.

[456] L. Gao, J. Surjadi, K. Cao, H. Zhang, P. Li, S. Xu, C. Jiang, J. Song, D. Sun, Y. Lu, *ACS Appl. Mater. Interfaces* 2017, 9, 5409−5418

[457] Y. Liu, N. Fu, G. Zhang, M. Xu, W. Lu, L. Zhou, H. Huang, *Adv. Funct. Mater.* 2017, *27*, 1605307-1605318.

[458] H. Pang, X. Li, Q. Zhao, H. Xue, Wen-Yong Lai, Z. Hu, W. Huang, *Nano energy*, 2017, 35, 138-145.

[459] S. Cheng, T. Shi, Y. Huang, X. Tao, J. Li, C. Cheng, G. Liao, Z. Tang, *Ceramics International* 2017, 43, 2155–2164.

[460] X. He, Q. Liu, J. Liu, R. Li, H. Zhang, R. Chen, J. Wang, *Chem. Eng. J.* 2017, 325, 134–143.

[461] T. Wang, S. Zhang, X. Yan, M. Lyu, L. Wang, J. Bell, H. Wang, *ACS Appl. Mater. Interfaces* 2017, 9, 15510−15524.

[462] Y. Zhong, T. Shi, Z. Liu, Y. Huang, S. Cheng, C. Cheng, X. Li, G. Liao, Z. Tang, *Energy Technol*. 2017, 5, 656 – 664.

[463] W. Ma, S. Chen, S. Yang, W. Chen, W. Weng, Y. Cheng, M. Zhu, *Carbon* 2017, 113, 151-158

[464] K. Lu, J. Zhang, Y. Wang, J. Ma, B. Song, H. Ma, *ACS Sustainable Chem. Eng*. 2017, 5, 821−827

[465] J. Zhao, C. Li, Q. Zhang, J. Zhang, X. Wang, Z. Lin, J. Wang, W. Lv, C. Lu, C. Wong, Y. Yao*, J. Mater. Chem. A*, 2017, 5, 6928–6936

[466] (a) F. R. Fan, W. Tang, Z. L. Wang, *Adv. Mater.* 2016, 28, 4283-4305. (b) T. Q. Trung, N. E. Lee, *Adv. Mater.* 2016, 28, 4338-4372. (c) Y. Huang, M.S. Zhu, Y. Huang, Z. X. Pei, H.F. Li, Z.F. Wang, Q. Xue, C.Y. Zhi, *Adv. Mater.* 2016, 28, 8344–8364.

[467] Z. Wang, J. Song, *Science*, 2006, 312, 242-246.

[468] (a) Z. L. Wang, T. Jiang, L. Xu, *Nano Energy* 2017, 39, 9-23 (b) J. Ma, Y. Jie, J. Bian, T. Li, X. Cao, N. Wang, *Nano Energy* 2017, 39, 192-199

[469] (a) Z. Tian, J. He, X. Chen, Z. Zhang, T. Wen, C. Zhai, J. Han, J. Mu, X. Hou, X. Chou, C. Xue, *Nano Energy* 2017, 39, 562-570 (b) W. Gong, C. Hou, Y. Guo, J. Zhou, J. Mu, Y. Li, Q. Zhang, H. Wang, *Nano Energy* 2017, 39, 673-683

[470] (a) X. Wang, Y. Yin, F. Yi, K. Dai, S. Niu, Y. Han, Y. Zhang, Z. You, *Nano Energy* 2017, 39, 429-436 (b) X. He, Y. Zia, H. Yu, S. L. Zhang, J. Wang, W. Ding, H. Zou, W. Zhang, C. Lu, Z. L. Wang, *Nano Energy* 2017, 39, 328-336 (c) A. Maitra, S. K. Karan, S. Paria, A. K. Das, R. Bera, L. Halder, S. K. Si, A. Bera, B. B. Khatua, *Nano Energy* 2017, 40,

633-645

[471] R. Song, H. Jin, X. Li, L. Fei, Y. Zhao, H. Huang, H. L. Chan, Y. Wang, Y. Chai, *J. Mater. Chem. A*, 2015, 3, 14963–14970

[472] A. Ramadoss, B. Saravanakumar, S. W. Lee, Y. S. Kim, S. J. Kim, Z. L. Wang, *ACS Nano*, 2015, 9, 4337–4345

[473] J. Luo, F. R. Fan, T. Jiang, Z. Wang, W. Tang, C. Zhang, M. Liu, G. Cao and Z. L. Wang, *Nano Res.*, 2015, 8, 3934-3943.

[474] (a) A. Scalia, F. Bella, A. Lamberti, S. Bianco, C. Gerbaldi, E. Tresso, C. F. Pirri, *J. Power Sources* 2017, 359, 311-321 (b) P. Yang, X. Xiao, Y. Li, Y. Ding, P. Qiang, X. Tan, W. Mai, Z. Lin, W. Wu, T. Li, H. Jin, P. Liu, J. Zhou, C. P. Wong, Z. L. Wang, *ACS Nano*, 2013, 7, 2617–2626

[475] X. Chen, H. Sun, Z. Yang, G. Guan, Z. Zhang, L. Qiu, H. Peng, *J. Mater. Chem. A*, 2014, 2, 1897-1902

[476] Z. Zhang, X. Chen, P. Chen, G. Guan, L. Qiu, H. Lin, Z. Yang, W. Bai, Y. Luo, H. Peng, *Adv. Mater* 2014, 26, 466-470

[477] C. Li, M. Islam, J. Moore, J. Sleppy, C. Morrison, K. Konstantinov, *Nat. Publ. Gr* 2016, 7, 1-10

[478] L. Liu, B. Shen, D. Jiang, R. Guo, L. Kong and X. Yan, *Adv. Energy Mater.*, 2016, 6, 1600763

[479] Y. Huang, M. Zhu, Z. Pei, Q. Xue, Y. Huang, C. Zhi, *J. Mater. Chem. A*, 2016, 4, 1290-1297.

[480] J. Deng, Y. Zhang, Y. Zhao, P. Chen, X. Cheng and H. Peng, *Angew. Chem., Int. Ed.*, 2015, 54, 15419-15423.

[481] J. Zhong, J. Meng, Z. Yang, P. Poulind, N. Koratkar, *Nano Energy*, 2015, 17, 330-338.

[482] (a) B. E. Logan, K. Rabaey, *Science* 2012, 337, 686-690. (b) R. D. Cusick, Y. Kim, B.

E. Logan, *Science* 2012, 335, 1474-1477. (c) B. E. Logan, *Nat. Rev. Microbiol.* 2009, 7, 375-381.

[483] (a) N. Uría, X. Muñ oz Berbel, O. Sánchez, F.X. Muñ oz, J. Mas, *Environ. Sci. Technol.* 2011, 45, 10250-10256. (b) A. Deeke, T. H. Sleutels, H. V. Hamelers, C. J. Buisman, *Environ. Sci. Technol.* 2012, 46, 3554-3560. (c) E. J. Gardel, M. E. Nielsen, P. T. Grisdela Jr, P. R. Girguis, *Environ. Sci. Technol.* 2012, 46, 5222-5229.

[484] N. S. Malvankar, T. Mester, M. T. Tuominen, D. R. Lovley, *ChemPhysChem* 2012, 13, 463-468.

[485] H. Ren, H. Tian, H. S. Lee, T. Park, F. C. Leung, T. L. Ren, J. Chae, *Nano Energy* 2015, 15, 697-708

[486] R. S. Jayashree, M. Mitchell, D. Natarajan, L. J. Markoski, P. J. Kenis, *Langmuir* 2007, 23, 6871-6874.

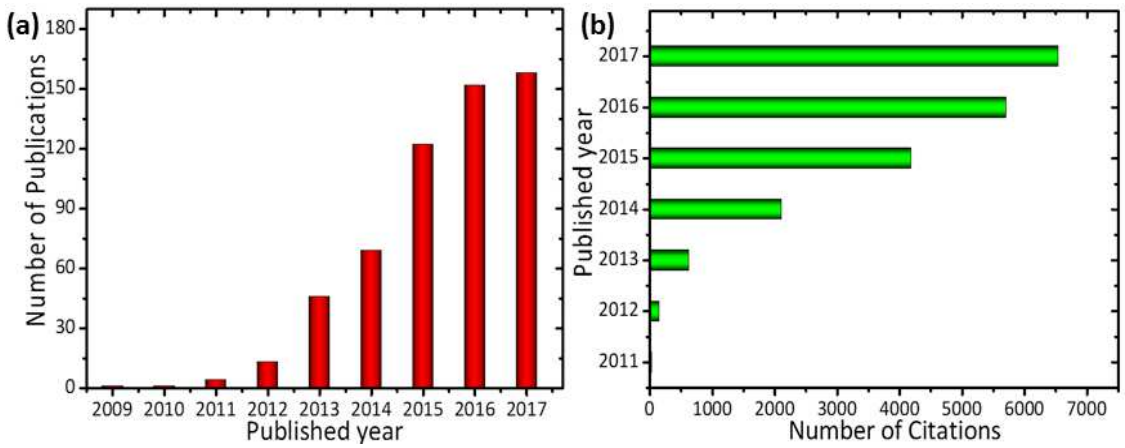

Figure 1 Statistics of number of papers published and number of citations per year. The results obtained for “Flexible solid-state supercapacitors” from scoups as of october 2017.

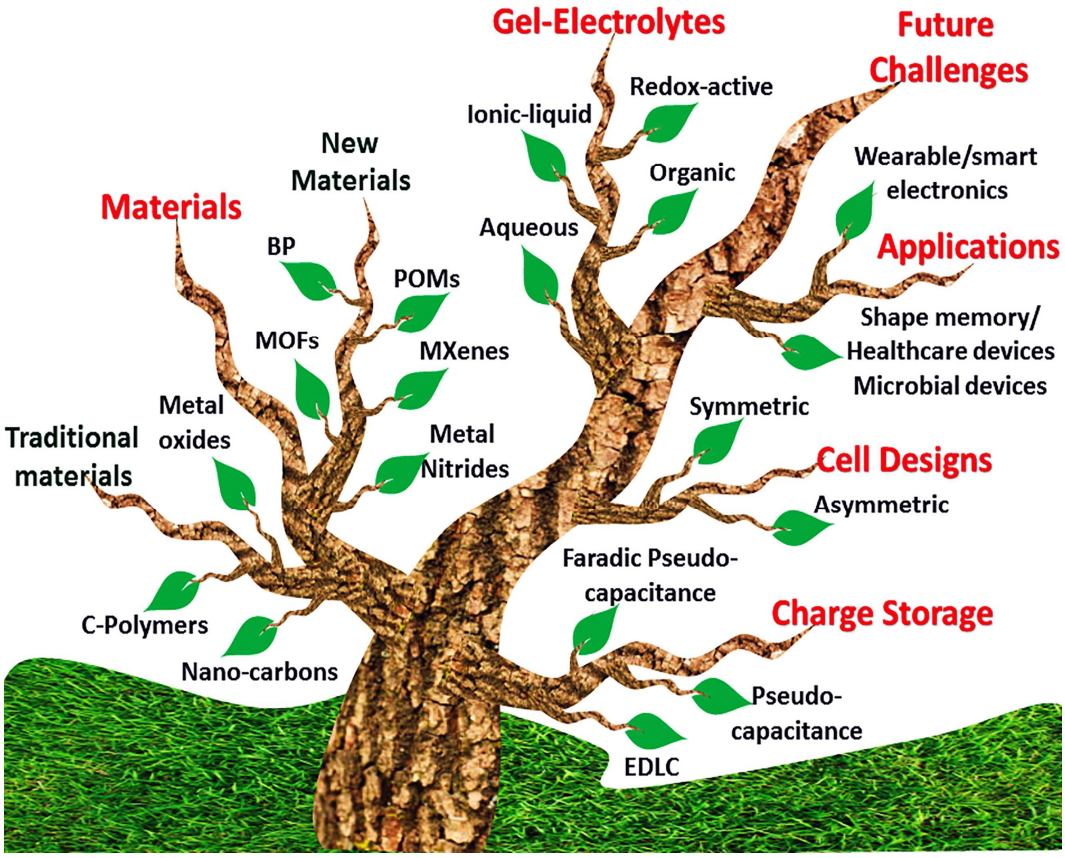

Figure 2 An overview of the latest advancement in the field of flexible solid-state supercapacitors (FSSCs) as a green energy storage technology.

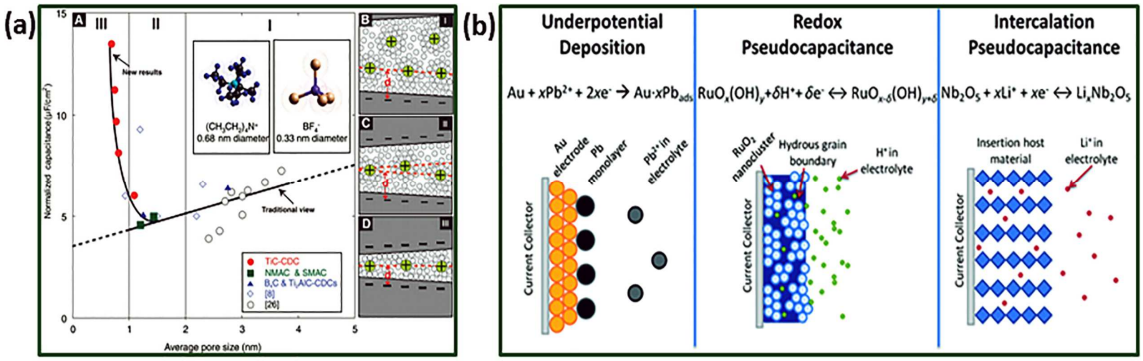

Figure 3 (a) Plot of specific capacitance vs normalized by BET SSA for the carbons suggesting decrease in capacitance with pore size until a critical value. Reprinted with the permission from [23a], Copyright 2006, The American Association for the Advancement of Science. (b) Different types of reversible redox mechanisms that give rise to pseudocapacitance: (a) underpotential deposition, (b) redox pseudocapacitance, (c) intercalation pseudocapacitance. Reproduced with Permission from from [21a], Copyright 2014, Royal Society of Chemistry.

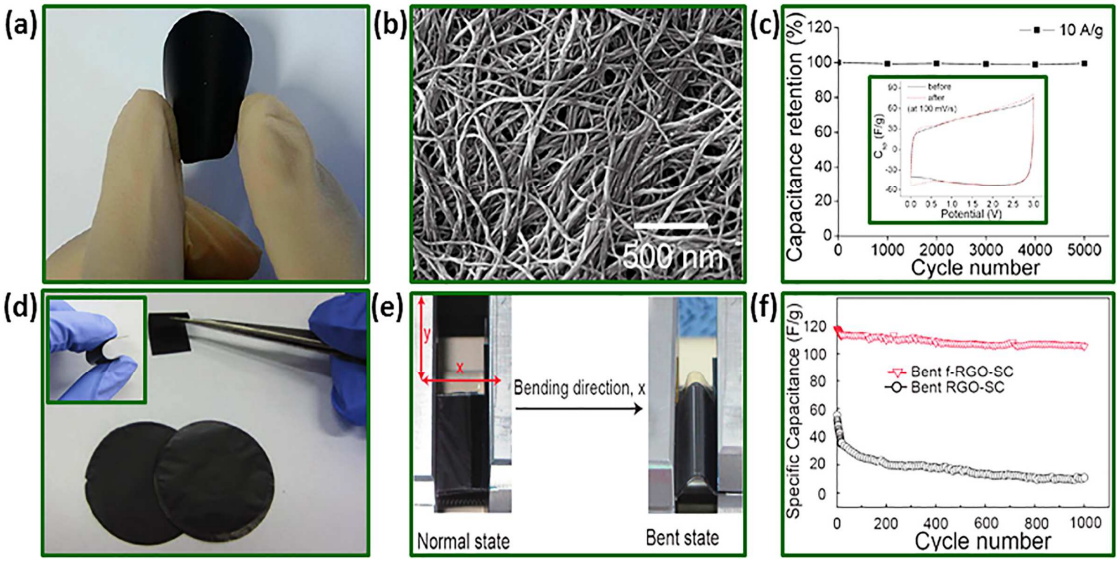

Figure 4 (a) Flexible CNT-coated bacterial nanocellulose (BNC) paper, (b) SEM image of CNTs coated on a BNC paper (c) Capacitance retention over 5000 cycles of charge/discharge at a current density of 10 A/g, inset shows CV curves measured before and after 200 bending cycles, Reprinted with permission from [30d], Copyright 2012 American Chemical Society. (d) Photograph of free-standing f-RGO films, inset shows the photograph of all solid-state flexible thin f-RGO-SC (e) Photographs of SC prior to the bent experiments, (f) Stability test of RGO-SC and f-RGO-SC by measuring 1000 charge-discharge cycles with a constant current density of 1 A/g at the bent state. Reprinted with permission from [45], Copyright 2012 American Chemical Society.

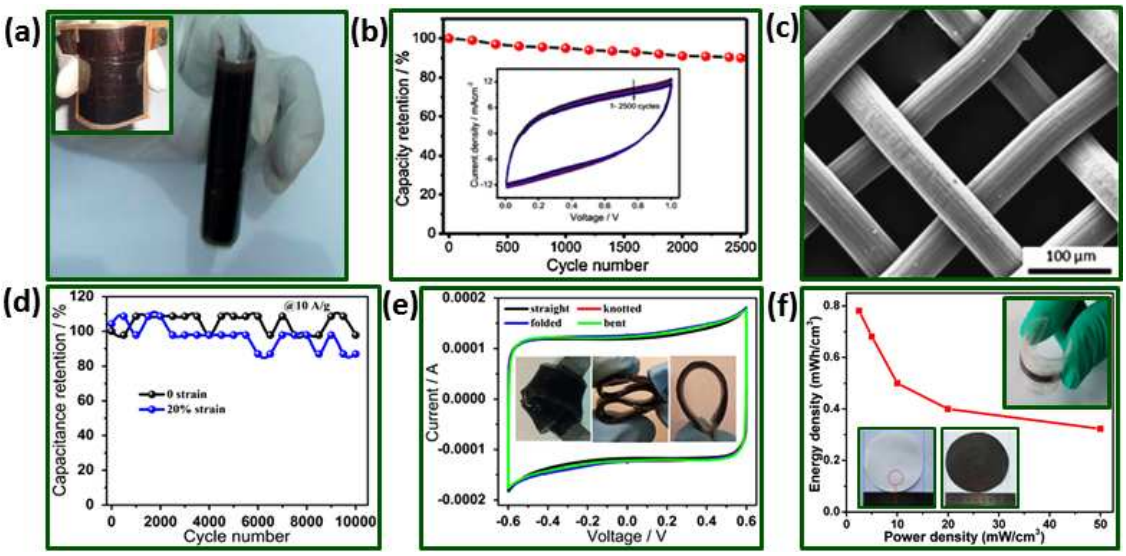

Figure 5 (a) FSSC device with MnO_2 nanoflakes electrodes in normal and bending conditions. Reprinted with permission from [69b], Copyright 2016 Elsevier. (b) Cycling stability of MnO_2 based FSC in bending state using CMC-Na_2SO_4 gel as an electrolyte. Reprinted with permission from [69a], Copyright 2015 Elsevier. (c) Low magnified SEM image of polypyrrole deposited on SS mesh, (d) Capacitance retentions as functions of cycle number at a specific current of 10 A/g under 0 (black) and 20 % strain (blue). (e) CV curves of the fabricated PPy based stretchable supercapacitors at various kinds of deformation. Reprinted with permission from [73], Copyright 2014 Elsevier. (f) Ragone plot for Ni/MnO_2−FP//Ni/AC−FP FSC, inset shows synthesized Ni/MnO_2-filter paper and digital photograph of final Ni/MnO_2-FP//Ni/AC-FP asymmetric device. Reproduced with permission from [82], Copyright 2016, American Chemical Society.

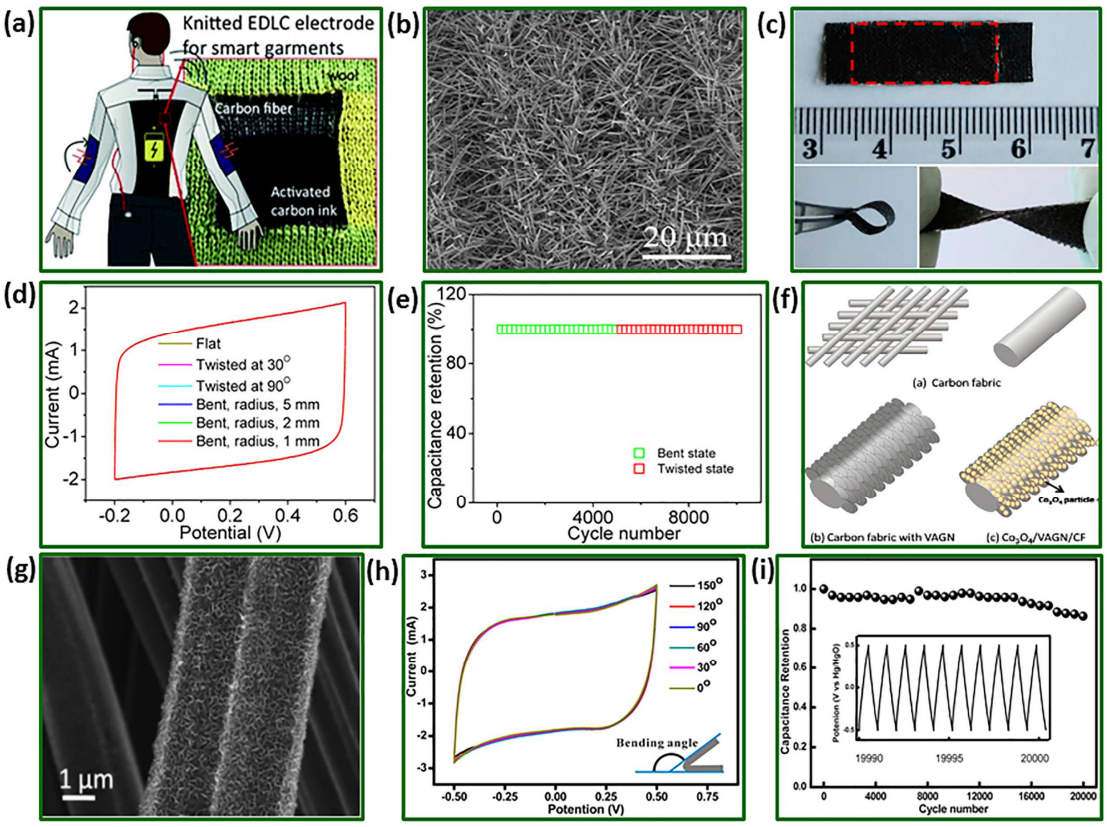

Figure 6 (a) Schematic of textile based supercapacitors for wearable electronics, Reproduced with permission from [85 a], Copyright 2013, Royal Society of Chemistry. (b-e) SEM image of single crystalline SiC nanowires on carbon fabric, Digital photographs of FSSC based on SiC with corresponding CV curves at normal and bending conditions, cycling stability at bent and twisted conditions, respectively, Reproduced with permission from [88], Copyright 2015, American Chemical Society. (f-i) Pictorial presentation of steps involved in the synthesis of vertically aligned graphene nanosheets (VAGNs) decoared with Co_3O_4 nanoparticles, SEM image of VAGNs on carbon fabric, CV curves for Co_3O_4/VAGNs/Carbon fabric solid-state cell at different bending conditions and cycling stability for 20,000 cycles, respectively, Reproduced with permission from [92], Copyright 2015, American Chemical Society.

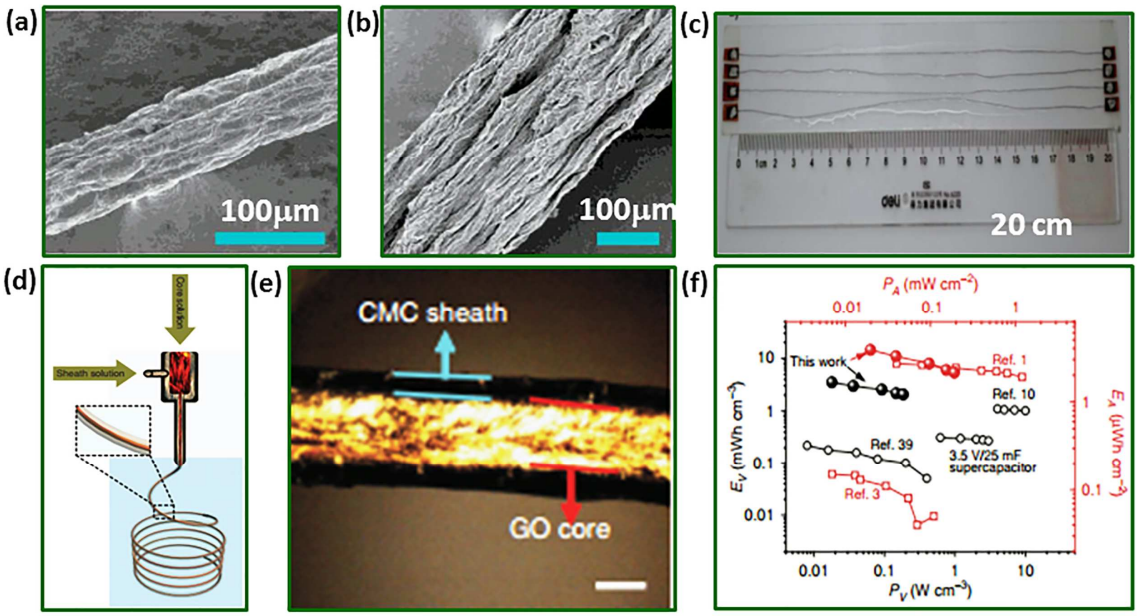

Figure 7 (a, b) SEM images of graphene fibers of two different sizes such as 100 μm and 35 μm, respectively (c) Digital photograph of planar fiber-based SC, Reproduced with permission from [95], Copyright 2013, Royal Society of Chemistry. (e) Schematic illustration of preparation of GO@CMC core-shell fibers by coaxial spinning process. (f) Polarized-light optical microscopy image of wet GO@CMC fibre showing the core-sheath structure and the well-aligned GO sheets in the core part, (j) Ragone plots compared with the reported fibre-shaped yarn-SCs with solid electrolyte, Reproduced with permission from [96], Copyright 2014, Nature Publishing Group.

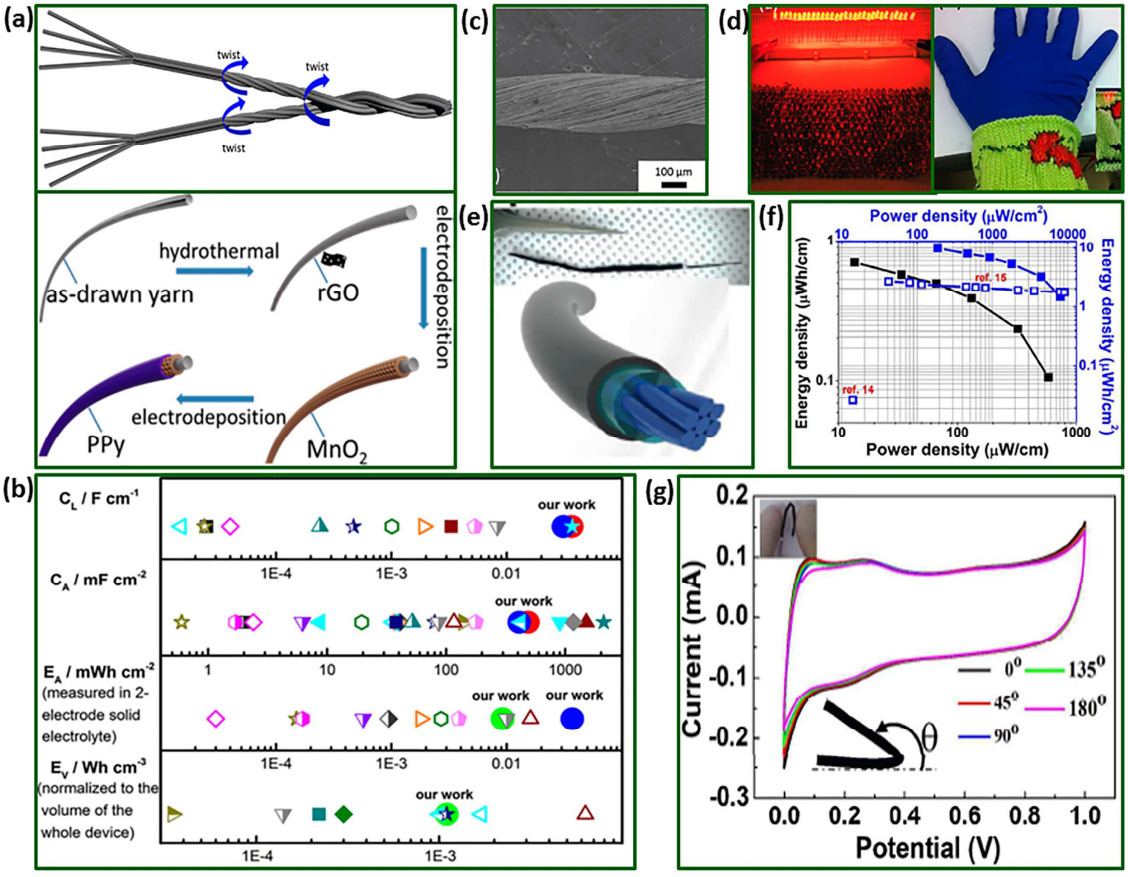

Figure 8 (a) Steps involved in the fabrication of yarn and subsequent deposition of MnO_2 and PPy thin films on to the yarn (b) Comparison of electrochemical performance of various fiber/yarn-based electrocapacitive materials (C_L and C_A are length and areal capacitances, E_A and E_V are areal and volumetric energy densities). (c) SEM image of an as-drawn yarn, Adopted with permission from [101], Copyright 2013, American Chemical Society. (d) Schematic and digital photo of a coaxial-fiber SC. (e) Ragone plot with energy and power density per length or area of the core electrode. (f) CV curves with different bending angles at a scan rate of 5 mV/s and inset shows the digital photograph of bended yarn-FSCs. Reprinted with permission from Ref. [102], Copyright 2013, American Chemical Society.

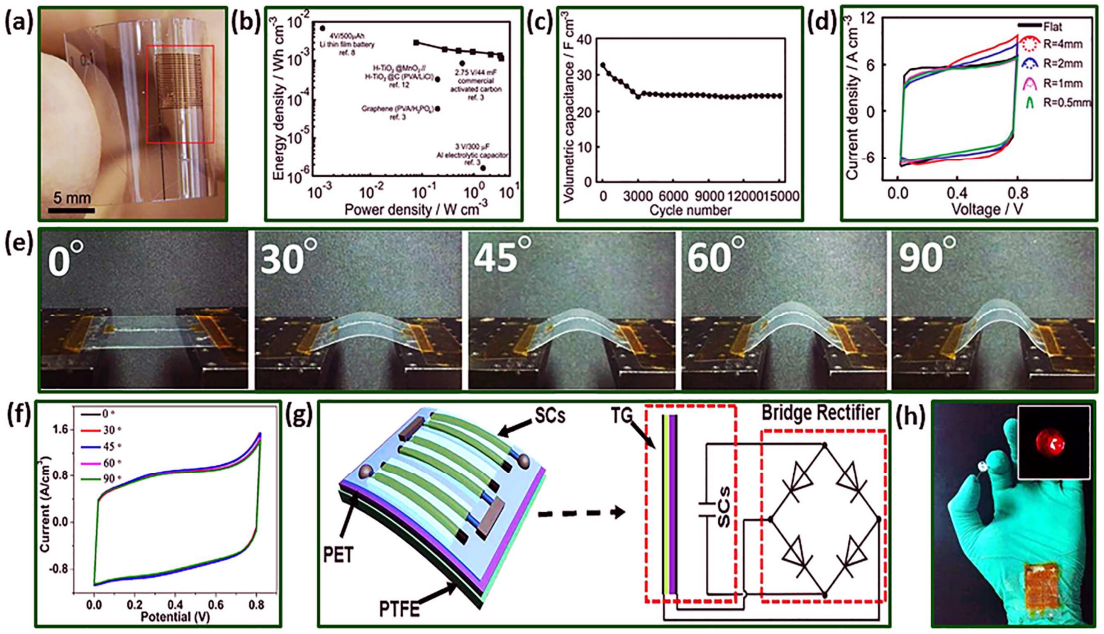

Figure 9 (a) Photograph of a fabricated flexible micro-supercapacitor on a polyethylene terephthalate (PET) substrate, (b) Ragone plot of the microsupercapacitor, (c) Cycling stability of MnOx/Au multilayer micro-supercapacitors, measured at a scan rate of 1 V/s (d) CV curves at different bending states, indicated by diameters of curvature, respectively. Reprinted with permission from [110], Copyright 2013, Royal Society of Chemistry. (e) Optical images of MnO_2@carbon fiber single device on PET substrate bended with different angles (f) CV curves for MnO_2@carbon FSCs at different bending conditions (g) Schematic diagram of energy modulus integrated by three SCs connected in series and a triboelectric generator. (h) Digital photograph of the energy modulus that is powering commercialized LED. Reprinted with permission from Ref. [111], Copyright 2012 American Chemical Society.

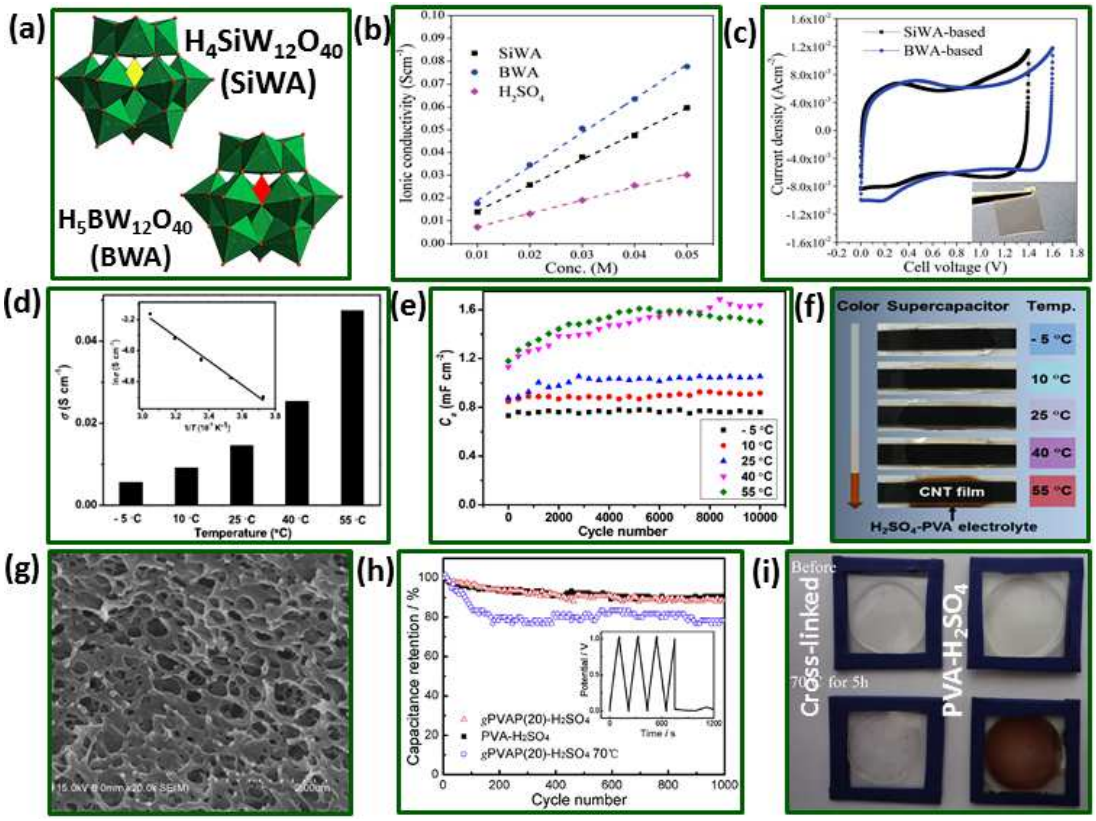

Figure 10 (a) Structures of SiWA and BWA hetero polyacids, Adopted with the permission from [203a], Copyright 2016, Royal Society of Chemistry. (b) Ionic conductivities of SiWA, BWA, and H_2SO_4 at different electrolyte concentrations (c) CVs curves of CNT-graphite electrodes with SiWA- and BWA-based gel electrolytes at 1 V/s, inset shows a picture of a polymer electrolyte film. Reprinted with permission from [203b], Copyright 2015, Royal Society of Chemistry. (d) Ionic conductivities of H_2SO_4-PVA electrolyte at various temperatures with corresponding plot of logσ vs. 1/T. (e) Variations in areal specific capacitances of CNTs and H_2SO_4-PVA with cycle number at different temperatures. (f) Change in the colour of cells after 10,000 cycles at different temperatures, suggesting aging of electrolyte. Reprinted with permission from [205], Copyright 2017, Elsevier. (g) Cross-sectional SEM image of cross-linked H_2SO_4-PVA gel-electrolyte (h) Cycling stability of graphene/carbon black electrode with and without cross-linked H_2SO_4-PVA gel-electrolyte at room temperature and 70°C. (i) Photographs of with and without cross linked H_2SO_4-PVA gel-electrolytes before and after thermal treatment at 70 °C for 5 h. Reprinted with permission from [109], Copyright 2014, Elsevier.

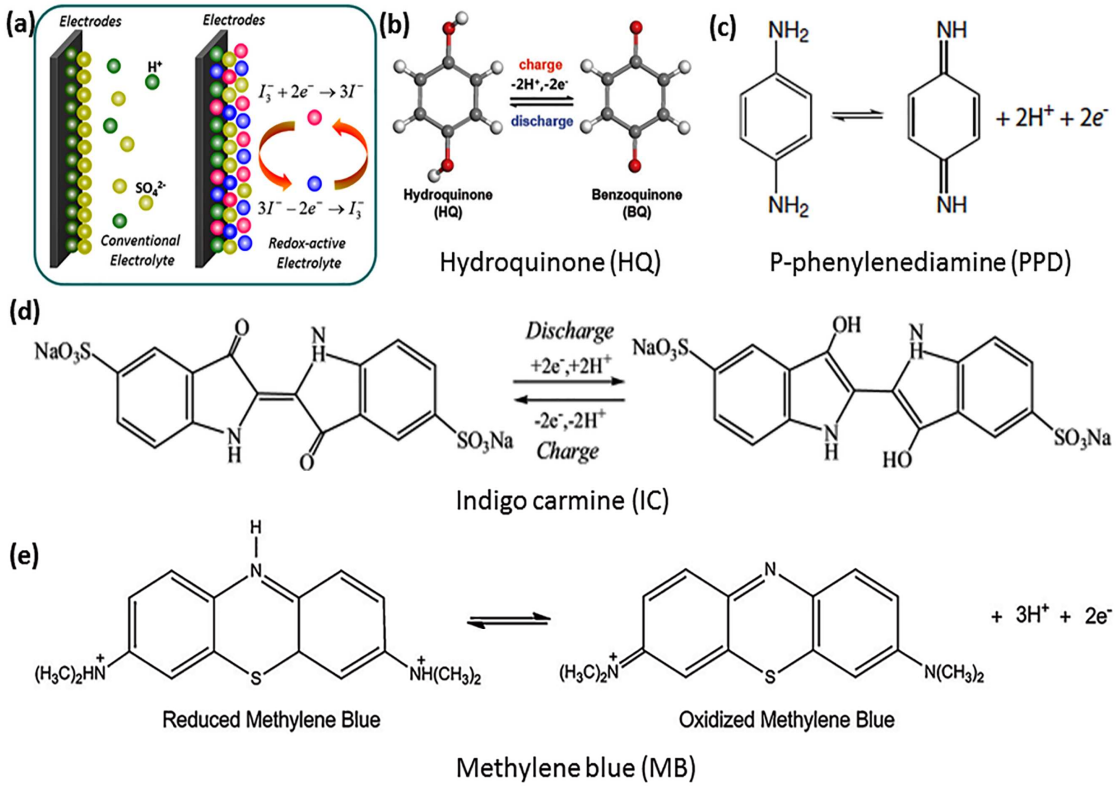

Figure 11 (a) Schematics illustration of charge storing mechanism in conventional and redox-active electrolytes (e.g. KI). Reaction mechanisms of different organic redox-active electrolytes during charge/discharge process (b) hydroquinone (HQ) (c) p-phenylenediamine (PPD) (d) Indigo carmine (IC) and (e) methylene blue (MB).

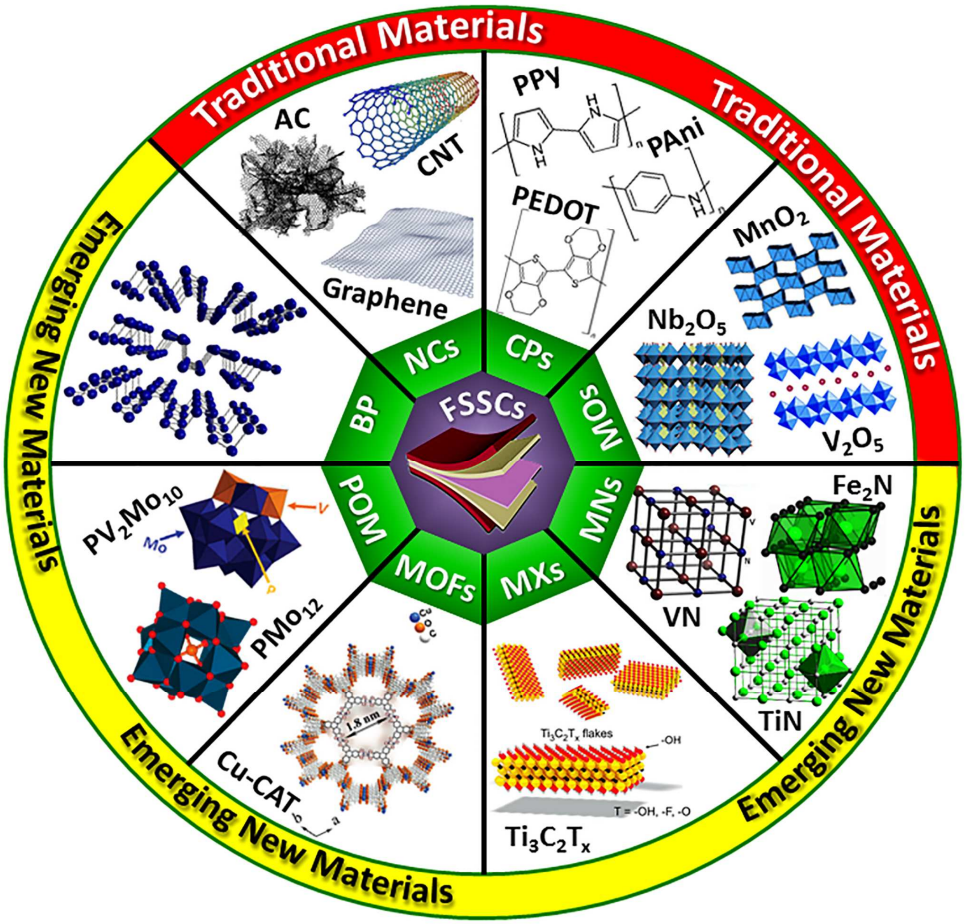

Figure 12 An overview of promising electrode materials used so far for flexible solid-state supercapacitors (FSSCs). The materials are divided into two sub-sections such as traditional materials (NCs-Nanocarbons, CPs-Conducting polymers, MOs-metal oxides) and emerging new materials (MNs-Metal nitrides, MXs-MXenes, MOFs-Metal organic frameworks, POMs-polyoxometalates, BP-Black phosphorous). Modified and reprinted with the permission from [6b, 260a, 311b, 321c, 335, 337] Wiley-VCH Verlag GmbH & KGaA, Royal society of chemistry, Elsevier.

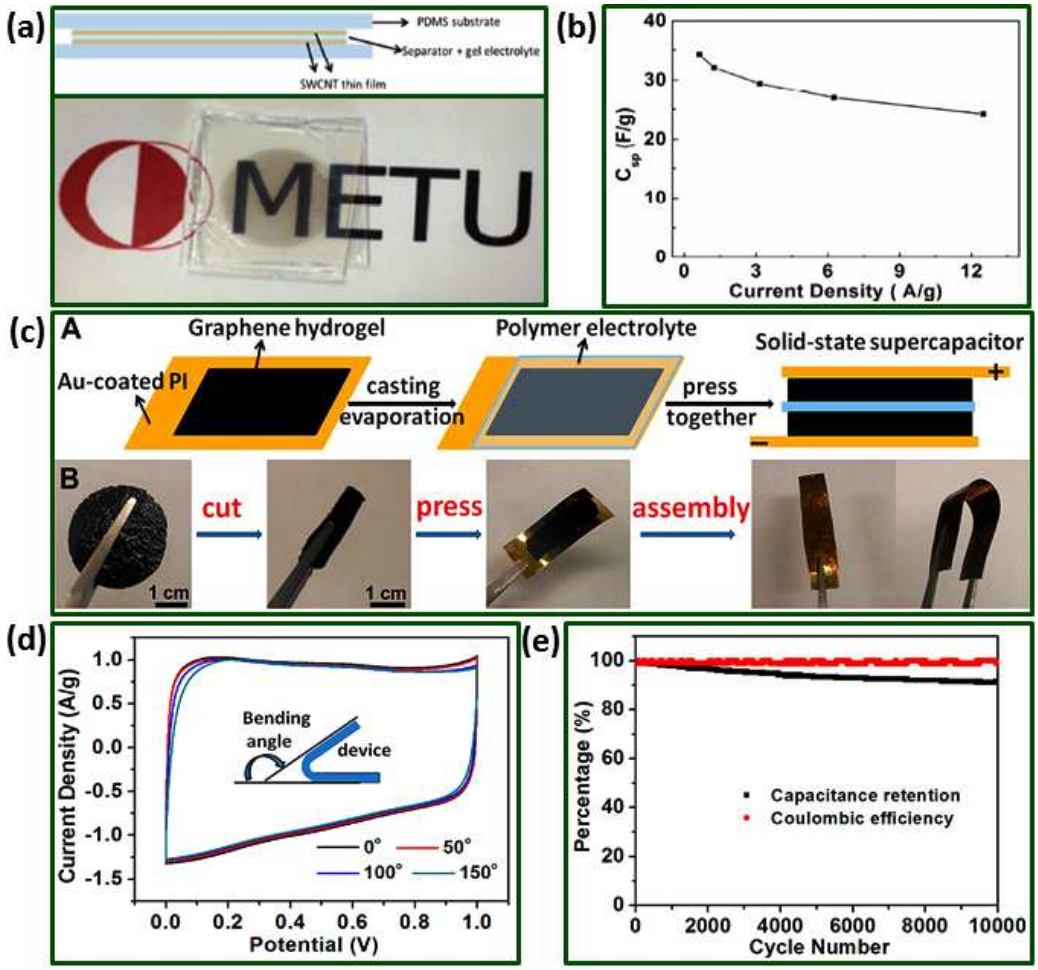

Figure 13 (a) Schematic and photograph of the fabricated supercapacitors without carbon paste current collectors. (b) Variation of specific capacitance with current density of SSC cell. Reprinted with permission from Ref. [228], Copyright 2014 American Chemical Society. (c) Schematic illustrations and photographs of the fabrication process of flexible solid-state supercapacitors based on graphene hydrogel films. (d) CV curves of FSC device at 10 mV/s for different bending angles. (e) Cycling stability of the device at a current density of 10 A/g with Coulombic efficiency. Adopted with permission from Ref. [279], Copyright 2013 American Chemical Society.

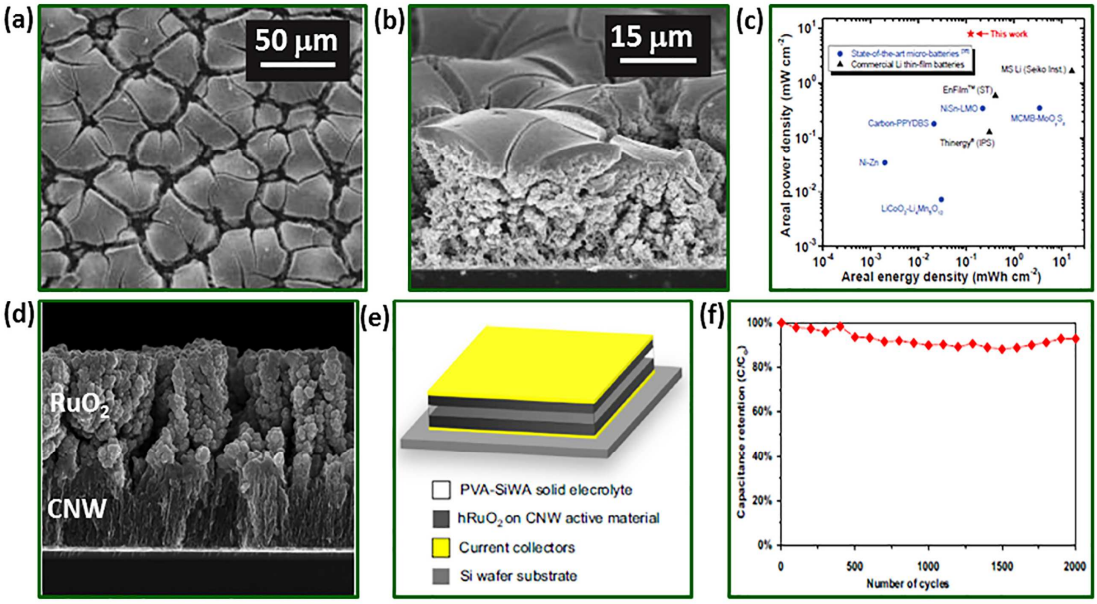

Figure 14 (a and b) SEM image (top-view and cross-section) of RuO_2 electrode after 300 electrodeposition cycles, respectively, (c) Ragone plot of the solid-state device based on RuO_2. Reproduced with the permission from [284], Copyright 2013 Wiley-VCH Verlag GmbH & KGaA. (d) Cross-section SEM image of a carbon nanowalls (CNW) film loaded with RuO_2, suggesting different morphologies such as cauliflower RuO_2 and vertically aligned CNW (e) Schematic diagram of fabrication of SSC based on RuO_2 on CNW electrodes, (f) Capacity retention with number of cycles for SSC device. Reproduced with the permission from [285], Copyright 2014 Elsevier.

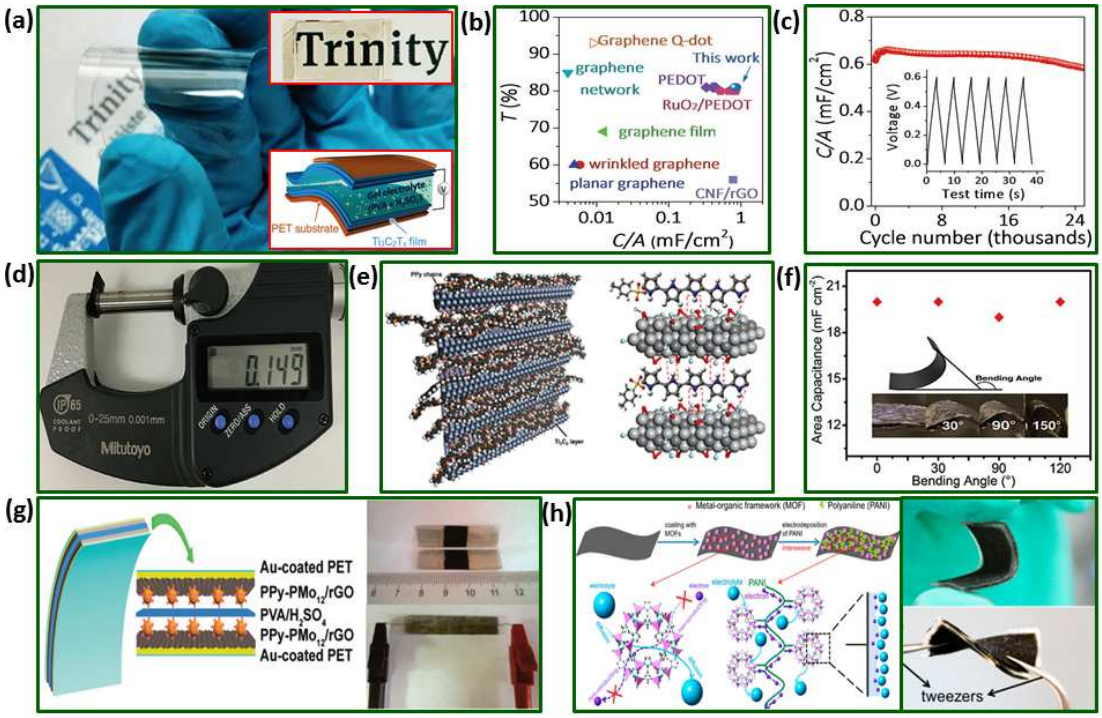

Figure 15 (a) Digital photographs of flexible, transparent $Ti_3C_2T_x$ film on PET substrate and inset shows schematic diagram and photograph of SSCs cell. (b) Comparison of areal capacitances with various transparent supercapacitors. (c) Cycling stability of a $Ti_3C_2T_x$ SSCs with the typical GCD curves upon cycling (inset). Reproduced with the permission from [314], Copyright 2017 Wiley-VCH Verlag GmbH & Co. KGaA, Weinheim. (d) Photograph of thickness of the as-prepared PPy/Ti_3C_2 SSC complete cell. (e) Schematic of intercalated PPy in the interlayers of Ti_3C_2 with corresponding atomic-scale presentation. (f) Performance of the PPy/Ti_3C_2 SSC under bending. Reprinted with the permission from [315], Copyright 2016 Wiley-VCH Verlag GmbH & Co. KGaA, Weinheim. (g) Schematic illustration of PPy-PMo_{12}/rGO SSCs with actual photographs of the device. Adopted from [322] Copyright 2015, Royal Society of Chemistry. (h) Steps involved in synthesis of PANI-ZIF-67-CC electrode with schematic representation of electron and electrolyte conduction in MOF (left) and MOF interwoven by PANI (right). Reprinted with the permission from [331], 2015, American Chemical Society.

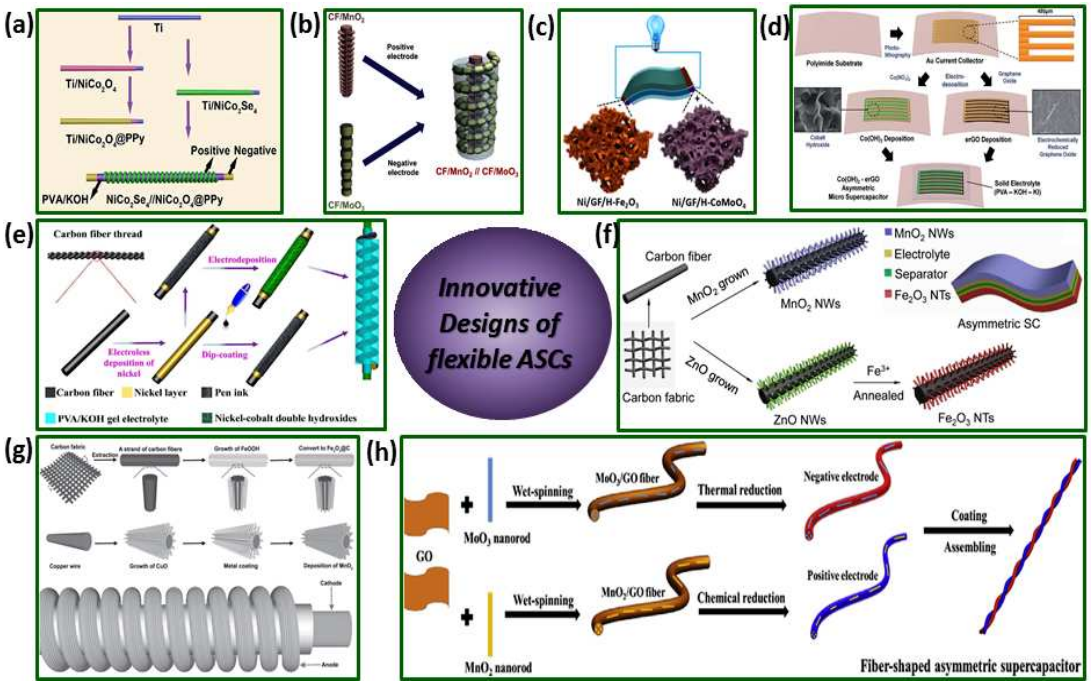

Figure 16 Recently developed innovative designs of ASCs that includes (a, b, e and g) Coil-type design, (c, f) planar design, (d) interdigitated and (h) wire-type design, Reprinted with the permission from [51b, 130, 399, 377c, 403, 442, 456, 463] American Chemical Society, Wiley-VCH Verlag GmbH & Co. KGaA, Weinheim, Elsevier, Royal Society of Chemistry.

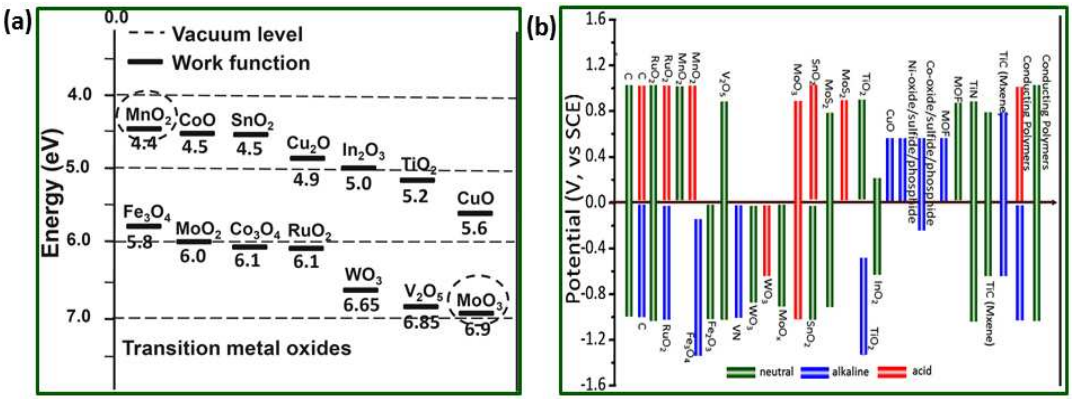

Figure 17 (a) Schematic illustration of work function of different metal oxides, Reprinted with permission from Ref. [397b], Copyright 2013 Wiley-VCH Verlag GmbH & KGaA. (b) Potential window of various electrode materials in aqueous electrolyte. Reproduced with the permission from Ref. [398c], Copyright 2015, Royal Society of Chemistry

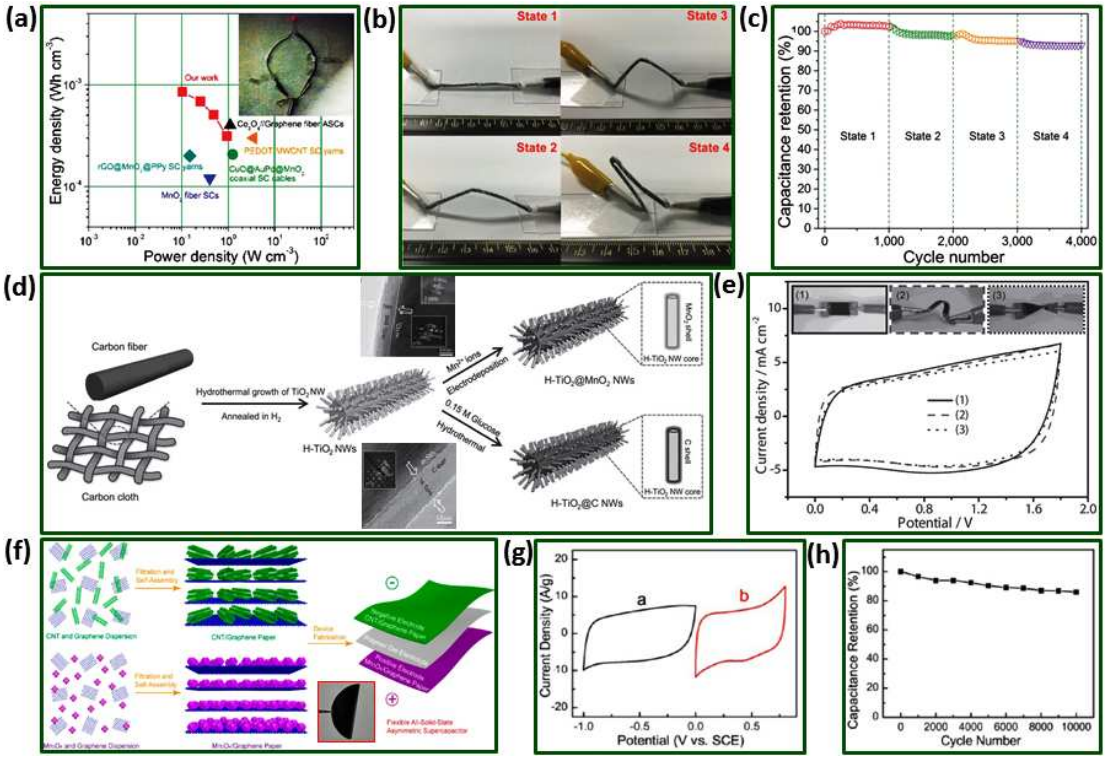

Figure 18 (a) Ragone plots of Fe_2O_3@C//MnO_2@CuO ASC compared with other recently reported values of ASCs. The inset shows a LED powered by ASC. (b) Photographs of cable-type ASC at different bending states. (d) Long-term cycling stability at different bending states. Adopted with the permission from [403], Copyright 2013 Wiley-VCH Verlag GmbH & KGaA. (d) Pictorial presentation of synthesis of hydrogenated (H)-TiO_2@MnO_2 and H-TiO_2@C core-shell NWs on a carbon cloth substrate as positive and negative electrodes for ASC respectively with corresponding TEM images. (e) CV curves recorded at a scan rate of 100 mV/s for (H)-TiO_2@MnO_2//H-TiO_2@C under different bending conditions with photographs of the device (inset). Reproduced with the permission from [405], Copyright 2013 Wiley-VCH Verlag GmbH & KGaA. (f) schematic presentation of synthesis steps of freestanding films of CNTs-graphene as negative and Mn_3O_4-graphene as a positive electrode, inset shows photograph of free-standing Mn_3O_4-graphene film, (g) CV curves of CNTs-graphene and Mn_3O_4-graphene in different working potential ranges, (d) Cycling stability of CNTs-graphene//Mn_3O_4-graphene ASC over 10,000 cycles at 50 mV/s scan rate. Reprinted with permission from Ref. [409], Copyright 2012 American Chemical Society.

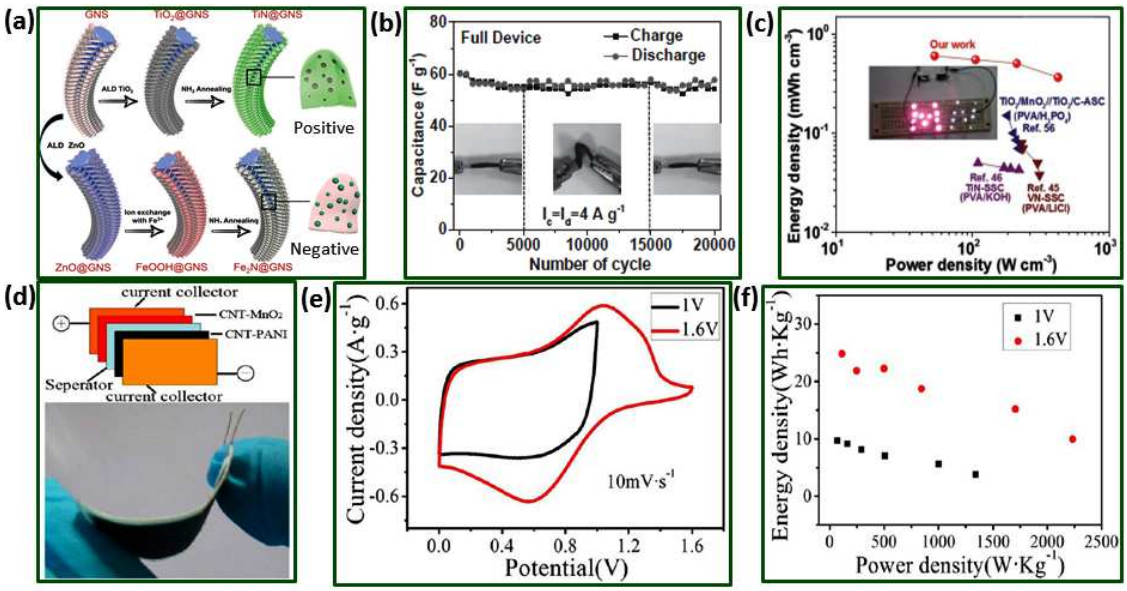

Figure 19 (a) Schematics of the fabrication of negative electrode (Fe_2N@GNS) and positive electrode (TiN@GNS) for ASC, (b) Cycling performance of Fe_2N@GNS//TiN@GNS device at 4 A/g in 20,000 cycles with different bending situations. (c) Ragone plots of quasi-solid-state Fe_2N@GNS//TiN@GNS ASC in comparison with other PVA-based solid electrolyte SSCs and ASCs with practical demonstration (inset). Reproduced with the permission from [414], Copyright 2015 Wiley-VCH Verlag GmbH & KGaA. (d) Schematic diagram of design of ASC based on CNT-MnO_2 as positive electrode and CNT-PAni as negative electrode with corresponding photograph of final ASC device. (e) CV curves and (f) Ragone plots of the CNT-MnO_2//CNT-PAni ASCs under different potential ranges. Reprinted with permission from Ref. [416], Copyright 2013 American Chemical Society.

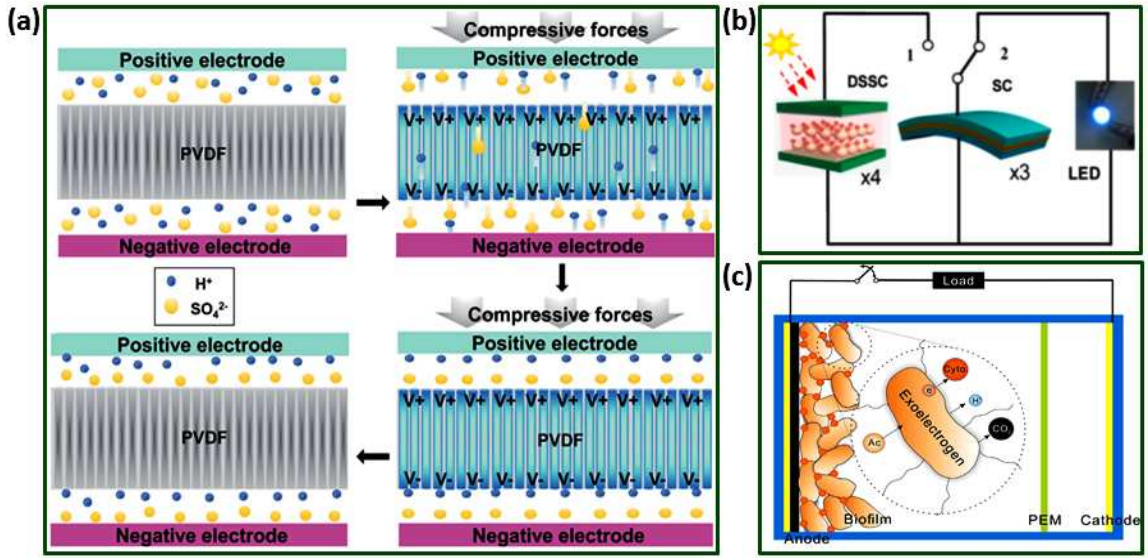

Figure 20 (a) Proposed working mechanism of the piezo-supercapacitor. Reproduced with the permission from [471], Copyright 2015, Royal Society of Chemistry. (b) Schematic of a self-powered system consisting of DSSCs and FSSCs, and one LED. Reproduced with the permission from [474 b], Copyright 2015, Elsevier. (c) Working principle of the microbial supercapacitor (MSC): when a high-speed switch is off, electrons are stored in the biofilm on graphene anode, and when it is on, electrons stored inside biofilm are discharged very quickly, resulting an extremely high current and power density. Reproduced with the permission from [485], Copyright 2015, Elsevier.

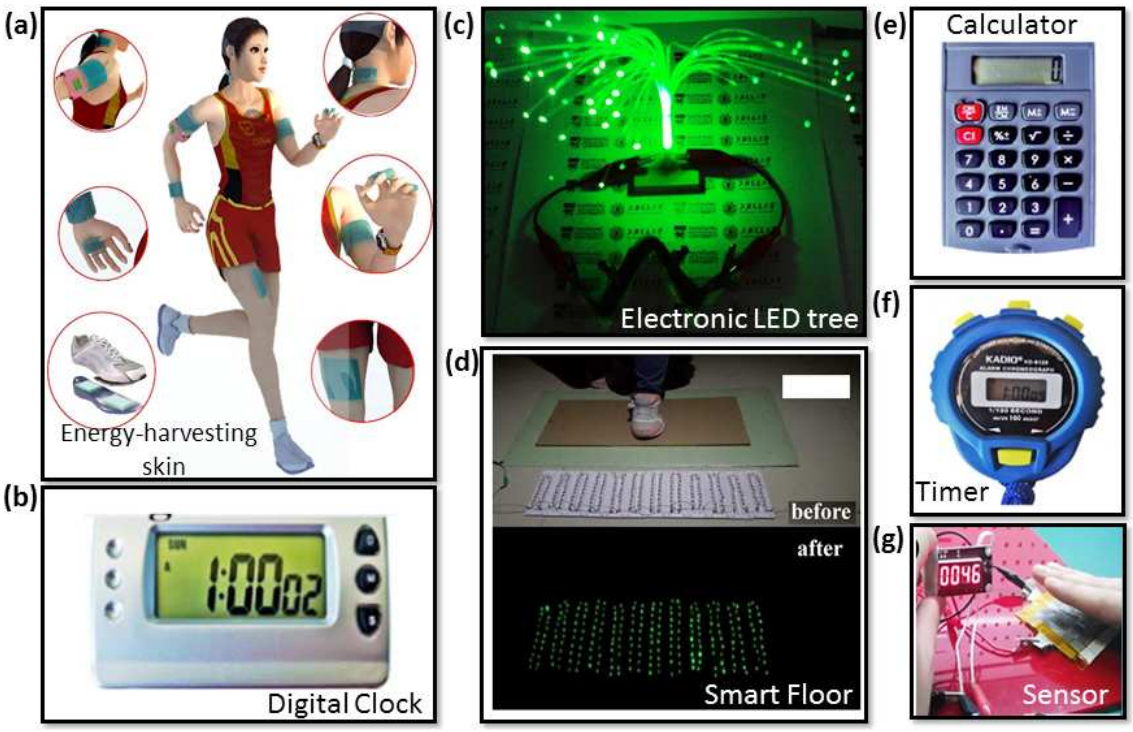

Figure 21 An overview of several new applications of FSSCs such as (a) triboelectric nanogenerator as energy-harvesting skin to scavenge energy from various motion of body parts. (b) Digital clock (c) an electronic LED tree (2.5 V) (d) large-area intelligent power floor (LIPF), LEDs lit up when a person stomps on the LIPF. (e) Calculator, (f) Competition timer (g) Sensors. Reprinted with permission from [470a, 469a, 58c and 468b] Elsevier and Nature Publishing Group.

Table 1 Various flexible substrates used for the fabrication of flexible solid-state devices and their electrochemic

Substrate	Materials	Cell design	Specific capacitance	Cycling
Ti wire	CNT	Symmetric	1.84 mF/cm^2 at 1 μA	80 % after
Au wire	MnO_2	Asymmetric	12 mF/cm^2 at 0.3 mA/cm^2	90 % after 2 0.6 m
Ni fibers	$Ni(OH)_2$	Symmetric	35.67 mF/cm at 0.1 mA	70 % over 1(0.5
Fiber	MnO_2 Nanowire/graphene	Symmetric	66.1 F/cm^3 at 60 mA/cm^3	96% over 10 0.12
carbon cloth	Activated carbon cloth	Symmetric	161.28 mF/cm^2 at 12.5 mA/cm^2	104 % after 3(12.5 m
mCel-Membrane	Activated carbon	Symmetric	153 mF/cm^2 at 10 mV/s	93.4 after 1(200
carbon cloth	polyaniline hydrogel	Symmetric	430 F/g at 5 mV/s	86 % after 1(
Stainless steel fabrics	Graphene	Symmetric	180.4 mF/cm^2 at 1 mA/cm^2	96.8 % after 8 mA
carbon cloth	TiO_2@PANI	Symmetric	775.6 mF/cm^3 (28.3 F/g) at 10 mV/s	97.2 % after 1 100
carbon cloth	$NiCo_2O_4$@CNT/CNT	asymmetric	-	95 % after 5 50 m
Ni Foam	C-$Co_3Si_2O_5(OH)_4$	Asymmetric	352 mF/cm^2 mF/cm^2 at 1 mA/cm^2	97.3 % after 4 mA
Carbon fabric	MnO_2//MoO_3	Asymmetric	4.86 mF/cm^2 at a 0.5 mA/cm^2	89 % after 3(mA
Carbon fabric	MnO_2	Symmetric	-	76.5 % after 1 mA
PET	$Ti_3C_2T_x$	Symmetric	1.44 F/cm^3 at 0.288 A/cm^3	87 % over 1 100
Carbon fabric	MnO_2/reduced graphene oxide (RGO)	Symmetric	14 F/cm^2 (31.8 F/g) at 2 mV/s	100 % after 5 0.2 m
Carbon fabric	MoS_2	Symmetric	-	96.5 % after 0.2

PET	SnS/S doped graphene	Symmetric	2.98 mF/cm^2 at 60 mA/cm^2	99 % after 1 120 m
Carbon fabric	MnO_2	Symmetric	0.44 F/cm^3 (283.9 F/g) at 0.2 A/g	83 % after 1 0.5
Carbon fabric	Co_3O_4/Vertically aligned graphene nanosheets (VAGNs)	Symmetric	580 F/g at 1 A/g	86.3 % after 2 20
Carbon fabric	CoMn-LDH	Symmetric	-	88.3 % after 2 A
Carbon fabric	Functionalized Carbon fabric	Symmetric	134.8 mF/cm^2 (2.4 F/ cm^3) at 2 mA/cm^2	90 % after 50 mA
Carbon fabric	$CuCo_2O_4$@MnO_2	Symmetric	714 mF/cm^2 at 1 mA/cm^2	3000 cycles
Carbon fabric	MnO_2	Symmetric	42.4 mF/cm^2 at 5 mV/s	96.4 % after 100
Carbon fabric	Cu_7S_4	Symmetric	-	95 % after 50 m
Carbon textile	ZnS	Symmetric	540 F/g at 5 mV/s	96.6 % after 0.8 m
Nickel Foam	$ZnCo_2O_4$	Symmetric	94 mF/cm^2 at 0.1 mA/cm^2	97.4 % after 0.5 m
Nickel Foam	MnO_2–CNT–graphene	Symmetric	107 F/g,	
Nickel Foam	PPy@LDH core–shell	Asymmetric	88.7 mF/cm^2 at 20 mA/cm^2	115.4 % after at 20
Nickel Foam	$NiCo_2O_4$	Symmetric	161 mF/cm^2 at 1 mA/cm^2	100 % 3000 mA
Carbon cloth	N/O-enriched carbon cloth	Symmetric	-	116 % 5000 mA
Commercial textiles	MnO_2/CNT	Symmetric	324 F/g at 0.5 A/g	100 % 5000 A
Commercial A4-size paper	graphene sheets	Symmetric	11.3 mF/cm^2 at 1 mV/s	
Photo paper	PANI–MnO_x	Symmetric	94.73 mF/cm^2 at 0.1	

			mA/cm^2	
Xerox printing paper	$MnO_2/Au/MnO_2$	Symmetric	8.14 mF/cm^2 (20.35 F cm^3) at 0.2 mA/cm^2	88 % after 5 100
Carbon Fiber Yarn	MnO_2	Symmetric	-	85 % after 1(0.1
A4 printing paper	graphite/polyaniline	Symmetric	77.8mF/cm^2 at 0.1mA/cm^2,	83% after 10,(mA
Filter paper	KCu_7S_4/Graphene	Symmetric	-	92 % after 5, 0.8 m
PET	MnOx/Au	Symmetric	78.6 F/cm^3 at 10 mV/s	74.1% after 1: 1 V
PET	Ag/activated carbon	Symmetric	45 mF/cm^2 at 0.3 mA cm^2	86 % after 12 mA
PET	Graphene/MWNT	Symmetric	740.9 $\mu F/cm^2$ at 1 $\mu A/cm^2$	85 % after 2(15 μA
PET	SWCNTs	Symmetric	17.5 F/g at 2 A/g	87.5 % after 1 5 A
PET	Au/PANI	Symmetric	26.49 mF/cm^2 (67.06 F/cm^3) at 0.5 mA/cm^2	72.7 % after 200
Carbon paper	graphene oxide/metal–organic framework (GO/MOF)	Symmetric	250 mF/cm^3 at 6.4 mA/cm^3	96.3% after 5 50.4 m
PET	Au/polyaniline	Symmetric	51.7 mF/cm^2 at 0.1 mA/cm^2	92 % after 1 0.2 m
PET	rGO/PPy	Symmetric	147.9 F/cm^3 at 5 A/ cm^3	71.7 % after 10 A
PET	N-doped rGO	Symmetric	3.4 mF/cm^2 at 20 $\mu A/cm^2$	98.4 % after 100 μ
PET	MoS_2@$Ni(OH)_2$	Symmetric	14.07 mF/cm^2 (37.53 F/cm^3) at 1 mV/s	94.2% after 9(V
PET	rGO/MoO_3	Symmetric	404 F/g at 0.5 A/g	80 % after 50 A

Au coated PET	CuSe	symmetric	30.17 mF/cm^3 at 0.14 mA/cm^3	90 % after 1 0.57 m
PET	graphene	Symmetric	56.5 F/cm^3 at 0.06 A/cm^3	
PET	β-Ni(OH)$_2$/graphene	Symmetric	2570 μF/cm^2 at 0.2 A/m	98.2 % after 0.1
Air-laid paper	PPy	Symmetric	702 mF/cm^2 at 1 mA/cm^2	
PET	graphene/carbon black nanoparticle	Symmetric	144.5 F/g at the current density of 0.5 A/g	
PET or PDMS	Graphene fibers/MnO_2 fibers	Symmetric	42.02 mF/cm^2 at 0.01 V/s	92 % after 1 mA
PDMS	Graphene	Symmetric	4.2 mF/cm^2 at 0.1 μA	
PDMS	SWCNTs	Symmetric	36.9 F/g at 10 mV/s	94 % after 1.25
carbon fiber paper	Silver nanoparticle-polyaniline-graphene	Symmetric	142 F/g at 1.5A/g	
Stainless steel	V_2O_5	Symmetric	96 F/g at 0.5 A/g	88 % after 1 20 m
carbon nanofibers	$ZnCo_2O_4$// carbon nanofibers	Asymmetric	139.2 F/g at 2 mV/s	90 % after 3 50 m
Cu foils	Graphene oxide	Symmetric	130 F/g at 5 mV/s	
Cu foils	Cu(OH)$_2$//AC	Asymmetric	26.4 F/g at 4 A/g	90% after

Table 2 Advances in gel-polymer electrolytes based on combinations of different plasticizers and polymer hos
corresponding room temperature ionic conductivities

Polymer Host	Electrolytic salt	Type of electrolyte	Ionic condu (mS/c
PAM	LiCl	Aqueous	10
PVA	SiWA-H_3PO_4	Aqueous	8
PVA	SiO_2-SiWA-H_3PO_4	Aqueous	16
PVA	BWA	Aqueous	78
PVA	H_2SO_4	Aqueous	30
PVA	KOH	Aqueous	0.1
PEO	KOH	Aqueous	1 to 1
PVA	GO doped KOH	Aqueous	200
PEO	TEAOH	Aqueous	11.2
PAA	TEAOH	Aqueous	0.9
PAN-b-PEG-b-PAN	DMF-$LiClO_4$	Organic	6.9
PEO	PC-NaTFSI	Organic	0.54
PEO	PC-EC-DMC-NaTFSI	Organic	0.76
PVDF-HFP	PC-$Mg(ClO_4)_2$	Organic	5.4
PVA	BMIMCl-Li_2SO_4	Ionic liquid	37
PVDF-HFP	GO doped $EMIMBF_4$	Ionic liquid	25
PEGDA	[EMIM][TFSI]	Ionic liquid	9.4
PEO	$EMIHSO_4$-$MIHSO_4$	Ionic liquid	1.7
PEO	$EMIHSO_4$-$ImHSO_4$	Ionic liquid	2.5
PVA	BAAS doped H_2SO_4	Redox-active aqueous	21.4
PVA	AQQS doped H_2SO_4	Redox-active aqueous	28.5
PMMA	PC-Fc doped $TEABF_4$	Redox-active organic	1.89
PMMA	PC-4-oxo TEMPO doped $TEABF_4$	Redox-active organic	1.73
PVA	$EMIMBF_4$ doped H_3PO_4	Redox-active ionic liquid	39.3
PAN-b-PEG-b-PAN	$LiClO_4$	Organic	11
PEO	$LiClO_4$-TiO_2-Al_2O_3	Organic	0.03
PEOEMA	$BMIPF_6$ and $LiPF_6$	Ionic liquid	0.94
PHEMA/chitosan	EMIMCl	Ionic liquid	25

PVdF-HFP	EMITf	Ionic liquid	13
PVdF-HFP	EMITf	Ionic liquid	5.19
PVdF-HFP	EMITf-NH_4Tf	Ionic liquid	0.23
PMMA	PC-EC-$LiClO_4$ OR PC-EC-$NaClO_4$ OR PC-EC-$TEAClO_4$	Organic	1
PAN	[BMIM][TFSI]	Ionic liquid	2.42
PEGDA	[EMIM][TFSI]	Ionic liquid	9.4
PVA	p-benzenediol (PB) doped H_2SO_4	Redox active aqueous	34.8

Table 3 Comparison of electrochemical performances of flexible solid-state symmetric designs based on differen

Electrode Material	Electrolyte	Specific capacitance	Energy density	Power density	Capacitanc
Treated carbon cloth	PVA-H_2SO_4	920 mF/cm^2 at 2 mA/cm^2	1.4 mWh/cm^3	280 mW/cm^3	100 % aft cyc
Graphene	PVA-H_2SO_4	80 F/g at 5 mV/s	8.87 Wh/kg	7.142 kW/kg	100 % ov cycles (0.5
Polyaniline	PVA-H_2SO_4	237.5 mF/cm^2 at 10 mV/s	24.31 mWh/ cm^3	140 mW/cm^3	95.2 % o cycles (1
α-Fe_2O_3/rGO	PVA-KOH	32.9 mF/cm^2 at 1 mA/cm^2	1.46 mWh/cm^3	2011.8 mW/cm^3	79.1 % o cycles (2.5
Carbon quantum dots/polypyrrole	PVA-LiCl	315 mF/cm^2 at 0.2 mA/cm^2	-	-	85.7 % o cycles (2
N/O co-doped graphene quantum dots	PVA-H_2SO_4	461 mF/cm^2 at 0.5 mA/cm^2	0.032 mWh/cm^2	-	87.5 % o cycles (15
MWCNTs	PVA-H_3PO_4	2.02 F/cm^3 at 10 mV/s	0.18 mWh/cm^3	400 mW/cm^3	94.1 % o cycles (0.1
MWCNTs	PVA-H_3PO_4	26.8 F/g at 1 A/g	3.5 Wh/kg	28.1 kW/ kg	92 % over 5 (4 A
CNTs/$NiCo_2O_4$	PVA-KOH	337.3 mF/cm^2 at 0.1 mA/cm^2	1.17 mWh/cm^3	2430 mW/cm^3	95.6 % o cycles (
CuO/3D graphene	PVA-LiCl	64 mF/cm^2 at 0.25 mA/cm^2	0.0059 mWh/cm^2	110 μW/cm^2	86 % over 5 (5 mA
Expanded graphite foil	PVA-H_2SO_4	30.5 mF/cm^2 at 1 mA/cm^2	0.163 mWh/cm^3	447 mW/cm^3	92 % over 1 (20 mA
$FeCo_2S_4$–$NiCo_2S_4$	PVA-KOH	-	46 Wh/kg	4.723 kW/kg	92 % over 3 (10 mA
MXene/graphene	PVA-H_3PO_4	216 F/cm^3 at 0.1 A/cm^2	3.4 mWh/cm^3	1600 mW/cm^3	85.2 % o cycles (1
MnO_2	PVA-LiCl	776 F/g at 0.5 A/g	0.17 mWh/cm^3	-	91 % over 2 (4 A

graphene/MoS_2	PVA-H_3PO_4	19.44 F/cm^3 at 0.3 mA	1.728 mWh/cm^3	62 mW/cm^3	95 % over 1
graphene/polyaniline	PVA-H_2SO_4	665 F/g at 1 A/g	14.2 mWh/cm^3	-	100 % over (5 A
N-doped cotton-derived carbon frameworks (NCCF)-rGO	PVA-KOH	200 F/g at 0.1 A/g	20 Wh/kg	-	94 % over 1 (3 A
Graphene	PVA-H_2SO_4	4.21 mF/cm^2 at 0.1 mA/cm^2	0.552 mWh/cm^3	561.9 mW/cm^3	94.8 % ov cycles (0.1
MnO_2	PVA-KOH	847.22 mF/cm^2 at 0.41 mA/cm^2	0.0188 mWh/cm^2	16.33 mW/cm^2	92.7 % o cycles (0.1
MnO_2/CNT	PVA-H_3PO_4	830 F/g at 1 mV/s	115.2 Wh/kg	73.9 kW/kg	89 % over 3 (20 r
MoS_2/CNT	PVA-H_2SO_4	16.3 mF/cm^2 at 20 mV/s	0.92 mWh/cm^3	2100 mW/cm^3	95.1 % ov cycles (10
$MoSe_2$	PVA-KOH	133 F/g at 2 A/g	36.2 Wh/kg	1.4 kW/kg	92 % over 2 (100 r
PEDOT:PSS/ MWCNT	PVA-KOH	380 F/g at 0.25 A/g	13.2 Wh/kg	4.99 kW/kg	90 % over 1 (1 A
PANI/N-Carbon	PVA-H_2SO_4	122 mF/cm^2 at 0.05 mA/cm^2	0.22 mWh/cm^2	-	91.3 % o cyc (1 A
PEDOT:PSS	PVA-H_2SO_4	202 F/cm^3 at 0.54 A/cm^3	-	-	100 % ov cycles (1
rGO/PANI	PVA-H_2SO_4	6.4 mF/cm^2 at 0.08 mA/cm^2	7.07 Wh/kg	-	72 % over 2 (0.1 mA
ZnS/CNTs	PVA-KOH	159.6 F/g at 1 A/g	22.3 Wh/kg	5 kW/kg	91.8 % o cyc (1 A
$ZnCo_2O_4$/rGO	PVA-KOH	143 F/g at 1 A/g	11.44 Wh/kg	1.382 kW/kg	93.4 % o cyc

					(3 A
Pt/n-CNT@PANI	PVA-H_3PO_4	217.7 F/g at 0.2 A/g	30.22 Wh/kg	9.072 kW/kg	96 % over 5 (1.8 A
Waste paper fibers-RGO-MnO_2	PVA-Na_2SO_4	220 F/g at 1 A/g	19.6 Wh/kg	2.4 kW/kg	85.3 % o cyc (1 A
Porous carbon	PVA-KOH	81.3 F/g at 0.5 A/g	7.22 Wh/kg	-	-
SWCNTs/TiO_2	PVA-LiCl	28 F/g at 20 mV/s	-	66.7 kW/kg	100 % over
SnS/S-Doped Graphene	PVA-H_2SO_4	2.98 mF/cm^2 at 60 mA/m^2	-	-	99 % ove cyc
rGO/Mn_3O_4	PVA-H_3PO_4	45.5 F/cm^3 at 50 mA/cm^3	4.05 mWh/cm^3	268 mW/cm^3	85 % ove cycles (2
rGO/PPy	PVA-H_3PO_4	0.51 F/cm^2 at 0.1 mA/cm^2	1.18 mWh/cm^3	-	-
$MoSe_2$	PVA-KOH	133 F/g at 2 A/g	36.2 Wh/kg	1.4 kW/kg	92 % over 2 (2 A
$SnSe_2$	PVA-H_2SO_4	406 μF/cm^2 at 20 mA/m^2	-	-	100 % over (50 mA
SnSe	PVA-H_2SO_4	1176 μF/cm^2 at 45 mA/m^2	-	-	100 % over (60 mA
rGO/$Ti_3C_2T_x$	PVA-KOH	-	63 mWh/cm^3	60 mW/cm^3	100 % ov cycles (

Table 4. Summary of electrochemical performances of flexible solid-state asymmetric designs based on different electrodes with corresponding gel-electrolytes.

Positive electrode	Negative electrode	Electrolyte	Voltage window	Specific capacitance	Max. Energy density	Max. Power density
$Co_{2.18}Ni_{0.82}Si_2O_5(OH)_4$	Graphene	KOH/PVA	1.75 V	194.3 mF/cm^2 at 0.50 mA/cm^2	0.496 mWh/cm^3	38.8 mW/cm^3
graphene/MnO_2	graphene/ polypyrrole	KOH/PVA	1.8 V	2.69 F/cm^3 (175.2 F/g) at 1 mA/cm^2	1.23 mWh/cm^3	-
CW/PNC/PEDOT	CW/CMK-3	KOH/PVA	1.45 V	31.6 mF/cm^2 (3.16 F/cm^3) at 0.4 mA/cm^2	0.011 mWh/cm^2	7.8 mW/cm^2
Mn_3O_4/NGP	$Ni(OH)_2$/NGP	NaOH/PVA	1.3 V	1.96 F/cm^3 at 50 mV/s	0.35 mWh/cm^3	32.5 mW/cm^3
TiN@GNSs	Fe_2N@GNSs	LiCl/PVA	1.6 V	60 F/g at 50 mV/s	15.4 Wh/kg	6.4 kW/kg
$Ni_{20}[(OH)_{12}(H_2O)_6][(HP_4)_8(PO_4)_4].12H_2O$	graphene	KOH/PVA	1.47 V	148 F/cm^2 at 0.5 mA/cm^2	0.446 mWh/ cm^3	44.1 mW/cm^3
$NaCoPO_4$–Co_3O_4	graphene	KOH/PVA	1.0 V	28.6 mF/cm^2 at 0.1 mA/cm^2	0.39 mWh/cm^3	50 mW/cm^3

$NiCo_2O_4$@PPy	activated carbon (AC)	KOH/PVA	1.6 V	165.4 F/g at 1 mA/cm^2	58.8 Wh/kg	10.2 kW/kg	
Co_3O_4@C@Ni_3S_2	AC	KOH/PVA	1.8 V	-	1.52 mWh/cm^3	60000 mW/cm^3	
MoS_2-rGO/MWCNT	rGO/MWCNT	H_2SO_4 /PVA	1.4 V	5.2 F/cm^3 at 0.16 A/cm^3	-	-	
Carbon Fiber (CF) −$Ni(OH)_2$	CF−CNT	KOH-PVA	1.3 V	-	41.1 Wh/kg	3.5 kW/kg	
$K_2Co_3(P_2O_7)_2$-$2H_2O$	graphene	KOH/PVA	1.07 V	6 F/cm^3 at 10 mA/cm^3	0.96 mWh/cm^3	54.5 mW/cm^3	
MnO_2/graphene/CF	graphene hydrogel (GH)/ copper wire (CW)	KCl/PAAK	1.6 V	2.54 F/cm^3 at 0.2 mA/cm^2	0.9 mWh/cm^3	200 mW/cm^3	
CF@RGO@MnO_2	CF@TRGO	KCl/PAAK	1.6 V	-	1.23 mWh/cm^3	270 mW/cm^3	
MnO_2	$CoSe_2$	LiCl/PVA	1.6 V	1.77 F/cm^3 at 1 mA/cm^2	0.588 mWh/cm^3	282 mW/cm^3	
$NiCo_2O_4$/CC	porous graphene papers (PGP)	LiOH/PVA	1.8 V	71.32 F/g at 5 mA/cm^2	60.9 Wh/kg	11.36 kW/kg	
$Co_{11}(HPO_3)_8(OH)_6$-Co3O_4	graphene	KOH/PVA	1.38 V	1.84 F/cm^3 at 0.5 mA/cm^2	0.48 mWh/cm^3	105 mW/cm^3	
$CoMoO_4$/PPy	AC	KOH/PVA	1.7 V	-	104.7 Wh/kg	971.43 W/kg	
MnO_2	Fe_2O_3	$LiClO_4$/ PVA	2.0	147 F/g at 5 mV/s	41 Wh/kg	10 kW/kg	
CuO	Fe_2O_3	Na_2SO_4/ CMC	2.0	79 F/g at 2 mA/cm^2	23 Wh/kg	19 kW/kg	

Ni/MnO_2	AC	Na_2SO_4/ PVA	2.5 V	2.0 F/cm^3 at 5 mV/s	0.78 mWh/cm^3	50 mW/cm^3	
Cobalt carbonate hydroxide/N-doped graphene	N-doped graphene	KOH/PVA	1.9 V	153.5 mF/cm^2 at 1.0 mA/cm^2	0.077 mWh/cm^2	2.5 mW/cm^2	
γ-MnS	Eggplant derived AC (EDAC)	-	1.6 V	110.4 F/g at 1.0 mA	37.6 Wh/kg	181.2 W/kg	
$NiCo_2Se_4$	$NiCo_2O_4$@PPy	KOH/PVA	1.7 V	14.2 F/cm^3 at 63.7 mA/cm^3	5.18 mWh/cm^3	260 W/cm^3	
CoS	AC	KOH/PVA	1.8 V	47 F/g at 2 A/g	5.3 Wh/kg	1.8 kW/kg	
Human hair/Ni /Graphene/MnO_2	human hair/Ni/ Graphene	KOH/PVA	1.8 V	4.10 F/cm^3 at 100 mV/s	1.81 mWh/cm^3	-	
carbon fiber/MnO_2	carbon fiber/MoO_3	KOH/PVA	2.0 V	3.20 mF/cm^2 at 5 mA/cm^2	0.0027 mWh/cm^2	0.53 mW/cm^2	
$Co_3O_4/Co(OH)_2$	AC	KOH/PVA	1. 4 V	210 mF/cm^2 at 0.3 mA/cm^2	9.4 mWh/cm^3.	354 mW/cm^3	
MnO_2	CoP	LiCl/PVA	1.6 V	1.94 F/cm^3 at 1 mA/cm^2	0.69 mWh/cm^3	114.2 mW/cm^3	
$CoMoO_4$	Fe_2O_3	KOH/PVA	1.5 V	3.6 F/cm^3 at 1 mA/cm^2	1.13 mWh/cm^3	150 mW/cm^3	
$CoMoO_4$@ $NiMoO_4$·xH2O	Fe_2O_3	KOH/PVA	1.6 V	153.6 F/g at 1 A/g	41.8 Wh/kg	12 kW/kg	
CuS/3D graphene	3D graphene	KOH/PVA	1.6 V	32 F/g at 1 A/g	5 Wh/kg	3.2 kW/kg	
Co_3O_4	AC	KOH/PVA	1.5 V	215 mF/cm^2	-	-	

				at 1.5 mA/cm^2			
MnO_2	porous carbon cloth	PVA/LiCl	2 V	1515 mF/cm^2 at 2 mA/cm^2	0.841 mWh/cm^2	-	
MnO_2@CNTs@3D graphene foams	Ppy@CNTs@ 3D graphene foams	Na_2SO_4/ PVA	1.8 V	8.56 F/cm^3 (950 mF/cm^2) at 1 mA/cm^2	3.85 mWh/cm^3	630 mW/cm^3.	
MnO_2@PANI	3D graphene foam (GF)	KOH/PVA	1.5 V	95.3 F/g at 1 A/g	37 Wh/kg	386 W/kg	
$Ni(OH)_2$-N-doped graphene (NG)	NG	H_2SO_4/PVA	1.45 V	255 mF/cm^2 at 1.0 mA/cm^2	79.5 mWh/cm^2	944 mW/cm^2	
Ni−Co LDHs/pen ink/nickel/CF	Pen ink/ nickel/CF	KOH/PVA	1.55 V	28.67 mF/cm^2 at 0.5 A/g	0.00957 mWh/cm^2	1.841 mW/cm^2	
Ni-Co@Ni-Co LDH	carbon fibers	KOH/PVA	1.5 V	319 F/g at 2 A/g	100 Wh/kg	15 kW/kg	
Co_3O_4-nanocube/$Co(OH)_2$-nanosheet	AC	KOH/PVA	1.4 V	210 mF/cm^2 at 0.3 mA/cm^2	9.4 mWh/cm^3	354 mW/cm^3	
$NiCo_2S_4$@$NiCo_2O_4$	AC	KOH/PVA	1.6 V	0.41 F/cm^2 at 2 mA/cm^2	44.6 Wh/kg	6.4 kW/kg	
$NiCo_2S_4$/Polyaniline	AC	KOH/PVA	1.6 V	152.1 F/g at 1 A/g	54.06 Wh/kg	27.1 kW/kg	
NiCo-LDH	Carbon nanorods	KOH/PVA	1.7 V	147.6 F/g at 1 A/g	59.2 Wh/kg	34 kW/kg	
MnO_2	Carbon	LiCl/PVA	2.0 V	71.856	0.766	142.56	

				mF/cm^2 at 0.5 mA/cm^2	mWh/cm^3	mW/cm^3
MnO_2 nanorods/rGO	MoO_3 nanorods/rGO	H_3PO_4/PVA	1.6 V	51.2 F/cm^3 at 2 mV/s	18.2 mWh/cm^3	3269 mW/cm^3
$Ni(OH)_2$/RGO/Ni	RGO aerogel/Ni	KOH/PVA	1.6 V	69 F/g at 2 A/g	24.5 Wh/kg	10.3 kW/kg
$ZnCo_2O_4$	VN	KOH/PVA	1.6 V	196.43 mF/cm^2 at 1 mA/cm^2	64.76 mWh/cm^3	8000 mW/cm^3
MOF-MnO_x	AC	KOH/PVA	1.2 V	175 mF/cm^2 at 0.5 mA/cm^2	5.1 mWh/cm^3	120 mW/cm^3

Acronyms

- Polyacrylamide – PAM
- Polyvinyl alcohol – PVA
- Poly(ethylene oxide)- PEO
- Poly(methyl methacrylate) – PMMA
- Poly(polyacrylate)- PAA
- Poly(amine-ester) – PAE
- Polyacrylonitrile (PAN),
- Poly(vinylidene fluoride)- PVdF
- Poly(vinylidene fluoride-co-hexafluoropropylene) - PVdF-HFP
- Poly-(ethylene glycol)- PEG
- Poly(ethylene glycol) diacrylate – PEGDA
- Poly(2-ethoxyethyl methacrylate)- PEOEMA
- Silicotungstic acid – SiWA
- $H_5BW_{12}O_{40}$- BWA
- Tetraethylammonium hydroxide – TEAOH
- Dimethylformamide – DMF
- Propylene carbonate – PC
- Sodium bis(trifluoromethanesulfonyl)imide – NaTFSI
- Ethylene carbonate – EC
- Dimethyl carbonate – DMC
- 1-butyl-3-methylimidazolium chloride - BMIMCl
- 1-ethyl-3-methylimidazolium tetrafluoroborate - $EMIMBF_4$
- 1-ethyl-3-methylimidazolium bis(trifluoromethylsulfonyl)imide - [EMIM][TFSI]
- 1-ethyl-3-methylimidazolium hydrogen sulfate - $EMIHSO_4$)
- 1-methylimidazolium hydrogen sulfate - $MIHSO_4$
- Imidazolium hydrogen sulfate - $ImHSO_4$
- 1-butyl-3-methylimidazolium hexafluorophosphate - $BMIPF_6$
- 1-ethyl-3-methylimidazolium chloride -EMIMCl
- Bromamine acid sodium – BAAS
- 1-anthraquinone sulfonic acid sodium – AQQS
- 2-mercaptopyridine – PySH
- Ferrocene – fc
- 4-oxo-2, 2, 6, 6-tetramethylpiperidinooxy - 4-oxo TEMPO
- Tetraethylammonium tetrafluoroborate - $TEABF_4$
- 1-ethyl 3-methyl imidazolium trifluoromethanesulfonate – EMITf
- Ammonium trifluoromethanesulfonate -NH_4Tf

- 1-butyl-3-methylimidazolium bis(trifluoromethylsulfonyl)imide – [BMIM][TFSI]
- p-benzenediol – PB
- Polyethylene terephthalate – PET
- Polydimethylsiloxane – PDMS
- Carboxymethyl cellulose – CMC
- Polyethersulfone – PES
- Polyoxometalates-POMs
- Black Phosphorous- BP
- Metal-organic Frameworks - MOFs